



FACULTY OF ELECTRICAL ENGINEERING  
UNIVERSITY OF BANJA LUKA

# ELECTRONICS

# FACULTY OF ELECTRICAL ENGINEERING UNIVERSITY OF BANJA LUKA

Address: Patre 5, 78000 Banja Luka, Bosnia and Herzegovina

Phone: +387 51 211824

Fax: +387 51 211408

## ELECTRONICS

Web: [www.electronics.etfbl.net](http://www.electronics.etfbl.net)

E-mail: [electronics@etfbl.net](mailto:electronics@etfbl.net)

### *Editor-in-Chief:*

Branko L. Dokić, Ph. D.  
Faculty of Electrical Engineering  
University of Banja Luka, Bosnia and Herzegovina  
E-mail: [bdokic@etfbl.net](mailto:bdokic@etfbl.net)

### *International Editorial Board:*

- Goce Arsov, St. Cyril and Methodius University, Skopje, Republic of Macedonia
- Petar Biljanović, University of Zagreb, Croatia
- Milorad Božić, University of Banja Luka, Bosnia and Herzegovina
- Tatjana Pešić-Brđanin, University of Banja Luka, Bosnia and Herzegovina
- Vladimir Katić, University of Novi Sad, Serbia
- Vančo Litovski, University of Niš, Serbia
- Danilo Mandić, Imperial College, London, United Kingdom
- Vojin Oklobdžija, University of Texas at Austin, USA
- Zorica Pantić, Wentworth Institute of Technology, Boston, USA
- Aleksandra Smiljanić, University of Belgrade, Serbia
- Slobodan Vukosavić, University of Belgrade, Serbia
- Volker Zerbe, Technical University of Ilmenau, Germany
- Mark Zwoliński, University of Southampton, United Kingdom
- Deška Markova, Technical University of Gabrovo
- Chakresh Kumar, Galgotias College of Engineering and Technology, Greater Noida, India

### *Secretary:*

Mladen Knežić, M.Sc.  
E-mail: [mladen\\_knezic@etfbl.net](mailto:mladen_knezic@etfbl.net)

Željko Ivanović, M.Sc.  
E-mail: [zeljko@etfbl.net](mailto:zeljko@etfbl.net)

### *Publisher:*

Faculty of Electrical Engineering  
University of Banja Luka, Bosnia and Herzegovina  
Address: Patre 5, 78000 Banja Luka, Bosnia and Herzegovina  
Phone: + 387 51 211824  
Fax: + 387 51 211408  
Web: [www.etfbl.net](http://www.etfbl.net)

Number of printed copies: 100





# Morlet Wavelet UDWT Denoising and EMD based Bearing Fault Diagnosis

A. Santhana Raj and N. Murali

**Abstract**—Bearing Faults in rotating machinery occur as low energy impulses in their vibration signal and are lost in the noise. This signal has to be properly denoised before analyzing for effective condition monitoring. This paper proposes a novel method to denoise and analyze such a noisy signal. The Undecimated Discrete Wavelet Transform (UDWT) with Morlet wavelet based De-noising method is used to denoise the signal. Then this denoised signal is decomposed by Empirical Mode Decomposition (EMD) into a number of Intrinsic Mode Functions (IMF). The impulses in the signal, corresponding to the characteristic fault frequency, are seen clearly in the FFT of the IMFs. A Fast Fourier Transform (FFT), Wavelet Transform (WT), Empirical Mode Decomposition and Envelope Detection are also performed with the acquired signal and all the results are compared with the proposed method. These results clearly show the effectiveness of proposed method in detecting the faults.

**Index Terms**—Bearing fault, condition monitoring, undecimated discrete wavelet transform denoising, Morlet wavelet, empirical mode decomposition.

*Original Research Paper*  
DOI: 10.7251/ELS1317001R

## I. INTRODUCTION

EARLY fault detection in rotating machineries is useful in terms of system maintenance and process automation, which will help to save millions on emergency maintenance and production costs. Faulty bearings contribute to majority of the problems in rotating machinery than any other parts [1]. Quite naturally, fault identification of rolling element bearings has been a subject of extensive research. Bentley [2] had shown that approximately 90% of rolling element-bearing failures are related to either inner race or outer race flaws. These faults are characterized by sharp peaks at periodic intervals but they are of low energy. These signals are modulated by number of high frequency harmonic components resulting from the structural response to individual impacts. Due to this, the characteristic frequency is lost in the noise and an efficient denoising technique is

required before analyzing the signal for the characteristic fault frequency retrieval [3].

If the noise type and frequency range are known, different filters can be used for denoising [4]. However in vibration analysis, neither the noise type nor the frequency range is known. For such applications, wavelet transform has been widely used, due to its extraordinary time-frequency representation capability [5]. Different thresholding techniques are also proposed in various literatures [5-6]. The methods discussed in these literatures are suitable for smooth signals that are to be separated from Gaussian noise. But for fault diagnosis, the vibration signal is characterized with impulses and the noise in the signal is also not Gaussian.

To effectively denoise the vibration signal, Morlet wavelet based denoising method is proposed making use of the resemblance between Morlet wavelet and the impulse generated by faults [7]. Undecimated wavelet transform has an advantage over normal DWT in denoising applications, because the aliasing information tends to be lost while applying threshold. This can be overcome in UDWT based denoising techniques.

After proper denoising, the signal has to be analyzed by an efficient method. The bearing signal is a nonlinear and non-stationary. Fast Fourier transform is not efficient as the signal is amplitude modulated and FFT is meant for linear and stationary signals [8]. Wavelet Transform is designed for linear signals only and they have the leakage problem due to limited length of the window [9]. Another drawback of WT is that it uses decomposition scale for analysis and does not take the signal characteristics into consideration. Empirical Mode Decomposition decomposes the signal based on frequency content and its variation [10]. Peng et.al. [9] compared the analysis of the signal using both WT and EMD. The Fourier transform of the IMFs obtained by decomposing the signal by EMD shows better results when compared to other techniques [10].

Envelope Detection is a benchmark method for bearing diagnostics for over many years now. Envelope analysis is an analogue method for extracting the impulses from a noisy signal. Instead of the obsolete analogue method, considerable advantage can be achieved by utilizing the available digital processing techniques. One such method is the Hilbert transform which can be used for amplitude demodulation as discussed by Randall et.al [11].

A more accurate technique of bearing fault diagnosis is thus

Manuscript received 8 November 2012. Received in revised form 14 February 2013. Accepted for publication 27 February 2013.

A. S. Raj is with Real Time Systems Division, Instrumentation and Control Group, Indira Gandhi Centre for Atomic Research, Dept. of Atomic Energy, Govt. of India (corresponding author, phone: +91-44-27480500 (extn:22872), e-mail: asraj@igcar.gov.in).

N. Murali is Associate Director, Instrumentation and Control Group, Indira Gandhi Centre for Atomic Research, Dept. of Atomic Energy, Govt. of India (e-mail: murali@igcar.gov.in).

proposed in this paper by using efficient technique for both denoising and analysis of signals where other methods fail to detect the faults. UDWT denoising with Morlet wavelet as the base wavelet is performed to remove the noise. Then by EMD method IMFs are generated and their FFT vividly shows the characteristic fault frequencies present. The flow diagram of the proposed hybrid method is given in Fig. 1.

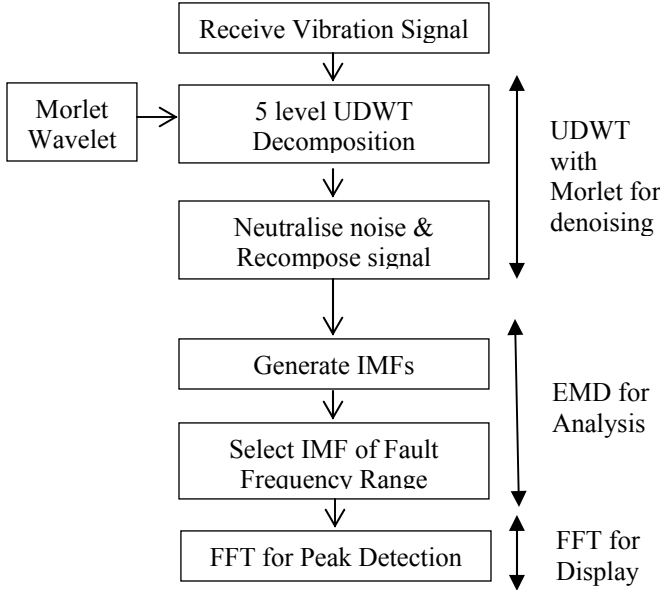


Fig. 1. Block Diagram of proposed hybrid method.

The remaining sections of the paper are organized as follows. The Undecimated discrete wavelet transform algorithm for denoising the signal is explained in the second chapter. The EMD decomposition with FFT analysis is discussed in the third chapter thereby explaining the proposed method of fault analysis. Chapter four discusses the experimental setup and data collected. The other methods for analysis like FFT, Wavelet transform, EMD and Envelope Detection are also done on the signal in chapter five. The proposed method is used to analyze the acquired signal and the results are shown in chapter six. Chapter seven discusses the results obtained with different analysis methods. Conclusion is drawn in chapter VIII.

## II. DISCRETE WAVELET BASED DENOISING

Discrete Wavelet based denoising is based on the principle of multi-resolution analysis. Multilevel discrete wavelet decomposition is carried out on the vibration signal to obtain the discrete detail coefficient and approximation coefficients.

While decomposition using an orthogonal wavelet, the energy of the signal is collected in fewer coefficients as the number of decomposition level increases. Energy is preserved because the orthogonal filters are chosen. Consequently these coefficients have become larger. The noise, being random, remains uniformly distributed over all levels. Thus due to the energy preservation, most of the coefficients coming from noise must be small. It is therefore reasonable to do denoising by setting the small coefficients equal to zero [12].

### A. Undecimated Discrete Wavelet Transform Based Denoising

While Decomposition of a signal using discrete wavelet transform, the details have some information of aliasing in different levels of decomposition. While thresholding, there is a danger of losing these aliasing information, thereby resulting in improper reconstruction of the signal. In normal wavelet transform, also known as, Decimated wavelet transform, the signal is band filtered and followed by decimation by two in each level. If the down sampling part alone is skipped, then the signal length will not be decreased and at the same time no aliasing information is present. This is a strong advantage while dealing with low signal to noise ratio signals [13].

In addition to the above mentioned property of UDWT, it also exhibits shift invariance [14]. Shift Invariance denotes that the Wavelet Transforms of the signal and its shifted versions are the same, which is not seen in an ordinary DWT. Since decimation is not done, UDWT gives more amount of information compared to DWT. The drawback of UDWT is that it requires bigger computational memory and redundancy in the coefficients.

### B. Morlet Wavelet

The wavelet based denoising method is based on orthogonal wavelets. This method assumes the noise to be independent and identically distributed and the signal to be smooth. These are not the case in bearing fault diagnosis. So the use of non-orthogonal wavelets can provide the desired noise removal.

The use of Morlet wavelet, a non-orthogonal wavelet, for bearing fault diagnosis is proved to be efficient than other regular orthogonal wavelets [11]. Morlet wavelet which is a complex wavelet and can be decomposed into real and imaginary parts as,

$$\psi_r(t) = \frac{1}{\sqrt{2\pi}} \exp\left(-\frac{\beta^2 t^2}{2}\right) \cos(2\pi\nu_0 t) \quad (1)$$

$$\psi_i(t) = \frac{1}{\sqrt{2\pi}} \exp\left(-\frac{\beta^2 t^2}{2}\right) \sin(2\pi\nu_0 t) \quad (2)$$

where  $\nu_0$  is a constant, and  $\beta$  is a shape parameter, used for balancing the time resolution and the frequency resolution of the Morlet wavelet. In general only the real part of the Morlet wavelet is used. From the equation of the Morlet wavelet, one can see that the real part of the wave is nothing but a cosine signal which decays exponentially on both sides of the y axis, which is similar to the impulse generated in faulty bearings. The optimal selection of shape factor  $\beta$  is done by Shannon entropy analysis [7]. The spectra, coherence, cross covariance and time delay functions are smoother and less noisy in high frequency band with the use of Morlet wavelet.

## III. EMPIRICAL MODE DECOMPOSITION

The empirical mode decomposition method is necessary to deal with data from non-stationary and nonlinear process. This

method decomposes the signal into a number of simple intrinsic mode of oscillations, known as Intrinsic mode functions (IMF).

The IMF has variable amplitude and frequency as functions of time. With this property, the decomposition procedure is defined by Huang vividly with examples [15].

Certain IMFs may have a sudden change in waveform at the extremes of the graph. This is called as End Swing. This may eventually propagate inward and corrupt the whole signal span leading to undesirable IMFs in the EMD process. This end swing affects especially the low frequency components. The cause of this behavior is the inherent problem in the spline fitting. This problem can be avoided by proper selection of IMFs [9].

#### IV. EXPERIMENTAL SETUP

The vibration data that was used for analysis is obtained from CWRU bearing data center [16]. Reliance Electric's 2 hp motor along with a torque transducer, dynamometer and control electronics constitute the test setup. The specifications of the 6205-2RS-JEM SKF deep groove ball bearing are given in Table I. With the help of electrostatic discharge machining, faults of sizes 0.007 and 0.021 inches are made. The vibration data is collected using accelerometers placed at 3'o'clock position. The data was sampled at a frequency of 12 kHz. The rotational frequency ( $F_r$ ) is 29 Hz.

When a fault occurs in a bearing either at inner race (IR) or

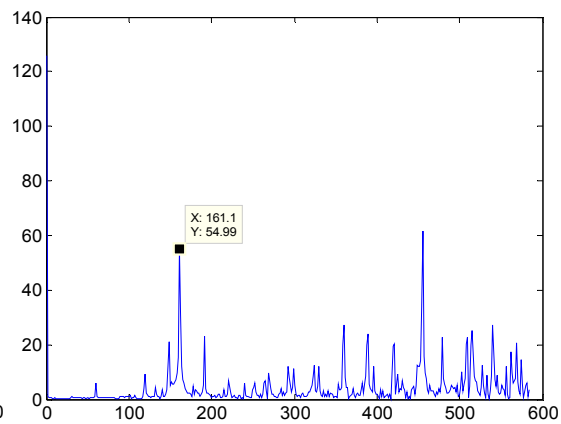
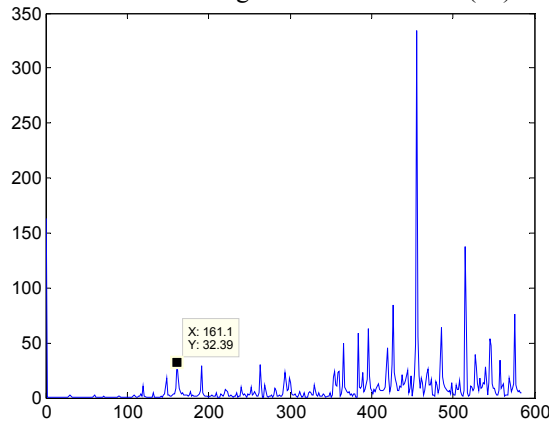


Fig. 2. FFT of Inner Race (IR) fault of a) 0.007" and b) 0.021". Freq. Resolution: 0.582 Hz.

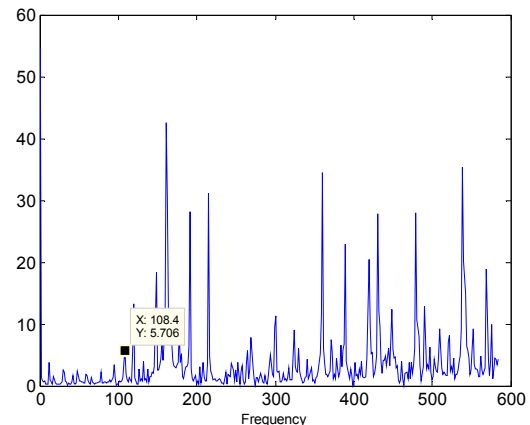
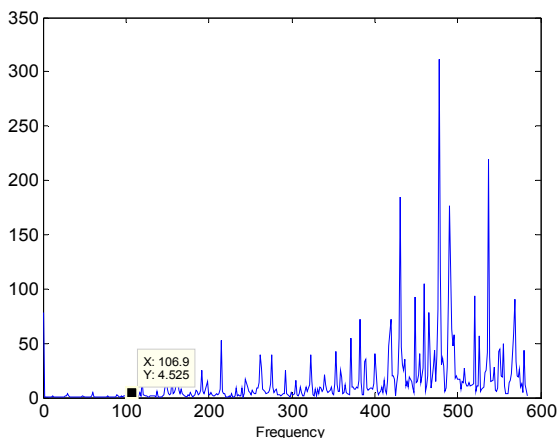


Fig. 3. FFT of Outer Race (OR) fault of a) 0.007" and b) 0.021". Freq. Resolution: 0.582 Hz.

outer race (OR), impulses of vibration are created at specific frequency. These characteristic frequencies for different faults are given by formulas in [17].

TABLE I  
BEARING DETAILS

Parameters	Values (Inches)
Inner Race (IR) Diameter	0.9843
Outer Race (OR) Diameter	2.0472
Thickness	0.5906
Ball Diameter	0.3126
Pitch Diameter	1.5370

With the required values specific for the bearing is listed in Table I. The characteristic frequency for inner race and outer race faults are 162.19 Hz and 107.36 Hz respectively.

#### V. BEARING FAULT DIAGNOSIS

##### A. Analysis using FFT and WT

Four sets of data are obtained from bearing data center with different faults, namely Inner Race faults of 0.007 and 0.021 inches thick and outer race faults of 0.007 and 0.021 inches thick.

The Figs. 2 and 3 show the FFT of these acquired data. It is noted that peak is not visible at the characteristic frequency of outer race faulty signal. The signal with inner race fault of size 0.21" alone is detected with a peak at fault frequency.

Wavelet analysis is a good technique for impulse detection in bearing fault as it is applicable for non-stationary signals also. Five-level decomposition with DWT based on Daubechies-4 wavelet is done on the filtered signal. The input signal is divided with respect to frequency bands by this

decomposition and named as Approximation (A) and Detail (D) coefficients. The FFT plots of those Details which constitute our interested area of fault frequencies are plotted in Figs. 4 and 5. It can be seen that the OR fault's characteristic frequency is not seen clearly.

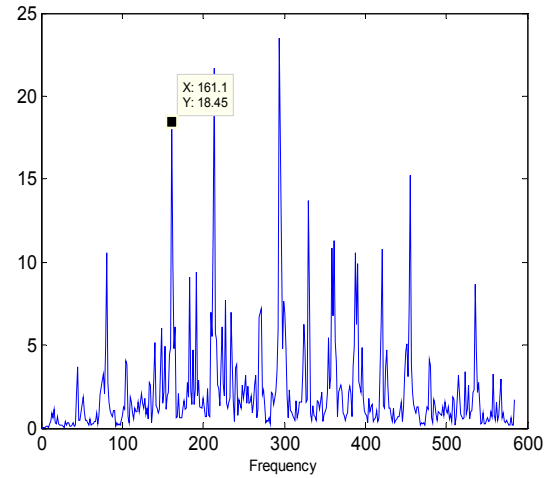
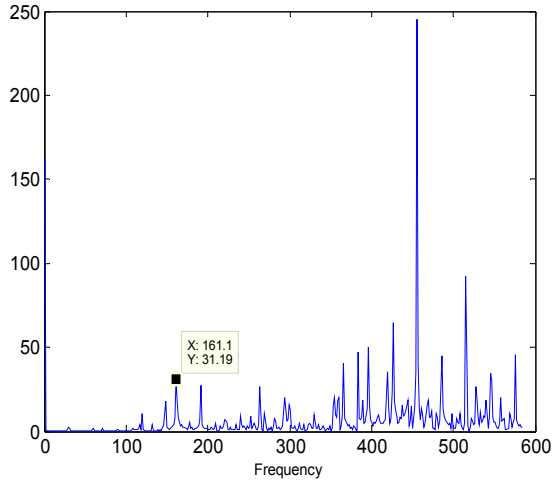


Fig. 4. FFTs of 3<sup>rd</sup> Detail (D3) of IR fault of a) 0.007" and b) 0.021". Freq. Resolution: 0.582 Hz.

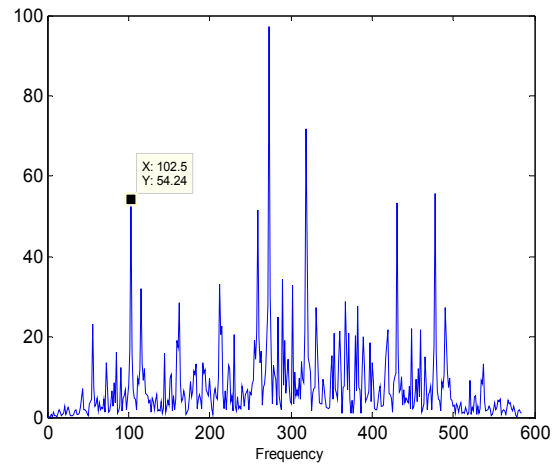
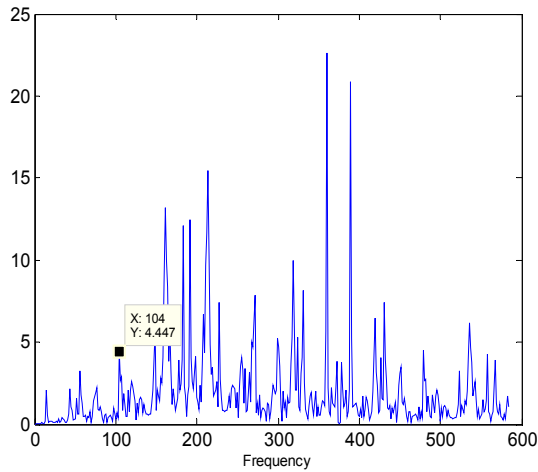


Fig. 5. FFTs of 3<sup>rd</sup> Detail (D3) of OR fault of a) 0.007" and b) 0.021". Freq. Resolution: 0.582 Hz.

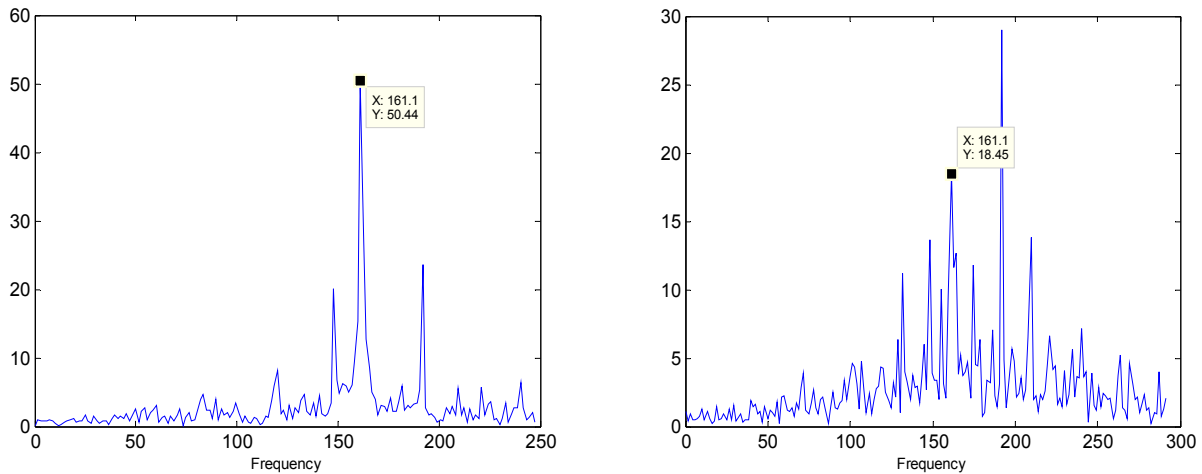


Fig. 6. FFT of 3<sup>rd</sup> IMF of IR fault of a) 0.007'' and b) 0.021''. Freq. Resolution: 0.582 Hz.

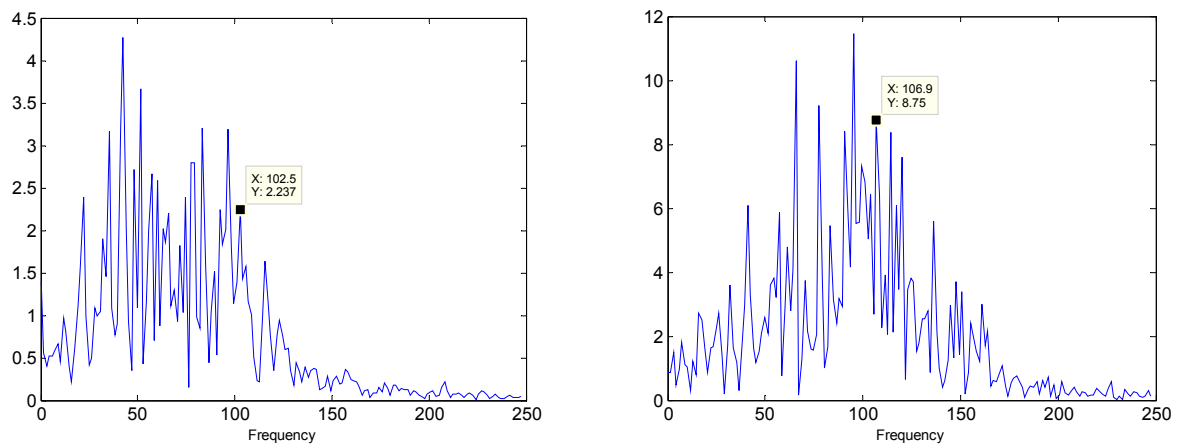


Fig. 7. FFT of 3<sup>rd</sup> IMF of OR fault of a) 0.007'' and b) 0.021''. Freq. Resolution: 0.582 Hz.

### B. Analysis Using EMD

Empirical Mode Decomposition based analysis is performed on the signal next. In EMD, the signal is decomposed into several Intrinsic Mode Functions. The FFTs of these IMFs with the respective characteristic defect frequency peak is shown in Figs. 6 and 7. The fault frequencies record a distinctive high peak in IR faulty signal but not so for OR faulty signal.

### C. Envelope Detection

Due to inherent slip in all bearings, there is a fundamental change in the characteristic of the signal. Due to these inherent slips, the diagnostic information is not obtained from other frequency analyses of raw signals and envelope analysis is often able to extract the required impulses. In digital domain, Envelope Detection is done by the using Hilbert transform which has been proved to provide sufficiently better results comparatively.

The Figs. 8 and 9 show the FFT of envelope Detection done on the four faulty signals obtained as mentioned earlier. It can be seen that this traditional method also fails for the OR faulty signal of fault size 0.007''.

## VI. ANALYSIS BY UDWT DENOISING USING MORLET WAVELET AND EMD

From chapter V, it is clear that all the methods, i.e., FFT, WT, EMD and Envelope Detection have failed to detect fault frequencies for OR fault. High noise ridden signal is common in vibration analysis and this paper proposes a novel method for such noisy signal. Because of the high noise, a Morlet wavelet based UDWT denoising followed by EMD decomposition is preferred.

As the OR fault of 0.007'' is difficult to identify, this faulty signal alone was taken for analysis using this proposed new hybrid method. While denoising, hard thresholding with a limit of 0.2 units is applied. This denoised signal is then analyzed with EMD. Fig. 10 shows how the UDWT based denoised signal has impulses that are not visible with earlier methods.

Instead of using normal DWT for denoising, Undecimated Discrete Wavelet Transform is used for better results. Fig. 10(a) shows the DWT based denoised signal analyzed with EMD and FFT of the 2<sup>nd</sup> IMF is shown. It can be seen that DWT denoised signal has a peak at 98 Hz and not at the expected frequency of 108 Hz.

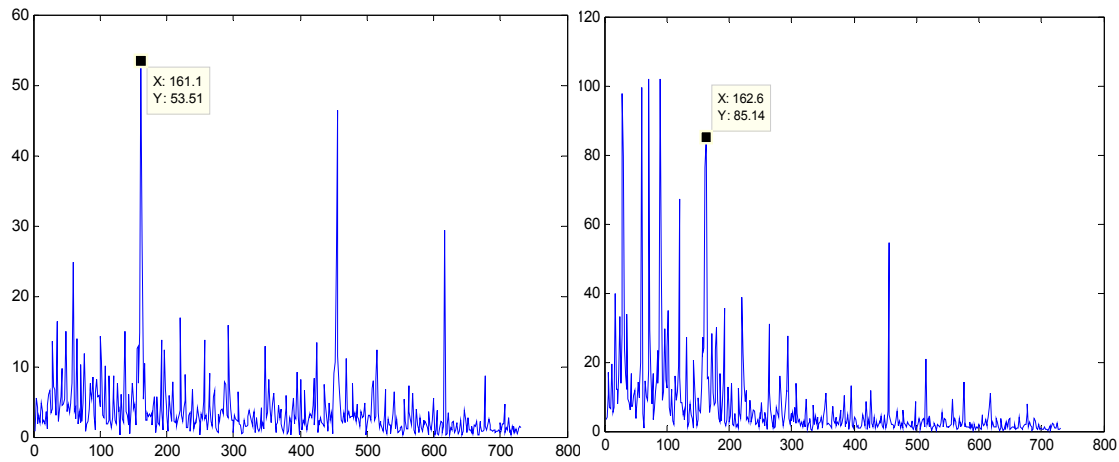


Fig. 8. FFT of envelope analysis of IR fault of a) 0.007'' and b) 0.021''. Freq. Resolution: 0.582 Hz.

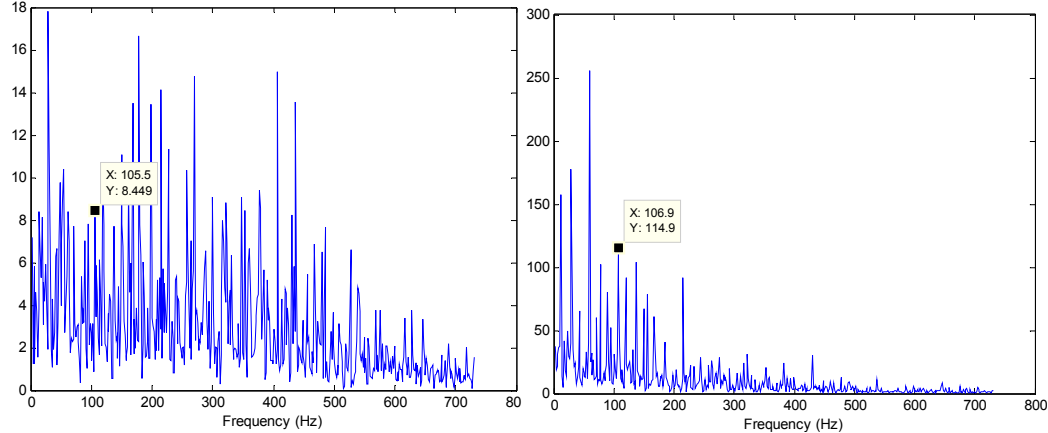


Fig. 9. FFT of Envelope analysis of OR fault of a) 0.007'' and b) 0.021''. Freq. Resolution: 0.582 Hz.

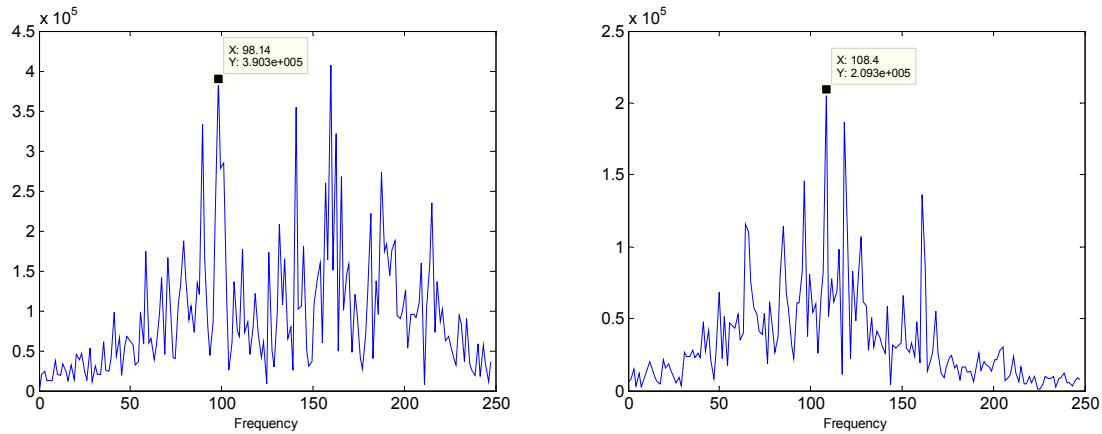


Fig. 10. FFT of the 2<sup>nd</sup> IMF obtained from a) DWT based Denoised signal and b) UDWT based Denoised signal (analysis as per the proposed method). Freq. Resolution: 0.582 Hz.

Fig. 10(b) shows the vibration signal analyzed by the proposed new method of Morlet wavelet UDWT de-noising and EMD based analysis. From the results shown in the figures 2-10, it can be clearly seen that the proposed method alone works excellently and can be used for signals with very low SNR.

## VII. DISCUSSIONS

The Fourier Transform based methods assume that the signal can be decomposed into multiple components where only the sinusoidal pattern is permissible for each component.

Therefore, when dealing with vibration signals of bearing faults, whose patterns are similar to impulses and their amplitudes vary with time, Fourier based method does not reveal its periodicity explicitly. This is shown in the above Figs. 2 and 3 that FFT is not able to detect the impulses hidden in noise.

Figs. 4 and 5 depict the DWT based Denoising. It is seen that the OR fault's characteristic frequency is not visible clearly. So it is concluded that Wavelet analysis also does not provide proper diagnosis on noisy signals.

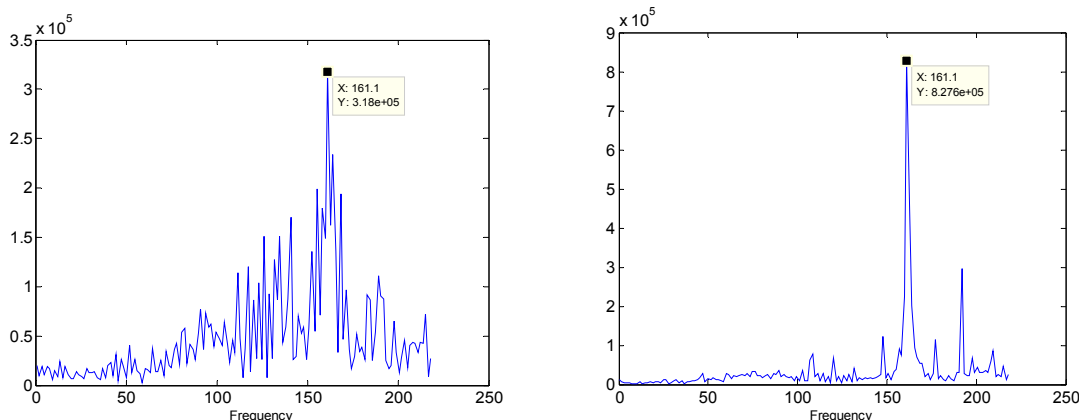


Fig. 11. Analysis by proposed method of IR fault of a) 0.007" and b) 0.021". Freq. Resolution: 0.582 Hz.

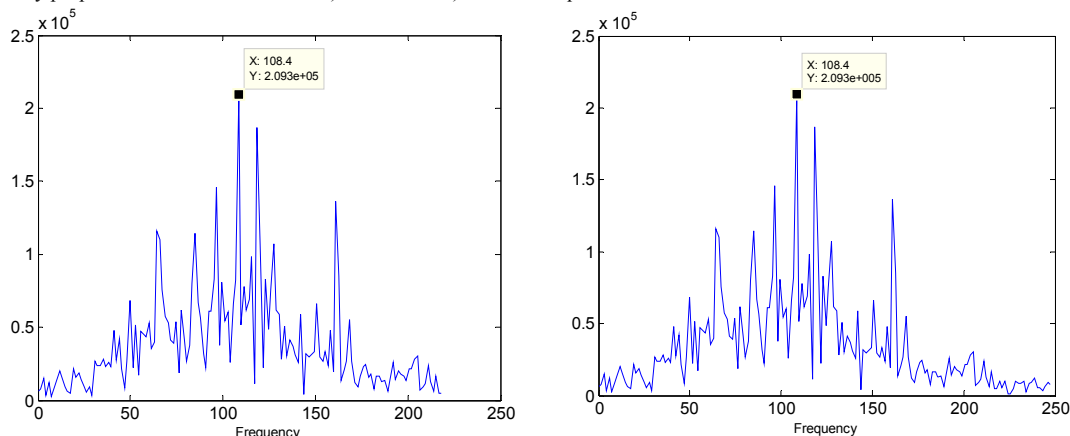


Fig. 12. Analysis by proposed method of OR fault of a) 0.007" and b) 0.021". Freq. Resolution: 0.582 Hz.

The EMD analysis of the vibration signals are shown in Figs. 6 and 7. It is apparent that for IR faults, EMD based analysis methods is able to provide satisfactory results. But for OR faults it does not. Usually detection of IR fault is difficult when compared to OR faults. Here the difficulty in detecting OR faults can be correlated to high noise in the OR faulty signal alone which is due to the noise addition during measurement. The benchmark method for bearing analysis, Envelope method, also have failed to detect the OR faults of both sizes as seen in Figs. 8 and 9.

To prove the importance of UDWT based denoising, FFTs of the 2<sup>nd</sup> IMF for both DWT and UDWT based denoised signal are shown in Fig. 10. It is evident that DWT based denoised signal has a peak at 98 Hz and not at the expected frequency of 108 Hz.

From the results shown in the Figs. 2-10(a), it is obvious that all the available methods FFT, WT, EMD, Envelope Detection and DWT based denoising fails in detecting the fault and in Fig. 10(b), the proposed method of Morlet wavelet UDWT denoising and EMD based bearing fault diagnosis alone works excellently especially for signals with very low SNR.

Figs. 11 and 12 show the analysis by the proposed method of IR fault signal and OR fault signals respectively. Thus, substantiating that the proposed method works well for all types of faults.

## VIII. CONCLUSION

The earlier methods of bearing fault diagnosis like FFT, Wavelet Transform, EMD and Envelope Detection method are shown that they are ineffective with the noisy data selected for analysis. The best denoising method, the Morlet wavelet based UDWT denoising technique, is selected for efficient denoising. Using the Undecimated Discrete Wavelet Transform based denoising, the reconstruction is better and prevents loss of valuable aliasing data. Instead of using any orthogonal wavelets for wavelet decomposition while denoising, Morlet wavelet is used for its close resemblance with the impulse. Empirical mode Decomposition method is done to analyze the denoised signal in this paper. The peaks corresponding to the characteristic frequencies of the fault can be seen clearly with the proposed novel method, which were hidden in the noise in the earlier methods.

## ACKNOWLEDGEMENT

The authors would like to thank Case Western Reserve University for providing free access to the bearing vibration experimental data from their website [16].

## REFERENCES

- [1] Albrechet,P.F., McCoy,R.M., Owen.E.L., "Assessment of reliability of motors in utility applications", *IEEE Trans. on energy conservation*, Vol.EC-1,No-1, March 1986.

- [2] D.Bently, "Predictive maintenance through the monitoring and diagnostics of rolling element bearings", Bently Nevada Co., Application Note 44, pp 2-8, 1989.
- [3] A.S.Raj, N.Murali,"Early Classification of Bearing Faults using Morphological operators and Fuzzy Inference", *IEEE Trans. Industrial Electronics*, vol.60, no.2, pp.567-574,2013
- [4] S.Sophocles, J.Orfanidis, "Introduction to signal processing", Prentice hall, 1996.
- [5] Donoho,D.L., "Denoising and Soft thresholding", *IEEE Trans. Inf. Theory*, vol.41, no.3,1995.
- [6] Pan.Q., Zhang.L.,Dai.G., Zhang.H., "Two denoising methods by wavelet transform", *IEEE Trans. Signal processing*, 47(12), 1999.
- [7] Lin.J., and Qu.L., "Feature Extraction based on Morlet wavelet and its application for mechanical fault diagnosis", *J. Sound and Vibration*, vol.234, no.1, 2000.
- [8] Rai.V.K.,Mohanty.A.R., "Condition Monitoring techniques for rolling element bearing: an overview ", *Proc. Role of NDE in Modern mainTenance Management*, IACR, 2005.
- [9] Peng.Z.K.,Tse.P.W., Chu.F.L., "A comparison study of improved Hilbert-Huang transform and Wavelet Transform: application to fault diagnosis for roller bearing", *Mechanical Systems and Signal Processing*, vol.19, 2005.
- [10] Rai.V.K.,Mohanty.A.R., "Bearing Fault Diagnosis using FFT of intrinsic mode functions in Hilbert-huang Transform", *Mechanical Systems and Signal Processing*, vol.21, 2007.
- [11] R.B. Randall, J. Antoni, S. Chobsaard, "The relationship between spectral correlation and envelope analysis in the diagnostics of bearing faults and other cyclostationary machine signals", *Mechanical Systems and Signal Processing*, vol.15, no.5, pp.945-962, 2001.
- [12] Lin.J.,Zuo.M.J., Fyfe.K.R., "Mechanical Fault detection based on the wavelet Denoising technique", *J. Vibration and Acoustics*, vol.126, no.9, 2004.
- [13] Fugal.D.L., "Conceptual wavelets in Digital Signal Processing", Space and Signals technical publishing, CA, 2009.
- [14] Undecimated wavelet transform for Image Denoising, UNR Computer Vision Laboratory,
- [15] <http://www.cse.unr.edu/CRCDD/Summer02/aglikal/index.html>.
- [16] Huang.N.E.,Shen.Z., Long.S.R., "The empirical mode decomposition and the Hilbert transform for nonlinear and non-stationary time series analysis", *Proc. Royal Society of London Series A*, 454, 1998.
- [17] Bearing Data center, <http://www.eecs.case.edu/laboratory/bearing>, Case Western Reserve University.
- [18] Collacott.R.A., "Vibration monitoring and Diagnostics", Gorge Godwin ltd, London, 1976.

# Combined Discrete Space Voltage Vector with Direct Torque Control for Bearingless Brushless DC Motor and Closed-Loop Suspended Force Control

Zhanshi Sheng, Xiaolian Wang, Fei Tan, and Weiran Wang

**Abstract**—In order to improve the performance of bearingless brushless DC motor, a closed-loop suspended force controller combining the discrete space voltage vector modulation is applied and the direct torque control is presented in this paper. Firstly, we increase the number of the control vector to reduce the torque ripple. Then, the suspending equation is constructed which is spired by the direct torque control algorithm. As a result, the closed-loop suspended force controller is built. The simulated and experimental results evaluate the performance of the proposed method. The more advantage is that the proposed algorithm can achieve the fast torque response, reduce the torque ripple, and follow ideal stator flux track. Furthermore, the motor which implants the closed-loop suspended force controller cannot only obtain the dynamic response rapidly and displacement control accurately, but also has the characteristics of bearingless brushless DC motor (such as simple structure, high energy efficiency, small volume and low failure rate).

**Index Terms**—Bearingless brushless DC motor, direct torque control, discrete space voltage vector modulation, closed-loop suspended force control.

*Original Research Paper*

DOI: 10.7251/ELSI317009S

## I. INTRODUCTION

THE bearingless brushless DC motor is a new kind of motor, which has two windings fixed in the stator. One winding is used to control system's torque, and the other is used to provide the suspension. The bearingless brushless DC motor has several

advantages, such as simple structure, low fault-rate, small volume and high efficiency of energy conversion. Furthermore, the motor has high speed because its rotor suspends in the air. Those merits make the motor popular in industrial community including medical industry, aerospace and chemical process.

Direct torque control (DTC), the most advanced AC drive technology, has been used in the bearing brushless DC (BLDC) motor recently [1]–[4]. Reference [5] deduced the mathematical formulas to describe the suspended force of bearingless brushless DC motor based on the principle of bearingless permanent magnet synchronous motor. Those equations have laid the foundation for the DTC. Reference [6] proposed a basic control method for the bearingless brushless DC motor. They divided the system into the torque part and suspension part by using the theory of independent suspension subsystem. The torque part was managed by the traditional double closed loop controller, and the suspension part was manipulated by the hysteresis current controller. The shortcoming of the method is that the precision is low and its speed is slow. The DTC has been used in brushless DC motor, which solves the difficulties of the non-sine and shut-off phase [7]–[10]. But it has not been used in the bearingless brushless DC motor. In order to improve the performance of bearingless brushless DC motor, the DTC which combines the discrete space voltage vector (DSVMDTC) is presented in this paper. The simulations evaluate the proposed method.

## II. THE SUSPENDED FORCE MODEL OF BEARINGLESS BRUSHLESS DC MOTOR

The air-gap flux of bearingless brushless DC motor consists of three parts: the permanent magnetic potential of rotor, the current magnetic potential of torque winding, and the current magnetic potential of suspended winding. The permanent magnetic potential of rotor and the current magnetic potential of torque winding are the square wave. The permanent magnetic potential of rotor changes with the rotor's position varying. Moreover, the current magnetic potential of torque winding has step change with the sector difference. So the space distribution of air-gap flux is very complex. In order to simplify the deduced process, the hypothesis is made by referring to [11].

Manuscript received 7 April 2013. Received in revised form 23 May 2013. Accepted for publication 5 June 2013.

This work was supported by the priority academic program development of Jiangsu higher education institutions and research and innovation plan of university graduate in Jiangsu province (CXLX11\_0586).

Zhanshi Sheng is with the School of Electrical and Information Engineering, JiangSu University, Zhenjiang 212013, China (corresponding author, phone:+135-05-286-768; e-mail: ymcom001@hotmail.com).

Xiaolian Wang is with the School of Electrical and Information Engineering, JiangSu University, Zhenjiang 212013, China.

Fei Tan is with the School of Electrical and Information Engineering, JiangSu University, Zhenjiang 212013, China.

Weiran Wang is with the School of Electrical and Information Engineering, JiangSu University, Zhenjiang 212013, China.

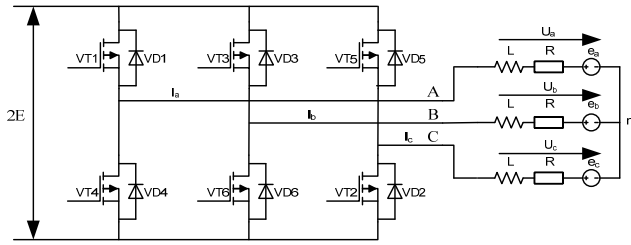


Fig. 1. The main circuit of brushless DC motor control system.

The Fig. 1 is a typical main circuit of brushless DC motor, which is a square wave control system. Controller triggers the inverter transistor according to the position sensor's information.

A phase axis is set as the  $x$  axis and the angle between the  $x$  axis and the clockwise of  $d$ -axis of the rotor is defined as the angle of rotor  $\theta$ . The symbols a, b and c are used to represent the on/off condition of the three-phase winding A, B and C [12].

The flux of stator air gap is:

$$F = F_t + F_1 + F_f \quad (1)$$

where  $F_t$  is the flux which is produced by the current through torque control winding and this flux is a phase change function;  $F_1$  is the flux which is produced by the current through suspension control winding and its value is  $F_1 = F_f \cos(\theta - \theta_1)$ ;  $F_f$  is the flux which is produced by the permanent magnet and its value also phase-change.

The mathematical model of suspension force in bearingless brushless DC motor is different under the different modes of the torque windings. It causes the difficulty in decoupling control of suspension part. So it needs to establish a uniform suspension control model. A parameter P is defined to denote the state variable, and the value is relevant to the angle of rotor. The values of the P are shown in the Table I:

P	0	1	2	3	4	5
a	0	-1	-1	0	1	1
b	1	1	0	-1	-1	0
c	-1	0	1	1	0	-1

In Table I, a, b, c are defined as three-phase torque control switch's state on/off. Taking the A phase for example, a=0 means the two switching tubes (up bridge arm and down bridge arm) of A phase are all turned-off; a=1 means the up bridge arm is turned-on and the down bridge arm is turned-off; a=-1 means the up bridge arm is turned-off and the down bridge arm is turned-on. The suspension control model of bearingless brushless DC motor is defined as follows:

$$F_x = \frac{rh\mu_0}{2l_{eg}^2} \left[ 4F_f F_2 \cos(\theta_1 - 2\theta_r) + 2\sqrt{3}F_1 F_2 \sin\left(\theta_1 - \frac{P\pi}{3}\right) \right] \quad (2)$$

$$F_y = -\frac{rh\mu_0}{2l_{eg}^2} \left[ 4F_f F_2 \sin(\theta_1 - 2\theta_r) - 2\sqrt{3}F_1 F_2 \cos\left(\theta_1 - \frac{P\pi}{3}\right) \right] \quad (3)$$

Where  $r$  is the radius of rotor,  $h$  is the length of axial,  $l_{eg}$  is the length of air gap between the stator and rotor,  $F_t$  is the torque flux which produced by the current through the torque winding,  $F_2$  is the suspended flux which produced by the current through the suspension winding,  $F_f$  is the flux which produced by the permanent magnet,  $\theta_1$  is the phase of suspended flux's base wave,  $\theta_r$  is the angle of rotor,  $\theta_t$  is the phase of torque flux's base wave.

### III. DIRECT TORQUE CONTROL OF THE BEARINGLESS BRUSHLESS DC MOTOR

#### A. The State of the Inverter for Bearingless Brushless DC Motor

We use six numerals to express the states of six switching tubes in BLDC-DSVM-DTC. Each numeral expresses one switching tube's state. Zero (0) denotes the turn-off and one (1) means turn-on. So the six voltage vectors  $V_1, V_2, V_3, V_4, V_5, V_6$  are (100001), (001001), (011000), (010010), (000110), (100100) and the zero vector  $V_0$  is (000000) as shown in Fig. 2.

The stator flux is complex in the BLDC-DTC. Under the linear condition, the flux leakage can be ignored. Then, the stator flux  $\psi_s$  is the vector sum of the armature flux  $\psi_a$  and the rotor flux  $\psi_f$ .

$$\psi_s = \psi_a + \psi_f \quad (4)$$

The  $\psi_f$  is produced by rotor permanent magnet and the value is constant under the linear condition. The  $\psi_a$  is produced by stator current and its value always varies. The phase angle of stator current can be deduced from the state of back-EMF.

#### B. Discrete Voltage Space Vector Modulation

The more the voltage space vectors use, the better the tracking effect is. As a result, the track of synthesis flux will be closed to the ideal track. This is the idea of SVPWM. But the computational burden will increase, which reduces the real-time performance of system. To overcome this problem, the DTC combining the discrete voltage space vector modulation is presented (DSVM-DTC) and the finite vectors are used to compose the new vector in a cycle. The method can get the better control effect and reduce the torque ripple greatly [13].

There are m basic voltage vectors in one cycle T and one

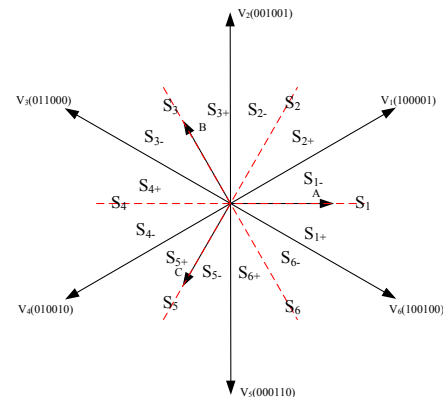


Fig. 2. Voltage vector synthesis.

basic voltage vector works T/m. It actually gets the duty cycle which can change from 1/m to 1. As shown in Fig. 3, there are four basic voltage vectors when system works in sector  $S_1$ . Then, more than 50 new voltage vectors can be composed in different duty cycle. The vectors which are perpendicular to the track of flux are selected. Then the best vector can be determined according to the sign of flux and torque.

The 9 hysteresis comparators are selected to get the flux sign and 8 hysteresis comparators are used to get the torque sign. Due to the number of the voltage vectors increase in one cycle, it is possible to refine flux and torque condition and select the best vector. The Fig. 4(a) is flux hysteresis comparison device which has nine layers. Flux difference=given Flux—real Flux.  $\varepsilon_{1\psi}, \varepsilon_{2\psi}, \varepsilon_{3\psi}, \varepsilon_{4\psi}$  are hysteresis tolerances. If the Flux difference  $\Delta\psi > \varepsilon_{4\psi}$ , the given Flux is much greater than the real Flux and it need increase the flux greatly; If the Flux difference  $\Delta\psi > \varepsilon_{3\psi}$ , the given Flux is greater than the real Flux and it need increase the flux. If the Flux difference  $\Delta\psi > \varepsilon_{1\psi}$ , the given Flux is greater than the real Flux slightly and it need increase the flux slightly. Similar to the upper condition, the sign can be got when  $\Delta\psi < -\varepsilon_{1\psi}, \Delta\psi < -\varepsilon_{2\psi}, \Delta\psi < -\varepsilon_{3\psi}, \Delta\psi < -\varepsilon_{4\psi}$ , but the flux should be decreased. The Fig. 4(b) is torque hysteresis comparison device which has eight layers. Torque difference=given Torque—real Torque.  $\varepsilon_{1T}, \varepsilon_{2T}, \varepsilon_{3T}, \varepsilon_{4T}$  are hysteresis tolerances and the state analysis of torque is similar to the flux.

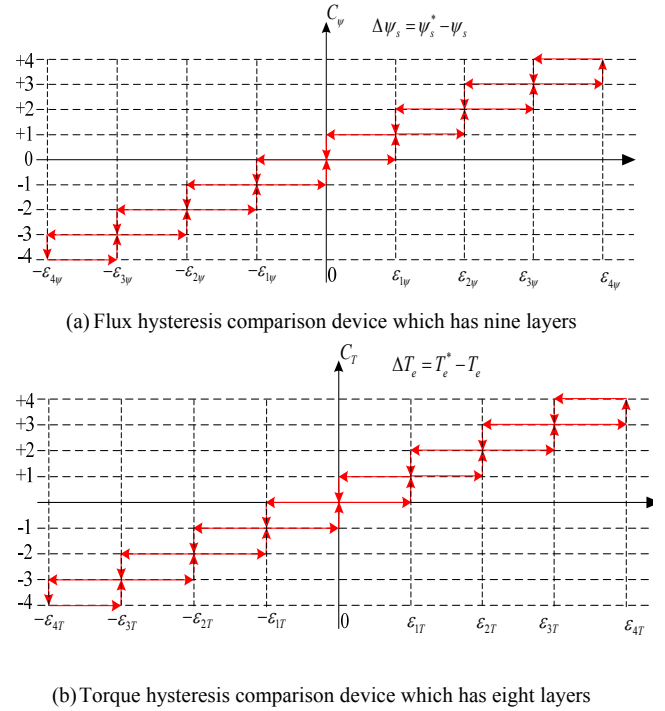


Fig. 4. Hysteresis comparison device which has multiply layers.

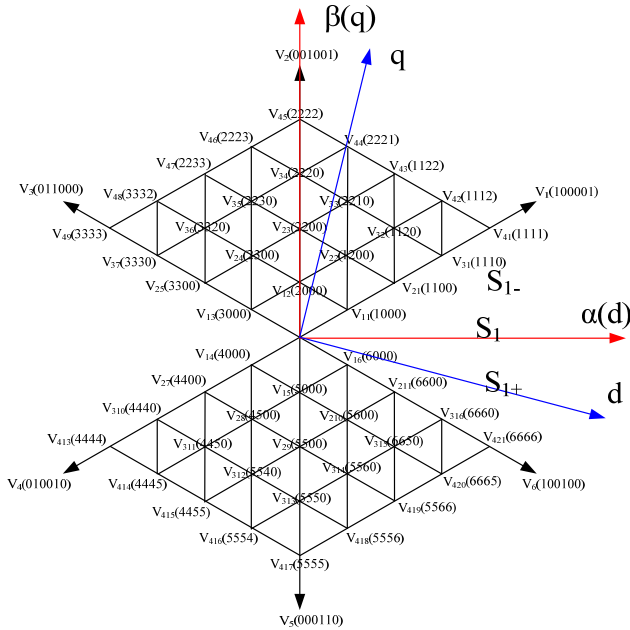


Fig. 3. Sector  $S_1$  ( $S_{1-}, S_{1+}$ ) of the vector choose.

In order to make the best use of voltage vector, the speed can be segmented as several parts. Then the refining methods can be used in the low-speed part and high-speed part (the refining sector divides the original sector into two parts equally). As shown in Fig. 3, the 6 sectors system is segmented into 12 sectors system equally. The refining sector can restrain torque ripple further by locating the flux at the sector. Then the prefect control effect can be achieved.

#### IV. THE CLOSED-LOOP SUSPENSION FORCE CONTROL OF BEARINGLESS BRUSHLESS DC MOTOR

The traditional algorithm adjusts the flux of suspended force by using the current of suspension winding. This pattern can get the amplitude and direction of suspended force indirectly. But it is an open-loop algorithm, so the precision is low and the response is slow. Inspired by the direct torque control, the suspended force can be regarded as amplitude which can be adjusted according to  $\psi_2$ . And the phase angle depends on the state of inverter and rotor angle. The state of inverter is related to the rotor position [15].

Deduced by (2) and (3),

$$F_\alpha = k_{m1}\psi_f\psi_2 \cos(\theta_l - 2\theta_r) + k_{m2}\psi_f\psi_2 \sin\left(\theta_l - \frac{P\pi}{3}\right) \quad (5)$$

$$F_\beta = -k_{m1}\psi_f\psi_2 \sin(\theta_l - 2\theta_r) + k_{m2}\psi_f\psi_2 \cos\left(\theta_l - \frac{P\pi}{3}\right) \quad (6)$$

The variation of flux produced by the suspension control winding can be known when the synthetic suspension force vector changes from  $k^{\text{th}}$  to  $(k+1)^{\text{th}}$ .

The synthetic suspended force vectors at  $k$  and  $k+1$  are:

$$F(k) = |F(k)| \angle (\theta_l - 2\theta_r) + |F_p(k)| \angle \left(\theta_l - \frac{P\pi}{3}\right) \quad (7)$$

$$F(k+1) = |F(k+1)| \angle (\theta_l - 2\theta_r + \Delta\theta) + |F_p(k+1)| \angle \left(\theta_l - \frac{P\pi}{3} + \Delta\theta\right) \quad (8)$$

Decompose the suspended force of  $k$  and  $k+1$  moment in  $\alpha\beta$  coordinate system and the difference of suspended force can be formulated as:

$$\Delta F = F(k+1) - F(k) \quad (9)$$

The component in  $\alpha\beta$  coordinate is:

$$\begin{aligned} \Delta F_\alpha &= F_\alpha(k+1) - F_\alpha(k) \\ &= k_{f1} |\psi_{s2}(k+1)| \cos(\theta_i + \Delta\theta) \cos(2\theta_r) \\ &\quad + k_{f1} |\psi_{s2}(k+1)| \sin(\theta_i + \Delta\theta) \sin(2\theta_r) \\ &\quad + k_{f2} |\psi_{s2}(k+1)| \sin(\theta_i + \Delta\theta) \cos\left(\frac{P\pi}{3}\right) \\ &\quad - k_{f2} |\psi_{s2}(k+1)| \cos(\theta_i + \Delta\theta) \sin\left(\frac{P\pi}{3}\right) \\ &\quad - k_{f1} |\psi_{s2}(k)| \cos\theta_i \cos(2\theta_r) \\ &\quad - k_{f1} |\psi_{s2}(k)| \sin\theta_i \sin(2\theta_r) \\ &\quad - k_{f2} |\psi_{s2}(k)| \sin\theta_i \cos\left(\frac{P\pi}{3}\right) \\ &\quad + k_{f2} |\psi_{s2}(k)| \cos\theta_i \sin\left(\frac{P\pi}{3}\right) \end{aligned} \quad (10)$$

$$\begin{aligned} \Delta F_\beta &= F_\beta(k+1) - F_\beta(k) \\ &= -k_{f1} |\psi_{s2}(k+1)| \sin(\theta_i + \Delta\theta) \cos(2\theta_r) \\ &\quad + k_{f1} |\psi_{s2}(k+1)| \cos(\theta_i + \Delta\theta) \sin(2\theta_r) \\ &\quad + k_{f2} |\psi_{s2}(k+1)| \cos(\theta_i + \Delta\theta) \cos\left(\frac{P\pi}{3}\right) \\ &\quad + k_{f2} |\psi_{s2}(k+1)| \sin(\theta_i + \Delta\theta) \sin\left(\frac{P\pi}{3}\right) \\ &\quad + k_{f1} |\psi_{s2}(k)| \sin\theta_i \cos(2\theta_r) \\ &\quad - k_{f1} |\psi_{s2}(k)| \cos\theta_i \sin(2\theta_r) \\ &\quad - k_{f2} |\psi_{s2}(k)| \cos\theta_i \cos\left(\frac{P\pi}{3}\right) \\ &\quad - k_{f2} |\psi_{s2}(k)| \sin\theta_i \sin\left(\frac{P\pi}{3}\right) \end{aligned} \quad (11)$$

Where  $k_{f1}$  is suspension force coefficient 1,  $k_{f2}$  is suspension force coefficient 2,  $\Delta\theta$  is the change angle of suspension force.

The fluxes of suspension control winding at  $k$  and  $k+1$  moment are:

$$\psi_{s2}(k) = |\psi_{s2}(k)| \angle(\theta_i) \quad (12)$$

$$\psi_{s2}(k+1) = |\psi_{s2}(k+1)| \angle(\theta_i + \Delta\theta) \quad (13)$$

Decompose the flux of suspension control winding at  $k$  and  $k+1$  moment and the flux difference of suspension control winding is:

$$\Delta\psi_{s2} = \psi_{s2}(k+1) - \psi_{s2}(k) \quad (14)$$

The component in  $\alpha\beta$  coordinate is:

$$\begin{aligned} \Delta\psi_{s2\alpha} &= \psi_{s2\alpha}(k+1) - \psi_{s2\alpha}(k) \\ &= |\psi_{s2}(k+1)| \cos(\theta_i + \Delta\theta) - |\psi_{s2}(k)| \cos\theta_i \end{aligned} \quad (15)$$

$$\begin{aligned} \Delta\psi_{s2\beta} &= \psi_{s2\beta}(k+1) - \psi_{s2\beta}(k) \\ &= |\psi_{s2}(k+1)| \sin(\theta_i + \Delta\theta) - |\psi_{s2}(k)| \sin\theta_i \end{aligned} \quad (16)$$

Substitute the (10) and (11) by (15) and (16), so

$$\begin{aligned} \begin{bmatrix} \Delta F_\alpha \\ \Delta F_\beta \end{bmatrix} &= k_{f1} \begin{bmatrix} \cos 2\theta_r & \sin 2\theta_r \\ \sin 2\theta_r & -\cos 2\theta_r \end{bmatrix} \begin{bmatrix} \Delta\psi_{s2\alpha} \\ \Delta\psi_{s2\beta} \end{bmatrix} \\ &\quad + k_{f2} \begin{bmatrix} -\sin\left(\frac{P\pi}{3}\right) & \cos\left(\frac{P\pi}{3}\right) \\ \cos\left(\frac{P\pi}{3}\right) & \sin\left(\frac{P\pi}{3}\right) \end{bmatrix} \begin{bmatrix} \Delta\psi_{s2\alpha} \\ \Delta\psi_{s2\beta} \end{bmatrix} \end{aligned} \quad (17)$$

$$\begin{bmatrix} \Delta\psi_{s2\alpha} \\ \Delta\psi_{s2\beta} \end{bmatrix} = K \left\{ k_{f1} \begin{bmatrix} \cos 2\theta_r & \sin 2\theta_r \\ \sin 2\theta_r & -\cos 2\theta_r \end{bmatrix} \begin{bmatrix} \Delta F_\alpha \\ \Delta F_\beta \end{bmatrix} + k_{f2} \begin{bmatrix} -\sin\left(\frac{P\pi}{3}\right) & \cos\left(\frac{P\pi}{3}\right) \\ \cos\left(\frac{P\pi}{3}\right) & \sin\left(\frac{P\pi}{3}\right) \end{bmatrix} \begin{bmatrix} \Delta F_\alpha \\ \Delta F_\beta \end{bmatrix} \right\} \quad (18)$$

$$K = \frac{1}{k_{f1}^2 + k_{f2}^2 + 2k_{f1}k_{f2} \left[ \sin 2\theta_r \cos\left(\frac{P\pi}{3}\right) - \cos 2\theta_r \sin\left(\frac{P\pi}{3}\right) \right]} \quad (19)$$

Equations (17) and (18) can be seen as the coordinate transformation between the flux difference and the suspended force difference. Then, the suitable space voltage vector is selected to compose the flux difference of the suspension control winding. The relationship between the suspended force difference and the flux difference of the suspension control winding is obtained. The amplitude and direction of suspension can be controlled by flux vector. In this algorithm, the suspension force is a closed-loop control and anti-interference performance of system is enhanced greatly.

## V. THE SIMULATION AND EXPERIMENT

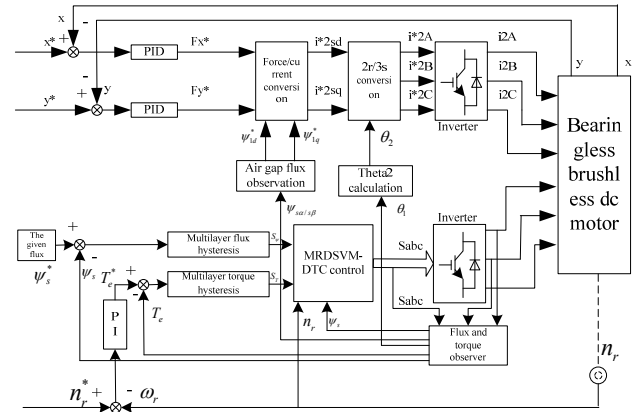


Fig. 5. BLDC-DSVM-DTC's simulation and experiment.

In this simulation, the parameters of bearingless brushless DC motor are: Rated voltage  $U = 50$  V, Rated speed  $n = 1500$  rad/min, Rated current  $I = 5$  A, the resistance of torque winding  $R_{1s} = 0.48 \Omega$ , the inductance of torque winding  $L_{1s} = 8.5 \times 10^{-3}$  H, the mutual inductance of torque winding  $L_{1m} = 0.0006$  H, the resistance of suspended force control winding  $R_{2s} = 0.42 \Omega$ , the inductance of suspended force control winding  $L_{2s} = 6.5 \times 10^{-3}$  H, the mutual inductance of suspended force control winding  $L_{2m} = 0.0004$  H, the coefficient of back EMF  $K_e = 0.075$  V·s/rad, the coefficient of rotational inertia  $J = 0.8 \times 10^{-3}$  kg·m<sup>2</sup>, the rotor quality  $m = 2.85$  kg [14].

The speed from zero to the rated speed (8000 rad/min) only needs 0.17 s and the overshoot volume is small. As shown in the Fig. 6, there are very small fluctuations at 0.17 s and the speed immediately stabilizes at rated speed.

The Fig. 7 is the typical track of stator flux. The track is not a circle. It is irregular circle when the rotor rotates to switch area. The flux will appear an obvious variation.

The Fig. 8(a) is velocity curve about DSVM-DTC and the Fig. 8(b) is torque response about the speed change. The velocity is stable at the given 1200 rad/min at 0.17 s. The velocity increases from the 1200 rad/min to 1500 rad/min at 0.25s and it is stable in 1500 rad/min at 0.31 s. As shown in the

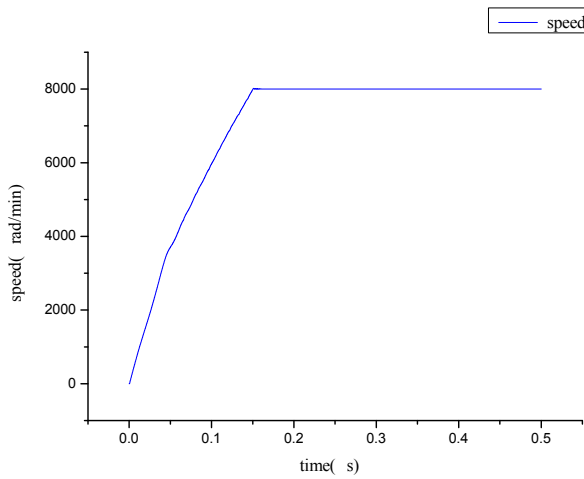
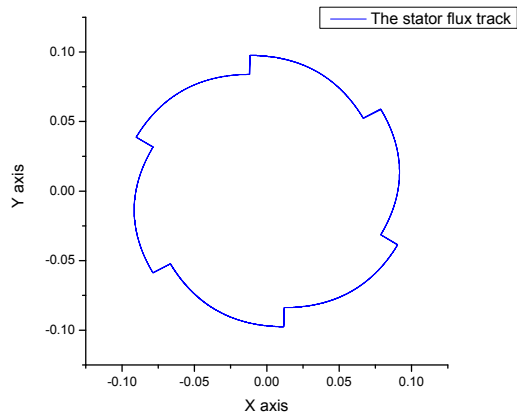
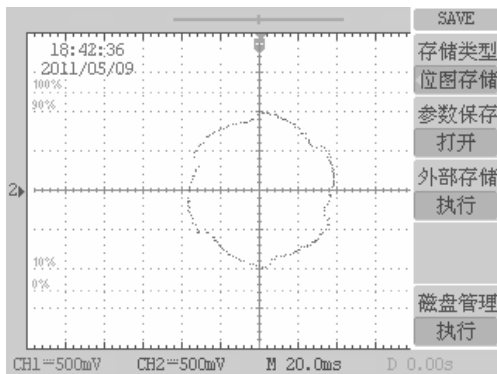


Fig. 6. Speed of BLDC-DSVMDTC's simulation.



(a) Flux track of BLDC-DSVMDTC's simulation

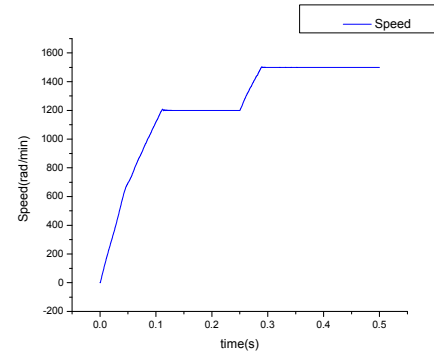


(b) Flux track of BLDC-DSVMDTC's experiment

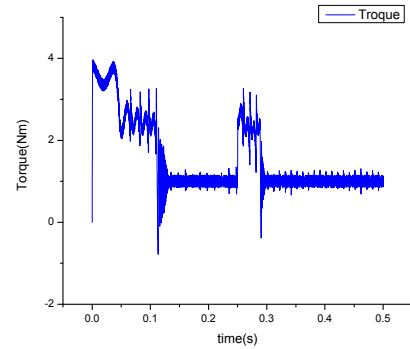
Fig. 7. The track of stator flux.

Fig. 8(b), the torque responds a 3 N·m change at 0.32 s, the system controls the torque and stabilizes at  $1 \pm 0.08$  N·m.

It means the change of velocity influences the torque greatly. The torque stabilizes only needing 0.07 s. So, the control system responds quickly and it has a good adjustment about the input change.

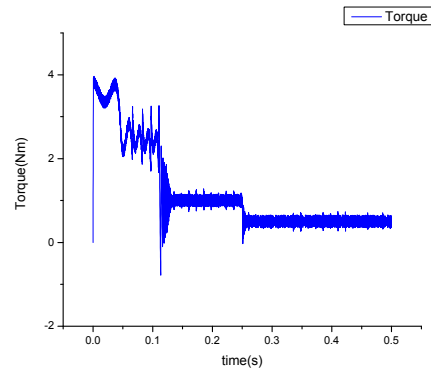


(a) Speed rose from 1200 rad/min to 1500 rad/min at 0.25 s

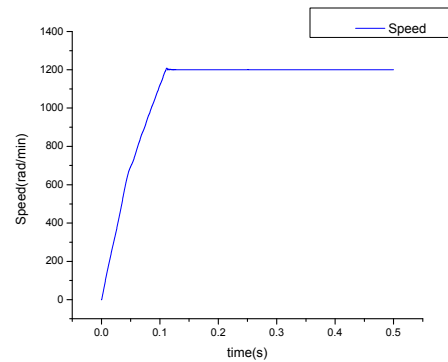


(b) The torque response when speed rose from 1200 up to 1500 rad/min at 0.25 s

Fig. 8. The response of speed and torque in the process of speed up.



(a) Torque drop from 1 N to 0.5 N at 0.25 s

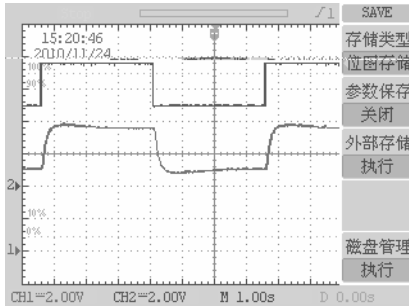


(b) The speed response when torque drop from 1 N to 0.5 N at 0.25 s

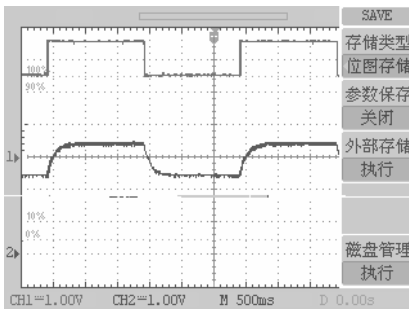
Fig. 9. The response of speed and torque in the process of torque change.

The Fig. 9(a) is torque change about DSVM-DTC and the Fig. 9(b) is speed response about the torque change.

Similar to the Fig. 8, the Fig. 9 also evaluates the fast response of the control system. It has a good adaptive performance about the input change. However, the velocity is almost not affected when the torque changes.



(a) The cycle step representation of BLDC-DSVMDTC's speed which rose from 1200 rad/s to 1500 rad/s



(b) The cycle step representation of BLDC-DSVMDTC's torque which rose from 2.5N to 3.5N

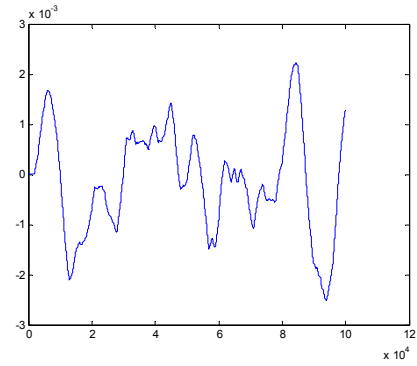
Fig. 10. Results of speed and torque change.

The result of step change in the velocity is shown in the Fig. 10(a). There is a step signal at the channel 1 of oscillograph, and its period is 7 s. The actual velocity at the channel 2 is detected by photoelectric encoder. We can see that the velocity tracks the input step signal and the overshoot is small (0.2 V). The motor only need 1.6 s to reestablish the speed. The torque step change is shown in the Fig. 10(b). It proves that the DSVM-DTC can suppress the torque ripple and keep the advantages of rapid response.

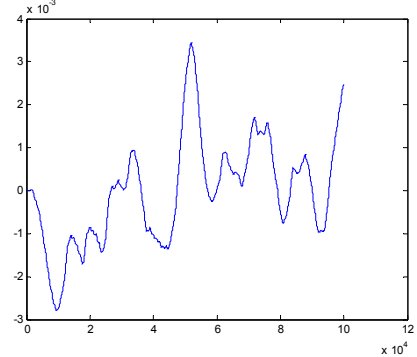
In order to demonstrate the anti-interference performance, the disturbances (1 N) are imported in  $x$ -axis and  $y$ -axis respectively. The Fig. 11(a) and Fig. 11(b) show the results. The unit is ms. It can be seen that the center and amplitude of the rotor impulse along the  $xy$  axis are 0 and  $3 \times 10^{-3}$  ms respectively. The Fig. 11(c) shows the displacement of rotor along the  $xy$  axis. The per-unit value is  $1 \times 10^{-3}$  ms/mv. The displacement of  $x$ -axis shakes by 0.5 mv as the center and  $y$  axis shakes by 0.1 mv as the center. The amplitude also is about 2.5 mv.

## VI. CONCLUSION

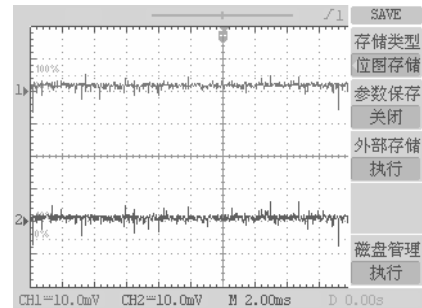
A DTC combined with the discrete space voltage vector is proposed to control the closed-loop suspended force of the bearingless brushless DC motor in this paper. The proposed algorithm controls the torque part and increases the number of vectors which are used to compose the new control vector. Comparing with the methods mentioned in the literatures, the



(a) The pulse at  $x$  axis in 10 s, the pulse unit is ms



(b) The pulse at  $y$  axis in 10 s, the pulse unit is ms



(c) The rotor displacement at  $x$  axis and  $y$  axis

Fig. 11. Results of bearingless brushless DCmotor's suspension control.

algorithm takes the characteristics of flux periodic change and the torque ripple in direct torque control into consideration. It uses the discrete space vector modulation to suppress the torque ripple and makes the ripple not affect the suspension of rotor. The more important is that the closed-loop suspended force control formula is deduced for the bearingless brushless DC motor. The simulated and experimental results show that the proposed method can get the quick response of the torque. The torque ripple is low and it can track the ideal stator flux trajectory. Furthermore, the accuracy is high and the performance of suspended force control is good. The bearingless brushless DC motor packed with the proposed method has several advantages, such as simple structure, high energy efficiency, small volume and low failure rate. So, it is suitable for the higher demand occasion of motor.

## REFERENCES

- [1] J. Gao. 2007. The Integreted Research of Direct Torque Control of Brushless DC Motors, Nanjing university of aeronautics and astronautics.

- [2] Q. T An, L. Z Sun, C Liu, L Sun. 2010. Flux linkage self-control based direct torque control of brushless DC motor, *Zhongguo Dianji Gongcheng Xuebao/Proceedings of the Chinese Society of Electrical Engineering*, Vol. 30, no. 12, pp. 86-92.
- [3] S. B Ozturk and A. H Toliyat. 2011. Direct torque and indirect flux control of brushless DC motor, *IEEE/ASME Transactions on Mechatronics*, Vol. 16, no. 2, pp. 351-360.
- [4] H. F Wei, P. P Li, G. H Liu and H. P Jia. 2009. A kind of BLDCM DTC with simplified structure, *Journal of Jiangsu University(Natural Science Edition)*, Vol. 11, pp. 606-609.
- [5] C. Jie. 2010. The Study of Bearingless and Brushless Dc Motor with Control System, Nanjing university of aeronautics and astronautics.
- [6] L. Jia. 2009. Principle and Control Techology of Bearingless Brushless DC Motors, Jiangsu university.
- [7] Z. L Yin. 2009. Direct Torque Control of Brushless DC Motors, Jiangsu university.
- [8] J. Gao, Y. W Hu, W. X Huang and Z. F Huang. 2007. The Direct Self Control of Brushless DC Motor Based on the Hexagon Locus of Stator Flux Linkage, *Proceedings of the CSEE*, Vol. 5, pp. 64-69.
- [9] X. X Liu, W. R Wang, W. 2010. DSVM and duty ratio control combined direct torque control for bearingless induction motor, 2010 Chinese Control and Decision Conference, pp. 2025-2030.
- [10] W. R Wang, X. X Liu, H. B Wang and X. Zhu. 2012. Adapted genetic algorithm and 5 levels control combined low-speed improvement Direct Torque Control, *Applied Mechanics and Materials*, Vol.130-134, pp. 426-429.
- [11] H. X Wu. 2009. Application Notes for motor drive and control ASIC, China Electric Power Press.
- [12] Q. D Guo and X. M Zhao. 2008. Brushless DC motor principles and techniques of application, China Electric Power Press.
- [13] X. M Xue. 2010. Ripple suppression method and device of brushless DC motor electromagnetic torque. CN201010118230.X.
- [14] M. S Ooshima, C. Takeuchi . 2011. Magnetic suspension performance of a bearingless brushless DC motor for small liquid pumps, *IEEE Transactions on Industry Applications*, Vol. 47, no. 1, pp. 72-78.
- [15] Z. F Huang, Y. W Hu, J. Gao, and W. X Huang. 2007. Improvement of Performance at Lower Speed of Direct Self-Control of Brushless DC Motor Based on DSP, *Electric Machines & Control Application*, Vol.4, pp. 15-19.

# A Realization of Temperature Monitoring System Based on Real-Time Kernel $\mu\text{C}/\text{OS}$ and 1-wire Bus

Haibo Pu, Lijia Xu, and Yanmei Qi

**Abstract**—The traditional temperature monitoring system generally adopt some analog sensors for collecting data and a microcontroller for processing data for the purpose of temperature monitoring. However, this back-fore ground system has the disadvantages that the system has poor real-time property and single function, the amount of sensors is not easy to expand, and the software system has a difficulty in upgrading. Aiming at these disadvantages, the system designed in this paper adopts brand-new hardware and software structures: a digital temperature sensor array is connected to 1-wire bus and communicated with a control core through 1-wire bus protocol, thus a great convenience is provided for the expansion of the sensor; a real-time operating system is introduced into the software, an application program capable of realizing various functions runs on the real-time kernel  $\mu\text{C}/\text{OS-II}$  platform. The application of the real-time kernel also provides a good lower layer interface for the late-stage software upgrading.

**Index Terms**—1-wire bus, temperature monitoring system, DS18B20,  $\mu\text{C}/\text{OS-II}$ , C8051F020.

*Original Research Paper*

DOI: 10.7251/ELS1317016P

## I. INTRODUCTION

THE traditional temperature monitoring system generally adopts an analog sensor for collecting data and a microcontroller for processing data for the purpose of temperature monitoring. However, this back-fore ground system has the disadvantages that the system has poor real-time property and single function, the amount of sensors is not easy to expand, and the software has a difficulty in upgrading. To overcome the disadvantages of poor real-time property, single function, difficulty in expansion and maintenance of the sensor and difficulty in upgrading of the software system in the traditional real-time temperature monitoring system, this paper provides a real-time temperature monitoring system (temperature Monitoring System, hereinafter called TMPSYS

for short) based on a real-time kernel  $\mu\text{C}/\text{OS}$  and a 1-wire bus. After test, the system can effectively realize multitask scheduling, and accomplish the system function. Compared with the traditional back-fore ground system, especially when adding tasks or sensor nodes, the kernel  $\mu\text{C}/\text{OS}$  with high real-time property can give a response within a short period time. The response time is mainly determined by both the selected switching frequency of  $\mu\text{C}/\text{OS-II}$  such as 50 Hz and the performance of CPU. The kernel  $\mu\text{C}/\text{OS}$  can also enable the C8051F series single-chip microcomputer to realize more complex functions. Another convenience of introducing  $\mu\text{C}/\text{OS}$  into the system is upgrading of application in the future almost does not affect the system's real-time characteristics. The sensors based on a 1-wire bus is simple and reliable in physical connection, is convenient for expansion and maintenance of a bus, and particularly suitable for monitoring multipoint temperature [1].

## II. DESIGN OF HARDWARE SYSTEM

The traditional analog sensor lies in that a sensor occupies a channel; however, the limited number of an available channel on the chip of an MCU limits the number of the sensor. Although the number of the sensor can be increased through an expansion port, when a plurality of sensors transmit data in a parallel transmission manner, electromagnetic interference between the channels is easily caused, and an expanded off-chip port cannot be compared with an on-chip port in speed and stability. However, the problem above can be better solved by adopting a digital sensor for transmitting data in a serial transmission manner [2]. Therefore, the 1-wire bus technology is adopted in the TMPSYS, and all the temperature sensors are connected to a 1-wire bus to form a sensor array, as shown in Fig. 1.

The system adopts two kinds of bus expansion technologies. The temperature acquisition parts are connected through a 1-wire bus, a simple 1-wire bus temperature sensor DS18B20 is only required to be accessed on a bus in the actual physical connection, the real-time clock adopts a DS1338 based on an I2C bus protocol, and more peripheral devices also can be connected to the I2C bus. The specific circuit diagram of the system is shown in Fig. 2.

Manuscript received 7 April 2013. Received in revised form 24 May 2013 and 9 June 2013. Accepted for publication 11 June 2013.

This work is supported by the Natural Science Project of Sichuan Education Department under Grant 12ZA277.

H. Pu, L. Xu, and Y. Qi are with the School of Information and Engineering Technology, Sichuan Agricultural University, Ya'an, China (Corresponding author is Lijia Xu, e-mail: xulijiasc@163.com).

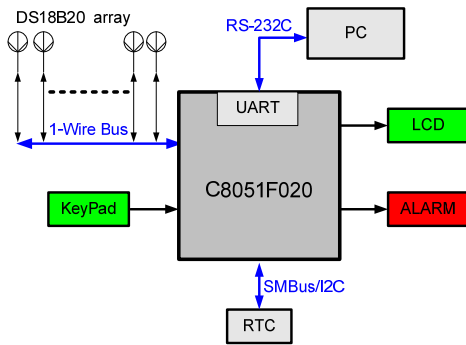


Fig. 1. Minimum system of the TMPSYS.

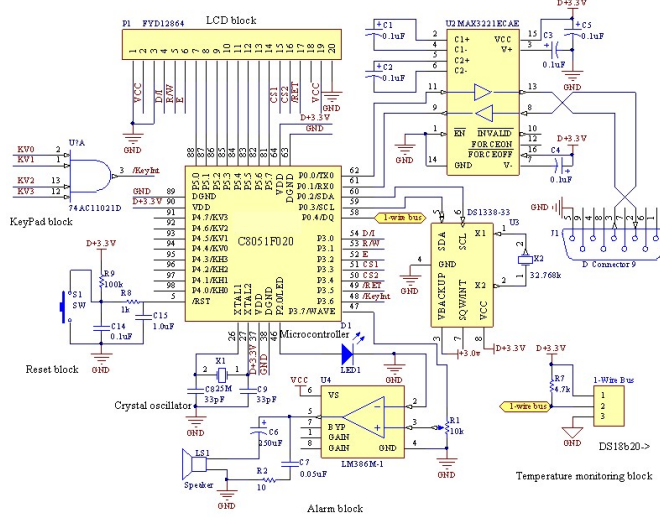


Fig. 2. Circuit diagram of the minimum system of the TMPSYS.

In Fig. 2, alarm block is used to give alarm for high or low temperature and temperature monitoring block is used to measure temperature. Crystal oscillator block is applied to produce crystal frequency for microcontroller C8051F. Reset block can reset signal when the C8051F is powered on and can cancel the reset signal until the power system stability. KeyPad block can set temperature manually. The DS1338 serial real-time clock is a low-power, full binary-coded decimal clock/calendar plus 56 bytes of NV SRAM. Address and data are transferred serially through an I2C interface. The MAX3221ECAE are 3V-powered EIA/TIA-232 and V.28/V.24 communications interfaces with automatic shutdown/wakeup features, high data-rate capabilities, and enhanced electrostatic discharge protection. FVD12864 is a liquid crystal display module used to show temperature.

#### A. C8051F Series Microcontroller

The C8051F series microcontroller is configured with a standard JTAG interface, the non-invasive on-chip debugging can be directly performed to the target system through the JTAG interface, the reading/writing operation of Flash is supported, and the JTAG logic also provides boundary scanning function for the system test [3, 4]. Under the programmed control of a boundary register, the weak pull-up functions of all pins, SFR buses and I/O ports of the device can be observed and controlled.

#### B. 1-wire Bus Temperature Sensor DS18B20

The 1-wire bus adopts a single signal wire for completing the bidirectional data transmission [5], and meanwhile, power supply is provided for the 1-wire bus device through the signal wire. A master-slave data exchange network can be formed conveniently by adopting 1-wire bus interface chips, and the number of slave devices in a network varies from a few to several thousand, and is almost unlimited theoretically. The 1-wire bus system has the characteristics of high networking speed and low cost, most devices depend entirely on power supply obtained from data lines, thus the 1-wire bus device has lower power consumption, and is a new selection of the field bus technology. The DS18B20 is a digital temperature sensor produced by the Maxim Company in USA, and has the advantages of simple structure, flexible operation and no external circuit, and the temperature warning limit can be set by users [6].

### III. DESIGN OF SOFTWARE SYSTEM

#### A. Introduction of Real-time Kernel $\mu\text{C}/\text{OS-II}$

In a traditional back-fore ground system, the application program is designed into an endless cycle, and the key operation with strong time correlation is executed through an interruption service program, thus the back-fore ground system has poorer real-time property in information processing, and the change of codes decreases the stability in response time of task level.

In the real-time system structure, the interruption service program can directly send a request of immediate execution to task-level codes. The real-time kernel can allow various task codes and the codes relatively urgent in a subprogram to run. The change of task codes does not affect the stability in response time of task level.

To ensure the real-time property of the system and the convenient subsequent software upgrading, the real-time kernel  $\mu\text{C}/\text{OS-II}$  with good stability and reliability is introduced in the system, and all the task-level codes run on the kernel platform [7].

#### B. Transplantation of Real-time Kernel $\mu\text{C}/\text{OS-II}$ on C8051F020

The  $\mu\text{C}/\text{OS-II}$  is a hard real-time kernel of an open source code, has good stability and reliability, and meets the standard of RTCA/DO-178B [8, 9]. The selected software build environment in the system is Keil  $\mu\text{Vision}$  3.53 for C51, because there is no software interruption in the C8051F020, some programs are required to be designed artificially for transplanting a kernel on an MCU without software interruption, so that the kernel can run normally.

##### 1) Configuration of System Stack and Task Stack

As shown in Fig. 3, the OSTCBStkPtr in the OS\_STK structure in the  $\mu\text{C}/\text{OS-II}$  is used for protecting a stack pointer of a task stack, and the pointer points to a contiguous region in an external data memory. A simulated stack is used for preserving formal parameters and local variables of a reentrant

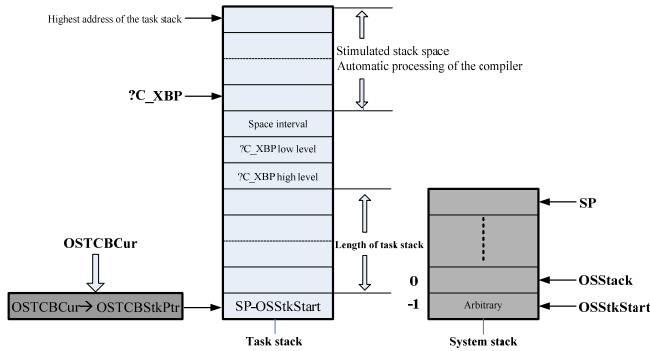


Fig. 3. Task stack frame customized for the C8051F020.

function, and grows downwards. A system stack occupies the IDATA area in a memory, and the area is the part where the data storage speed is the fastest.

During the system transplantation, to hold the variables in each task stack and the application program, the whole system is compiled in a large mode, most of the data structures are assigned in an external data memory XRAM through a compiler, and the external space has a 16-bit address (The addressing space of the C8051F020 is 0x0000-0x0FFF).

### 2) Overwriting of Portable File

The data type supported by the C8051F020 is compatible with the standard MCS-51 [10], and the two files are only required to be overwritten for use. The OS\_CPU.H includes constants and macro definition related to the processor, data type related to the compiler and codes related to the processor. The OSTaskStkInit() is only required to be corrected for initializing the task stack in the OS\_CPU.C.C, the structure of the task stack must be determined before overwriting, and all registers at the task site are preserved in the task stack.

Because many assembly language functions in the OS\_CPU\_A.ASM are invoked by C language functions in the  $\mu$ C/OS-II, thus they should be described in a principal function. And in an assembly program, a pseudo instruction "SEGMENT CODE" should be declared as a relocatable segment type, the function names are translated according to different circumstances; the symbols used in other modules should be declared with a pseudo instruction "PUBLIC", and the foreign symbols should be declared with a pseudo instruction "EXTRN".

During the late-stage application programming process, if interrupt processing is involved, the assembly codes at an interrupt entry should be written into this file for convenient unified management.

### 3) Calculation of Clock Frequency

The timing interruption of a timer 0 brings extra load of 10%-20% to the MCU, thus the extra load caused by the kernel should be reduced as possible on the premise of ensuring the actual demand, and the higher its frequency is, the greater the system overhead is, thus the frequency of the system is 50 Hz (the commonly-used frequency range in the  $\mu$ C/OS-II is 0-100 Hz).

In the TmpsYS, the C8051F020 adopts an external crystal oscillator (25 MHz) as a clock source. According to the initial

value of the timer, the calculating formula is as follows:

$$(2^{16} - X) \times F = \frac{F_{osc}}{12} \quad (1)$$

Where  $F$  represents clock frequency TICK,  $F_{osc}$  represents crystal frequency, and  $X$  represents the initial value of a counter. The equation  $F = 50$  Hz is substituted into the formula to obtain  $X = 5D3D_H$ , that is,  $TH0 = 5D_H$ , and  $TL0 = 3D_H$ .

## C. Design of Application Program

### 1) Analysis of Application Program

The application program is developed on a microcontroller successfully transplanted with a real-time kernel, the system service provided by the kernel can be invoked conveniently for programming, and the real-time property, stability and reliability are all greatly enhanced.

The system can realize three basic functions to reduce power consumption: single-machine multi-point temperature measuring, single-machine multi-point temperature monitoring and online multi-point temperature monitoring, and the task created in these modes is different for reducing power consumption and increasing performance of the system. In the single-machine multi-point temperature measuring mode, the system is only used as a temperature measuring instrument, and data acquisition and task processing are only required; In the single-machine multi-point temperature monitoring mode, it must have warning function under the premise of temperature measurement, and an exception processing task is required for recording the time of occurrence of temperature anomaly; In the online multi-point temperature monitoring mode, it must be communicated with a computer, a serial communication task is required [11], the system is just used as a terminal machine at the moment, a user monitors the computer, and data processing on the terminal machine is not required [12]. Particularly, as the keyboard is an important channel for interaction between a user and the system, it can work in any working mode.

### 2) Task Design

Task design is mainly used for partitioning tasks, allocating the task priority and determining a communication mechanism between tasks. The sensor cannot work normally before receiving the command, a task TMPStart must be created for periodically sending a temperature acquisition command to the sensor array by using a timing function OSTimeDlyHMSM() of the system, and the frequency of sending commands must be set within the scope of working frequency of the sensor. A binary semaphore SemTMPRead is used for synchronizing data reading tasks TMPRead. The periodicity of the task TMPStart cannot be destroyed according to the requirement of real-time property, thus the priority of the task TMPStart is set highest to ensure the integrity of data acquisition.

The TMPRead stores the read data in a buffer area TMPQueue, the space of the buffer area is dynamically allocated via system service, and the data is processed through a follow-up task in a first-in first-out queuing way.

The data processing task TMPPProcess can run only when there is data in the buffer area TMPQueue, and it's used for displaying the formatted temperature data through an LCD,

judging the excessive temperature point( out of the set threshold of temperature), and starting the exception processing task TMPExpt through a mailbox MboxExpt. A straight selection sorting algorithm is used for searching the excessive temperature point during the process of judging the excessive monitoring point.

In the straight selection sorting process, the selection and exchange of  $n-1$  times are carried out, the comparison of  $n-i$  times is required in every time of selection, wherein  $1 \leq i \leq n-1$ , and the number of movements is at most three in exchange per time, then the total number of comparisons:

$$C = \sum_{i=1}^{n-1} (n-i) = \frac{1}{2}(n^2 - n) \quad (2)$$

Because of the number of movements is at most three in exchange per time, then the maximum number of movements is  $3(n-1)$ .

The time complexity of straight selection sorting is  $O(n^2)$ , the straight selection sorting speed is higher than the straight insertion sorting speed, and the storage space is less used, thus the straight selection sorting algorithm is suitable for a system with small data storage space.

The monitoring point exception processing task TMPExpt controls the specific hardware to give an alarm response, and searches and records the time of occurrence of anomaly, and its priority should be higher than that of the data processing task. To avoid the loss of input information, a queue buffer area KeyQueue is used to store the keyboard scan code, the keyboard interrupt service program generates a scan code and writes it into the KeyQueue. If there is data in the buffer area, the keyboard task KeyTask executes the related operation, and is triggered by an external event, and its priority is set lowest.

From the analysis above, six tasks and the corresponding priorities (the highest priority is 2) can be obtained, as shown in Table I, and the operating mechanism of the whole software system is shown in Fig. 4.

#### D. Search of 1-wire Bus Device

The purpose of search is to obtain values (as shown in Table II) stored in an ROM in each device, because the MCU controls the corresponding devices by using the serial number.

##### 1) Search Algorithm

The search algorithm adopts a binary tree structure, and the search process is carried out along each partial node until the leaf nodes of an ROM code of the device are found [13]. The

TABLE I  
TASK PRIORITIZATION

Task <sup>a</sup>	TStart	TRead	TExpt	Process	TSend	KeyTask
Priority	2	3	4	5	6	7

<sup>a</sup> TStart = TMPStart , Tread = TMPRead , TExpt = TMPExpt , Process = TMPProcess , TSend = TMPSend .

TABLE II  
64-BIT REGISTRATION CODE IN THE ROM IN THE 1-WIRE BUS DEVICE

MSB		64-bit registration code in the ROM				LSB	
8-bit CRC check code		48-bit serial number				8-bit family code	
MSB	LSB	MSB	LSB	MSB	LSB	MSB	LSB

subsequent search is carried out along other paths on the node,

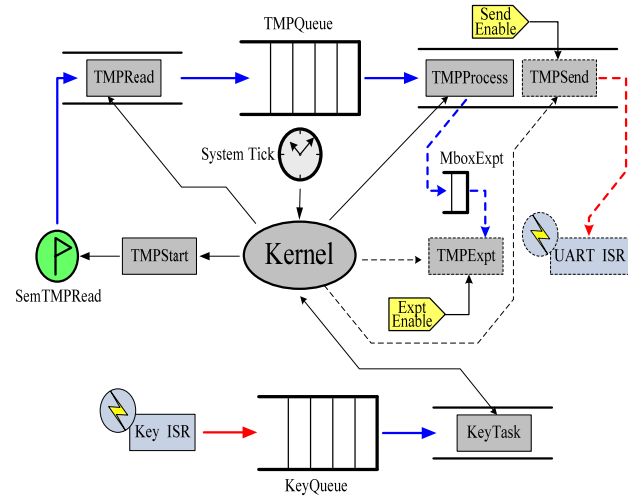


Fig. 4. Operating mechanism of the TMPSYS.

until the registration codes of all the devices on the bus are found in the same way.

##### 2) Search Process

After the bus reset, the host sends a search command for starting the actual search process. First, all the sensors on the bus send the first bit (least significant bit) in the ROM code at the same time. In the 1-wire communication, no matter the host reads data or data is written into the slave device, the 1-wire host starts the operation of each bit. According to the characteristics of 1-Wire, when all the slave devices respond the host at the same time, the outcome is equivalent to the logic that all data bits are sent; after the slave sends the first bit in the ROM code, the host starts the next operation, and then the slave sends a complementary code of data of the first bit in its ROM code; a judgment shown in Table III can be made to the first bit in the ROM code according to the data bit read twice.

##### E. Monitoring Program on PC side

The monitoring program (as shown in Fig. 5) of a PC machine realizes the serial communication between a terminal machine for the TMPSYS and the PC machine, performs analysis processing to the data acquired from 12 sensors, and finally, displays the temperature data at the monitoring point on a program interface. And when a monitoring point is out of the set threshold of temperature, the monitoring program also gives an alarm signal; a control panel of an operational program can achieve the purposes of adding the monitoring point and

TABLE III  
RETRIEVAL INFORMATION BIT

Bit (actual value)	Bit (complementary code)	Conclusions
0	0	The current bits in the ROM code of a slave include 0 and 1; differences exist
0	1	All the current bits in the ROM code of the slave are 0.
1	0	All the current bits in the ROM code of the slave are 1.
1	1	There is no response of a slave device on the bus.

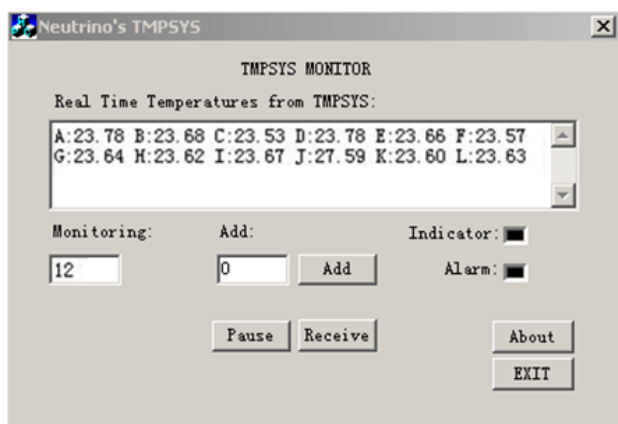


Fig. 5. Interface of the monitoring program on the PC side.

controlling a servo system for the terminal machine. An MSComm control is the core of the monitoring program.

#### F. Real-time test

The selected test environment is Keil uVision (v3.53), a logic analyzer carried in a Keil is used for timing test, the selected operating frequency of the C8051F020 is 25 MHz [14], and the selected switching frequency of the  $\mu\text{C}/\text{OS-II}$  (v2.00) is 50 Hz. The time difference is calculated from a tab file exported from the logic analyzer, that is, the response time is obtained. Refer to Table IV for the calculated evaluated data.

#### IV. CONCLUSIONS

Based on the above test, the kernel  $\mu\text{C}/\text{OS-II}$  can effectively realize multi-task scheduling with the support of a CIP-51 framework, and can accomplish the system function and can give a response within a short period time which is mainly determined by both the selected switching frequency of the  $\mu\text{C}/\text{OS-II}$  such as 50 Hz and the performance of CPU. Compared with the traditional back-fore ground system, the hard real-time kernel can enable the C8051F series single-chip microcomputer to realize more complex functions, and the subsequent upgrading of the application program does not affect the real-time property of the system. The sensor is simple and reliable in physical connection, convenient for expansion and maintenance of a bus, and particularly suitable for monitoring multipoint temperature; the keyboard and LCD are used as the man-machine interface, thus the core control chip with a JTAG interface provides a great convenience for detection and maintenance of the hardware system.

TABLE IV  
SYSTEM RESPONSE TEST OF THE TMPSYS

Test items <sup>b</sup>	Switch tasks	Ip	Sas	Smm	Smq	Mpa	Mpl
Response time (us)	79	3	216	170	167	33	29

<sup>b</sup> Ip = Interruption preempt , Sas = Signal amount synchronization , Smm = Sending short messages through mailbox , Smq = Sending messages in queue , Mpa = Memory pool allocation , Mpl = Memory pool deal location.

#### REFERENCES

- [1] LU Sheng-jie, HUO Shu-yan. Single Bus Multi-point Temperature Detection Technology Based on DS1820[J]. Modern Electronics Technique,34(2):185-187, 2011.
- [2] LI Gang, ZHAO Yan-feng. Principle and Application of 1-Wire Bus Digital Thermometer DS18B20[J]. Modern Electronics Technique,28(21):77-79,2005.
- [3] ZHANG Yi-hui. Research on Synchronous Switching System of Air Preheated Based on C8051F [D]. Master Degree Candidate, Xi'an University of Technology, 2006.
- [4] BI Jian-feng. The Research and Development of Intelligent Flowmeter Based C8051F060 [D]. Master Degree Candidate, Hebei University of Technology, 2007.
- [5] JU Rong, GUO Yi-qian. The application of DS18B20 in thermometric system [J]. Journal of Agricultural Mechanization Research,(1):224-226,2005
- [6] Maxim Integrated Products.DS18B20 Programmable Resolution 1-Wire® Digital Thermometer. [EB/OL] . <http://www.maxim-ic.com>, 2013.
- [7] ZHAO Jian-hua, WANG Wen-yong. Porting uC/OS-II kernel to 80C 51-family microprocessor [D]. Master Degree Candidate University of Electronic Science and technology, 2007.
- [8] TANG Song-song. The Research of Integrated Development Environment Based on  $\mu\text{C}/\text{OS-II}$  for Intelligent Instrument Microprocessor [D]. Master Degree Candidate, Chongqing University, 2006.
- [9] XU Jing-feng. Methods on Transplantation of  $\mu\text{C}/\text{OS-II}$ [J]. Computer Knowledge and Technology,4(29):493-494,2008.
- [10] ZHAO Yue-qi, MA Rui-qing, LIANG Gui-yi, et al. Design and Realization of Intelligent Temperature Control System Based on C8051F Microcontrollers [J]. Computer Measurement & Control, 17(3):490-491,2009.
- [11] Maxim Integrated Products.  $\pm 15\text{kV}$  ESD-Protected,  $1\mu\text{A}$ ,  $3.0\text{V}$  to  $5.5\text{V}$ ,  $250\text{kbps}$ , RS-232 Transceivers with Auto Shutdown [EB/OL]. <http://www.maxim-ic.com>, 2013.
- [12] HUA Xian-zhe. Room temperature and humidity monitoring and energy-saving system [C].The 6th International Conference on Computer Science & Education. pages 537-540, 2011.
- [13] Maxim.1-Wire Search Algorithm [EB/OL]. <http://www.maxim-ic.com/app-notes/index.mvp/id/187>, 2013.
- [14] LING Xu, ZHEN Chen, ZHANG Shi-lei et al. Research of serial communication system based on C8051F020 single chip[C]. 2010 International Conference on Computer Application and System Modeling. vol. 8 .2010 :V8-404-V8-407.

# Impact of Sectorization/Vehicular Traffic on Minimum Cell Size for Information Capacity Increase in Cellular Systems

Kwashie A. Anang, Predrag B. Rapajic, and Ruiheng Wu

**Abstract**—In this paper results of mathematical analysis supported by simulation are used to study the impact of sectorization/vehicular traffic on the theoretical limit for cell size radius reduction in cellular wireless communication systems. Information capacity approach is used for the analysis. Attention is given to the active co-channel interfering cells. Because at carrier frequencies greater than 2 GHz, co-channel interfering cells beyond the first tier becomes dominant as the cell size radius reduces. Results show that for sectorized cellular wireless communication system operating at carrier frequency greater than 2 GHz and having smaller cell size radius in a traffic environment the second tier co-channel interference still becomes active. This causes a decrease in the information capacity of the cellular wireless system. For example for a heavy vehicular traffic environment, at a carrier frequency  $f_c = 15.75$  GHz, basic path loss exponent  $\alpha = 2$  and cell radius  $R = 100, 300$  and  $500$  m for a six sector cellular the decrease in information capacity, because of interference from the second tier was 5.47, 3.36 and 2.78%.

**Index Terms**—Breakpoint distance, land mobile radio cellular system, radio propagation, spectrum efficiency, sectorization.

*Original Research Paper*  
DOI: 10.7251/ELS1317021A

## I. INTRODUCTION

THE radio frequency spectrum is an important parameter in the design and implementation of a wireless communication system. Because it is limited and regulated by international agreements [1], [2]. Cellular wireless systems are therefore partly used to achieve spectral efficiency and have been in operation since the late 1970's.

A high overall spectral efficiency is achieved at the frequency planning level by reducing the cell size radius [3]. Reducing cell size radius has caused cell sites to be installed in

ever increasing densities [4]. However, Zhou et al. reported that there may be a limit to cell size radius reduction [5], because of an increase in co-channel interference. Since co-channel interference is one of the ultimate factors which determines the bit error rates (BERs) available to a user.

The rapid development of high-speed data rate wireless communication system by service providers and the need for high-bit-rate services at mobile terminals have spurred the use of broadband channels in wireless communication systems. Thus the UHF bands (900 and 1900 MHz) normally used for cellular wireless communication are not suitable for wireless broadband application. For broadband channels carrier frequency needs to be increased [6]. Therefore, future and emerging cellular wireless communication systems beyond the third generation (B3G) will be accommodated at carrier frequencies greater than 2 GHz [6]–[8].

Increasing carrier frequency leads to an increase in free space path loss and diffraction loss. An increase in the path loss means cell size radius needs to be reduced to smaller radius. For smaller cell size radius cellular system co-channel interference becomes severe and more difficult to control [6].

Numerous studies on cellular wireless communication systems have given ranges of maximum and minimum cell size radius for information capacity increase [5], [9]–[11]. Most of these studies to proceed analytically took into account co-channel interference from the first tier, assuming interference outside the first tier to be negligible. Because of the assumption of large path loss exponent [5].

Results from a study by Anang et al. shows that at higher microwave carrier frequencies greater than 2 GHz co-channel interference outside the first tier, (second tier) becomes active and it was reported that there is a theoretical limit to cell size radius reduction [12]. However, the study was for a non-sectorized cellular wireless system. A study on the impact of vehicular traffic on the information capacity of a non-sectorized cellular wireless system, operating at carrier frequencies greater than 3 GHz was presented in [13]. The impact of cell sectorization on the information capacity of cellular wireless networks was presented in [14], without the inclusion of the effect of vehicular traffic. However, at higher carrier frequencies and smaller cell size radius; vehicles, pedestrians and other objects on the road affect the

Manuscript received 10 April 2013. Accepted for publication 7 May 2013.

This is an expanded version of work presented at the IX International Symposium Industrial Electronics INDEL 2012, Banja Luka, Bosnia and Herzegovina, November 2012 and at the 5th IEEE European Symposium on Computer Modeling and Simulation EMS 2011, Madrid, Spain, November 2011.

K. A. Anang, P. B. Rapajic and R. Wu are with the Wireless and Mobile Communication Research Centre, School of Engineering, University of Greenwich, Chatham Maritime, ME4 4TB, UK, Fax : +44-(0)-1634-883153. The corresponding author, K. A. Anang can be reached on Tel: +44-(0)-1634-883873, and E-mail: k.anang@gre.ac.uk.

information capacity performance of cellular wireless systems [7]. Therefore, the main contribution of this paper is as follows:

- We study the impact of cell sectorization on the information capacity performance of future and emerging cellular wireless systems, which will be operating at higher microwave carrier frequency greater than 2 GHz and smaller cell size radius, where first and second tier co-channel interference are dominant.
- We study the impact of cell sectorization/vehicular traffic on the information capacity of future and emerging cellular wireless systems, which will be operating at higher microwave carrier frequency greater than 2 GHz and smaller cell size radius, where first and second tier co-channel interference are active.

The rest of the paper is organised as follows. Section II describes the system models for propagation, sectorized co-channel interference, user distribution and outlines the basic assumptions used in the modeling. Section III focus on the spectral efficiency of the cellular wireless system used for our information capacity analysis. Section IV presents theoretical analysis and simulation results for the impact of cell sectorization/vehicular traffic on the information capacity. Finally, we conclude this paper in Section V.

## II. PROPAGATION AND SYSTEM MODELS

A two-dimensional hexagonal smaller cell size radius network is assumed, where the BSs are uniformly distributed. Cells form clusters (co-channel cell) around reference cells. BSs located at the center of each cell receive signals from all users in the system which is attenuated according to the power-law path loss.

### A. Users' Distribution

The cell shape is approximated by a circle of radius  $R$ , for mathematical convenience. It is assumed that all mobiles, (desired and interfering users) are uniformly and independent distributed in their cells. Mobile stations (Ms) are also assumed to be located in the far field region. The probability distribution function (PDF) of a MS location relative to a BS in polar co-ordinate is given by

$$\rho_{r,\theta}(r, \theta) = \frac{(r - R_0)}{\pi(R - R_0)^2}; R_0 \leq r \leq R, 0 \leq \theta \leq 2\pi, \quad (1)$$

where  $R_0$  corresponds to the minimum distance a mobile can be from the BS antenna (to be in the far field region), which defines a small circular area around the MS to be kept free from interferes. A reasonable value around 20 m is recommended for smaller cell size radius systems.

### B. Propagation Path Loss

The radio environment of a cellular system is described by: (1) path loss, (2) shadowing and (3) multipath fading. For the purposes of this study, we make the simplifying assumption that shadowing and multipath fading is negligible. That is leaving only the variation of averaged received power with distance. The analysis and simulation uses the two-slope path

loss model [10], to obtain the average received power as function of distance. From this model the average received signal power  $P_r$  [W] is given by:

$$P_r = \frac{K}{r^\alpha (1 + r/g)^\rho} P_t, \quad (2)$$

where  $K$  is the constant path loss factor, and it is the free space path loss at a reference distance  $r_0 = 1$  m,  $r$  [m] is the distance between BS and MS.  $\alpha$  is the basic path loss exponent (roughly 2),  $\rho$  is the additional path loss exponent (between 2-8).  $P_t$  [W] is the transmitted signal power. The breakpoint distance,  $g = 4 h_b h_m / \lambda_c$ , where  $\lambda_c$  is the carrier wavelength. BS antenna height  $h_b = 15$  m, and MS antenna height  $h_m = 1.5$  m. In this work the exact value of  $K$  and  $P_t$  is not required for the analysis. Therefore we assume  $K = 1$ ,  $P_t = 1$  and focus on the attenuation factor

$$P_t = r^{-\alpha} (1 + r/g)^{-\rho}. \quad (3)$$

### C. Sectorized Two Tier Co-Channel Interference

The first and second tiers of co-channel interference are considered for interference generation. The desired mobile is located in the central cell and the interfering mobiles are in cells in the first and second tiers as shown in Fig. 1. To simplify the analysis the following assumptions have been made in the co-channel interference model. First the system is considered to be interference-limited, with thermal noise power negligible relative to the co-channel interference power [15]. Therefore, the ratio of carrier to noise CNR reduces to the carrier-to-interference power ratio CIR. All inter-channel interference is considered to be negligible [15]. All BSs are assumed to transmit the same power, and for simplicity we assume each cell to be circular shape.

From [12], for an omnidirectional antenna cell site layout pattern the number of co-channel interfering cells in a given tier  $N_n$  is given by

$$N_n = N_l \times n; (n = 1, 2, 3, 4, \dots), \quad (4)$$

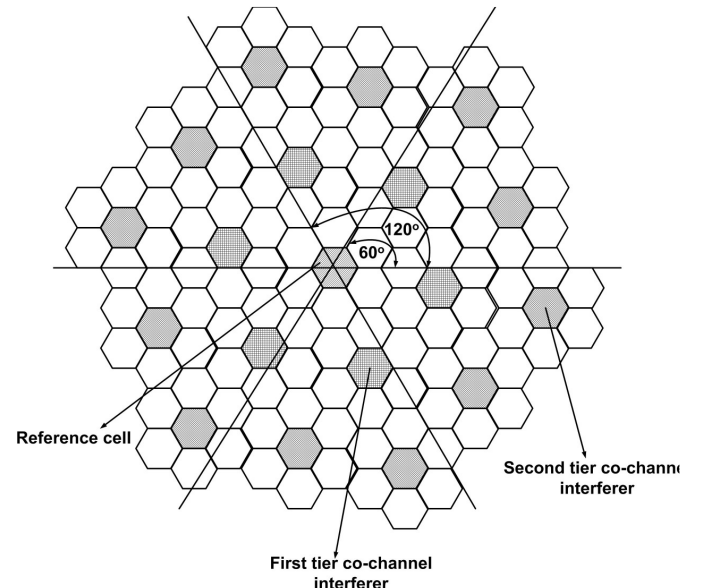


Fig. 1. Omnidirectional, sectorized cellular wireless communication systems showing first and second tier co-channel interferers.

where  $N_l$  is the number of interfering cells in the first tier and  $n$  is the  $n$ th tier number and it is always an integer. Now for sectorized cells (direction antennas), (4) is modified as follows:

$$N_n = \frac{N_l \times n}{S}; (n=1,2,3,4,\dots), \quad (5)$$

where  $S$  is the number of sectors in the cell. For omnidirectional cellular system,  $S = 1$ , for  $120^\circ$  and  $60^\circ$  sectorized cellular system  $S = 3$  and  $6$ .

Reference [16] stated that the uplink interference at a served BS is the non-coherent sum of interference signals from the user served by the BS and the users served by other BSs. Likewise the desired user CIR,  $\gamma$ , is defined as the ratio of averaged received signal power from a MS at a distance  $r$  [m] from the desired BS to the sum of interfering received signal power. Therefore, the desired user CIR,  $\gamma$ , can be written as follows:

$$\gamma = \frac{P_d}{P_I} = \frac{P_d(r)}{\sum_{i=1}^{N_{I1}/S} P_{i1}(r_{i1}) + \sum_{i=2}^{N_{I2}/S} P_{i2}(r_{i2})}, \quad (6)$$

where  $P_d$  [W], is the received power level of desired MS and  $P_I$  [W] is the power sum of individual interferers in tiers 1 and 2.  $N_{I1}$  and  $N_{I2}$  is the number of co-channel interfering cell in tiers 1 and 2 of an omnidirectional cellular system. For hexagonal cell site layout with cluster size  $N_c = 7$ ,  $N_{I1} = 6$  and  $N_{I2} = 12$ .  $P_{i1}$  and  $P_{i2}$  [W] is the average power level received from the  $i$ th interfering MSs at distances  $r_{i1}$  and  $r_{i2}$  [m] from the desired BS.

### III. AREA SPECTRAL EFFICIENCY

The ultimate capacity of a land mobile radio system is directly related to its spectral efficiency [17]. The spectral efficiency of a cellular wireless system can be expressed in a number of ways such as number of channels per cell, Erlangs/km<sup>2</sup>, the number of users/km<sup>2</sup>, etc. However in this paper, we adopted the definition suggested by [18]. This definition gives a more complete picture of the spectrum efficiency by expressing it in terms of capacity, bandwidth, and area. The area spectral efficiency (ASE) is defined as the achievable sum rate [bits/sec] (of all users in a cell) per unit bandwidth per unit area which is given by [18] as:

$$A_e = \frac{\sum_{k=1}^{N_s} C_k}{\pi W (D/2)^2}, \quad (7)$$

where  $W$  is the total bandwidth allocated to each cell,  $D$  is the reuse distance,  $N_s$  is the total number of active serviced channels per cell. The achievable sum rate  $C_k$  is the Shannon capacity of the  $k$ th user, which depends on  $\gamma$ , the received carrier to interference power ratio CIR of that user and  $W_k$  the bandwidth allocated to the user. The Shannon capacity formula assumes the interference has Gaussian characteristics. Because both the interference and signal power of the  $k$ th user vary with mobiles locations and propagation conditions,  $\gamma$  varies with time, therefore the average channel capacity of the  $k$ th user is given by [18] as

$$\langle C_k \rangle = W_k \int_0^{+\infty} \log_2(1+\gamma) p_\gamma(\gamma) d\gamma, \quad (8)$$

where  $p_\gamma(\gamma)$ , is the probability distribution function (PDF) of the average mean CIR( $\gamma$ ) of the  $k$ th user.

The transmission rate is assumed to be continuously adapted relative to the CIR in such a manner that the BER goes to zero asymptotically. In (8) assuming that all users are assigned the same bandwidth,  $\langle C_k \rangle = \langle C \rangle$  becomes the same for all users, therefore  $\langle A_e \rangle$  can be written as

$$\langle A_e \rangle = \frac{4N_s \langle C \rangle}{\pi W D^2} = \frac{4N_s \langle C \rangle}{\pi W R_u^2 R^2}, \quad (9)$$

where  $R_u$  is defined as the normalized reuse distance and is given by the ratio of reuse distance and cell radius ( $D/R$ ). For a TDMA system, the total bandwidth is allocated to only one active user per time slot, (that is  $N = 1$ ,  $W_k = W$ ). Substituting this into (9) yields

$$\langle A_e \rangle = \frac{4}{\pi R_u^2 R^2} \int_0^{+\infty} \log_2(1+\gamma) p_\gamma(\gamma) d\gamma. \quad (10)$$

### IV. SECTORIZED IMPACT ANALYSIS

In this section, we analyse the impact of sectorization on the information capacity performance of smaller cell size radius cellular system operating at carrier frequency greater than 2 GHz, in the presence of first and second tier co-channel interference. The analysis applies to a TDMA, (time-division multiple access) based cellular wireless system. Because, it is the most representative of cellular wireless system. The analysis is based on fully loaded systems with fixed cluster size  $N_c = 7$ . Though there is an excessive demand to broadcast, (downlink) high speed data in emerging communication services, because of space we confine our study on the uplink between a MS-to-BS.

#### A. Analysis

Recall from section II-A; user are randomly located in their respective BSs, therefore  $\gamma$  is a random variable which depends on the random position of the user and the sums of interference from tier 1 and 2. Without power control the average-case interference configuration corresponds to the case, where all the  $N_{I1}$  and  $N_{I2}$  co-channel interferers are at the center of their respective BSs, at a distances  $r_{i1} = D$  [m] and  $r_{i2} = 2D$  [m]

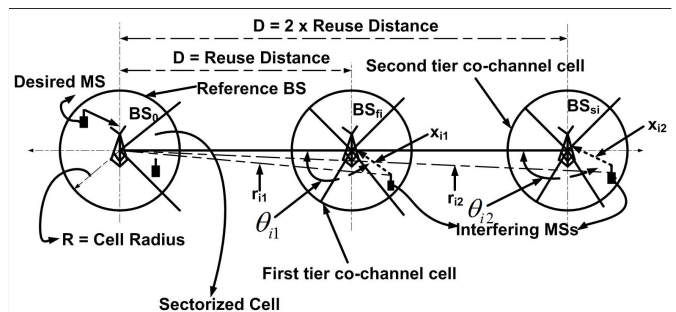


Fig. 2. Sectorized cellular system geometry of the desired and interfering mobile in two co-channel cells.

from the desired MS's as shown in Fig. 2. Note power control is essential for direct sequence CDMA systems; therefore we did not consider it in our analysis. Assuming that the transmitted power of all users is the same and substituting (3) into (6) yields

$$\begin{aligned} \gamma(r, N_{I1}, N_{I2}) &= \frac{P_d(r)}{\sum_{i1=1}^{N_{I1}/S} P_{i1}(r_{i1}) + \sum_{i2=1}^{N_{I2}/S} P_{i2}(r_{i2})} \\ &= \frac{r^{-\alpha} (1+r/g)^{-\rho}}{\sum_{i1=1}^{N_{I1}/S} \tau^{-\alpha} (1+\tau/g)^{-\rho} + \sum_{i2=1}^{N_{I2}/S} (2\tau)^{-\alpha} (1+(2\tau)/g)^{-\rho}} \quad (11) \\ &= \left(\frac{2\tau}{r}\right)^{\alpha} \cdot \left(\frac{g}{g+r}\right)^{\rho} \cdot \left( \frac{SN_{I2}}{2^{\alpha} N_{I1} N_{I2} \left(\frac{g}{g+\tau}\right)^{\rho} + \left(\frac{g}{g+2\tau}\right)^{\rho}} \right) \end{aligned}$$

where  $\tau$  is the product of  $R_u$  and  $R$ ,  $R_u$  is the normalized reuse distance and  $R$  is the cell size radius.  $S$  is the number of sectors in the cell. Because  $\gamma$  is a function of  $r$ , the desired user capacity is given by

$$\langle C(r, N_{I1}, N_{I2}) \rangle = W_0 \log_2(1 + \gamma(r, N_{I1}, N_{I2})). \quad (12)$$

Substituting (12) in (9) yields the ASE conditioned on the de-sired mobile position  $r$ , for a fully-loaded system. Integrating (12) over the desired user's position PDF (1) yields the average ASE for the average interference configuration as:

$$\langle A_e(r, N_{I1}, N_{I2}) \rangle = \frac{4}{\pi R_u^2 R^2} \int_{R_0}^R \log_2(1 + \gamma) \rho_r(r) dr. \quad (13)$$

It is clear from (13) that the average ASE mainly depends on the mean CIR, which is a function of random locations of the MS. This makes the ASE mathematically intractable to solve. A computer simulation is therefore used to solve it.

### B. Simulations

Monte Carlo simulation is used to estimate  $\langle A_e \rangle$ , because it appears to be mathematically intractable to explicitly solve analytically. Fig. 3 shows a simulation flowchart for the ASE of a sectorized cellular system, and the basic parameters used for the simulation are presented in Table I. In the simulation the desired user is randomly located, and uniformly distributed as described in subsection II-A of section II. When the desired

TABLE I  
SIMULATION PARAMETERS

Parameter	Value
Type of system	omni, 3-sector and 6-sector
Cell radius, $R$	100 to 1000 m
Effective road height, $h$	0.23 and 1.3 m [7], [19]
Path loss exponent, ( $\alpha$ ),	2
Additional path loss exponent, ( $\rho$ )	2
Cluster size, $N_C$	7
BS antenna height, $h_B$	15 m [19]
MS antenna height, $h_M$	1.5 m [20]
Mobile Distribution	Uniform/Random
Number of co-channel tiers	2
Co-channel interferences	Random and first and second tiers
Frequency reuse factor, $R_U$	4 [18]
Frequencies, $f_C$	0.9, 2, 3.35, 8.45 and 15.75 GHz

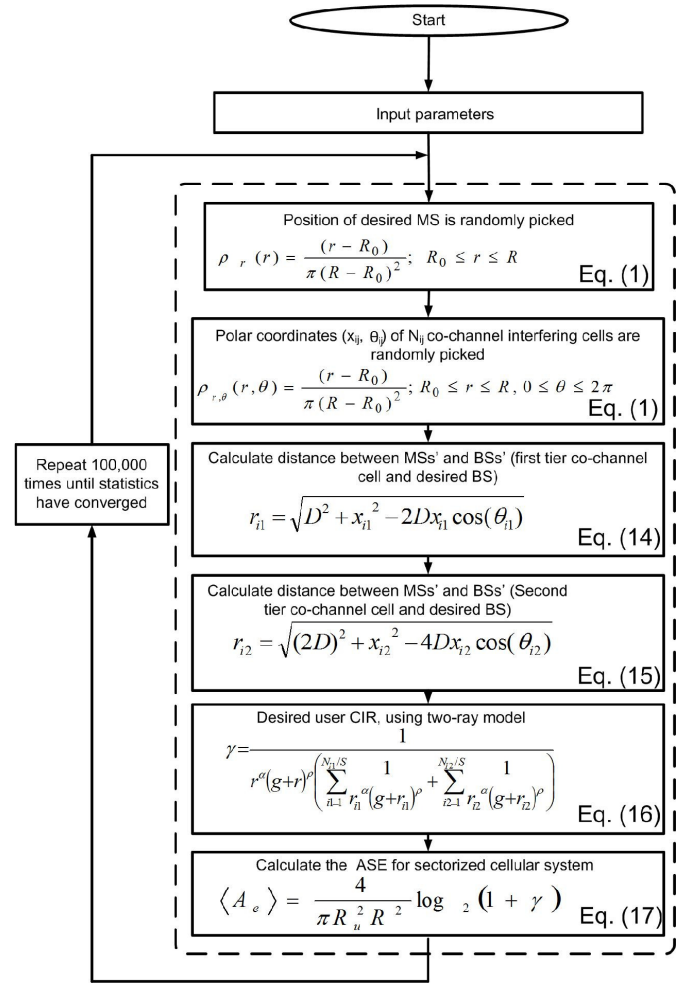


Fig. 3. Flowchart for sectorized cellular system area spectrum efficiency simulation.

user position is located the simulation algorithms is composed of the following steps:

- 1) The polar coordinates  $(x_{i1}, \theta_{i1})$  and  $(x_{i2}, \theta_{i2})$  of the  $N_{I1}$  and  $N_{I2}$  co-channel interferers are randomly picked according to (1).
- 2) From Fig. 2, (geometry for analysis) the distance  $r_{i1}$  for each co-channel interferer from tier 1 to the desired BS is calculated as

$$r_{i1} = \sqrt{D^2 + x_{i1}^2 - 2Dx_{i1} \cos(\theta_{i1})}. \quad (14)$$

- 3) The distance  $r_{i2}$  for each co-channel interferer from the second tier to the desired BS is calculated as

$$r_{i2} = \sqrt{(2D)^2 + x_{i2}^2 - 4Dx_{i2} \cos(\theta_{i2})}. \quad (15)$$

- 4) The two-slope path loss model (2), is used to calculate the average received signal power of the desired user and interfering mobiles in the first and second tier of co-channel cells ( $P_d$ ,  $P_{i1}$ s and  $P_{i2}$ s), therefore the CIR is calculated as

$$\gamma = \frac{1}{r^{\alpha} (g+r)^{\rho} \left( \sum_{i1=1}^{N_{I1}/S} \frac{1}{r_{i1}^{\alpha} (g+r_{i1})^{\rho}} + \sum_{i2=1}^{N_{I2}/S} \frac{1}{r_{i2}^{\alpha} (g+r_{i2})^{\rho}} \right)}. \quad (16)$$

- 5) The ASE,  $A_e$  is calculated as

$$\langle A_e \rangle = \frac{4}{\pi R_u^2 R^2} \log_2(1 + \gamma). \quad (17)$$

Repeating the proceed above (from steps 1-5) 100000 after locating the desired user position.  $\langle A_e \rangle$ , is estimated by taking the average of all the observations of  $A_e$  as given by (17).

### C. Numerical and Simulations Results

Figs. 4, 5 and 6 show plot of ASE as a function of cell size radius for omni-directional, three sectors and six sector cellular systems. The figures quantified the fact that sectorization reduces co-channel interference, thus improves CIR, which causes an increase in information capacity of the cellular wireless systems.

The curves in Fig. 4 show the plot for an omni-directional cellular system for different carrier frequency  $f_c$ , using the interference model presented in [18], and the model presented in this work (11). The curves show that when  $f_c = 900$  MHz and  $R = 0.1$  km, the decrease in information capacity was 6%. Now for  $f_c = 2, 3.35, 8.45$  and  $15.75$  GHz, the decrease in information capacity was 8.55, 10.5, 13.73, and 15.31%. At  $R = 0.3$  km for  $f_c = 0.9, 2, 3.35, 8.45$  and  $15.75$  GHz, the decrease in information capacity was 3.7, 4.9, 6.15, 9.18, and 11.39%. In the case of  $R = 0.5$  km for  $f_c = 0.9, 2, 3.35, 8.45$  and  $15.75$  GHz, the decrease in information capacity was 3.17, 4.0, 4.88, 7.42 and 9.42%.

The curves in Fig. 5 show the case of a three sector cellular wireless communication system. The curves show that for  $f_c = 0.9, 2, 3.35, 8.45$  and  $15.75$  GHz at cell radius  $R = 0.1$  km,

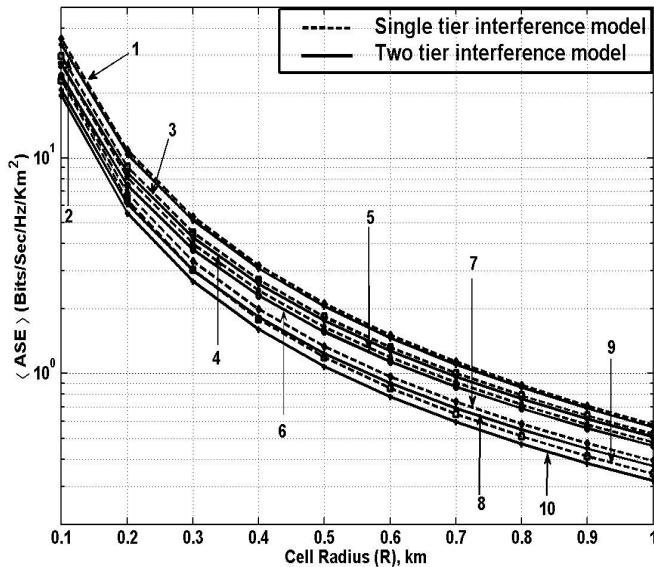


Fig. 4. Average uplink Area Spectral Efficiency (ASE) versus cell radius for omnidirectional cellular system at different carrier frequencies  $f_c$ . (Fully-loaded system with 6 and 12 co-channel interfering cells in first and second tier  $N_{I1} = 6$  and  $N_{I2} = 12$ ; basic and extra path loss exponent:  $\alpha = 2$  and  $\rho = 2$ ; MS and BS antenna heights:  $h_m = 1.5$  m and  $h_b = 15$  m). 1 - single tier interfering model ( $f_c = 900$  MHz), 2 - two tier interfering model ( $f_c = 900$  MHz), 3 - single tier interfering model ( $f_c = 2$  GHz), 4 - two tier interfering model ( $f_c = 2$  GHz), 5 - single tier interfering model ( $f_c = 3.35$  GHz), 6 - two tier interfering model ( $f_c = 3.35$  GHz), 7 - single tier interfering model ( $f_c = 8.45$  GHz), 8 - two tier interfering model ( $f_c = 8.45$  GHz), 9 - single tier interfering model ( $f_c = 15.75$  GHz), 10 - two tier interfering model ( $f_c = 15.75$  GHz).

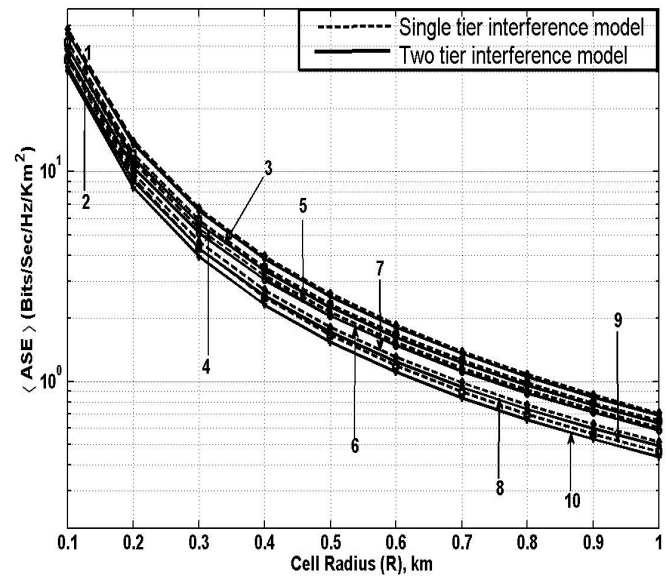


Fig. 5. Average uplink Area Spectral Efficiency (ASE) versus cell radius for three sector cellular system at different carrier frequencies  $f_c$ . (Fully-loaded system with 6 and 12 co-channel interfering cells in first and second tier  $N_{I1} = 6$  and  $N_{I2} = 12$ ; basic and extra path loss exponent:  $\alpha = 2$  and  $\rho = 2$ ; MS and BS antenna heights:  $h_m = 1.5$  m and  $h_b = 15$  m). 1 - single tier interfering model ( $f_c = 900$  MHz), 2 - two tier interfering model ( $f_c = 900$  MHz), 3 - single tier interfering model ( $f_c = 2$  GHz), 4 - two tier interfering model ( $f_c = 2$  GHz), 5 - single tier interfering model ( $f_c = 3.35$  GHz), 6 - two tier interfering model ( $f_c = 3.35$  GHz), 7 - single tier interfering model ( $f_c = 8.45$  GHz), 8 - two tier interfering model ( $f_c = 8.45$  GHz), 9 - single tier interfering model ( $f_c = 15.75$  GHz), 10 - two tier interfering model ( $f_c = 15.75$  GHz).

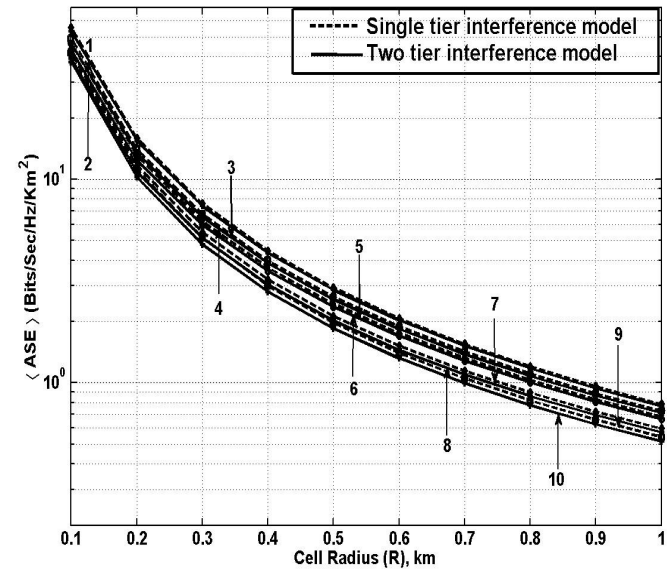


Fig. 6. Average uplink Area Spectral Efficiency (ASE) versus cell radius for six sector cellular system at different carrier frequencies  $f_c$ . (Fully-loaded system with 6 and 12 co-channel interfering cells in first and second tier  $N_{I1} = 6$  and  $N_{I2} = 12$ ; basic and extra path loss exponent:  $\alpha = 2$  and  $\rho = 2$ ; MS and BS antenna heights:  $h_m = 1.5$  m and  $h_b = 15$  m). 1 - single tier interfering model ( $f_c = 900$  MHz), 2 - two tier interfering model ( $f_c = 900$  MHz), 3 - single tier interfering model ( $f_c = 2$  GHz), 4 - two tier interfering model ( $f_c = 2$  GHz), 5 - single tier interfering model ( $f_c = 3.35$  GHz), 6 - two tier interfering model ( $f_c = 3.35$  GHz), 7 - single tier interfering model ( $f_c = 8.45$  GHz), 8 - two tier interfering model ( $f_c = 8.45$  GHz), 9 - single tier interfering model ( $f_c = 15.75$  GHz), 10 - two tier interfering model ( $f_c = 15.75$  GHz).

the decrease in the information capacity between the two interference model was 4.62, 6.51, 7.94, 10.36 and 11.56%. For 0.3 km at carrier frequencies  $f_c = 0.9, 2, 3.35, 8.45$  and 15.75 GHz, the decrease in ASE was 3, 3.9, 4.81, 7.09 and 8.72%. For 0.5 m, the decrease was 2.61, 3.22, 3.85, 5.62 and 7.28%. We can therefore conclude that for a three sector cellular wireless communication system as the carrier frequency increases and cell size radius reduces, second tier co-channel interference becomes severe.

The curves in Fig. 6 show the case of a six sector cellular wireless communication system. The curves show that for  $f_c = 0.9, 2, 3.35, 8.45$  and 15.75 GHz, at cell radius  $R = 0.1$  km, the decrease in the information capacity between the two interference model was 4.02, 5.57, 6.77, 8.8 and 10%. For 0.3 km at carrier frequencies  $f_c = 0.9, 2, 3.35, 8.45$  and 15.75 GHz, the decrease in ASE was 2.64, 3.4, 4.17, 6.05 and 7.43%. For 0.5 m, the decrease was 2.32, 2.83, 3.35, 4.89 and 6.24%. We can conclude that for a sectorized cellular wireless communication system as the carrier frequency increases and cell size radius reduces, second tier co-channel interference becomes dominant. Tables II, III and IV show the results of percentage decrease in ASE between the two interference models; for different cellular network sectorization; carrier frequency  $f_c$  and cell size radii R: 0.1, 0.3 and 0.5 km.

#### D. Combined Effect of Sectorization and Vehicular Traffic

In this section, we consider the ASE of a fully loaded sectorized cellular system in a light/heavy vehicular traffic environment, by including effective road height in the two-slope path loss model. This is the scenario for an urban line-of-sight (LOS) environment, when carrier frequencies are greater than 2 GHz.

1) *Analyses-Modified Breakpoint Distance*: The modified breakpoint distance proposed by Masui et al. [7], is incorporated into the system model, (that is the path loss model), for the study of impact of vehicular traffic on the information capacity performance of a sectorized cellular wireless system. The modified breakpoint distance  $g_m$  is given by [7], as

TABLE III  
DECREASE IN ASE BETWEEN THE TWO INTERFERENCE MODEL:  
THREE-SECTOR CELLULAR SYSTEM  
 $h_m = 1.5$  m,  $h_b = 15$  m and  $\alpha = 2$

Cell Radius (km)	Carrier Frequency	Decrease in ASE (%)
0.1	900 MHz	4.62
	2 GHz	6.51
	3.35 GHz	7.94
	8.45 GHz	10.36
	15.75 GHz	11.56
0.3	900 MHz	3
	2 GHz	3.9
	3.35 GHz	4.81
	8.45 GHz	7.09
	15.75 GHz	8.27
0.5	900 MHz	2.61
	2 GHz	3.22
	3.35 GHz	3.85
	8.45 GHz	5.62
	15.75 GHz	7.28

TABLE IV  
DECREASE IN ASE BETWEEN THE TWO INTERFERENCE MODEL: SIX-SECTOR  
CELLULAR SYSTEM  
 $h_m = 1.5$  m,  $h_b = 15$  m and  $\alpha = 2$

Cell Radius (km)	Carrier Frequency	Decrease in ASE (%)
0.1	900 MHz	4.02
	2 GHz	5.57
	3.35 GHz	6.77
	8.45 GHz	8.80
	15.75 GHz	10
0.3	900 MHz	2.64
	2 GHz	3.4
	3.35 GHz	4.17
	8.45 GHz	6.05
	15.75 GHz	7.43
0.5	900 MHz	2.32
	2 GHz	2.83
	3.35 GHz	3.35
	8.45 GHz	4.89
	15.75 GHz	6.24

$$g_m = \frac{4(h_b - h) \times (h_m - h)}{\lambda_c}, h < h_m, \quad (18)$$

where  $h$  is the effective road height, which is due to vehicles, pedestrians and other objects on the road. Now,  $h$  depends on the average height of traffic on the road, which is the average height of vehicles and pedestrians height on the road [7]. For light vehicular traffic the value of  $h$  is between 0.23 and 0.74 m, and for heavy vehicular traffic, it is between 1.29 and 1.64 m [19].

For the simulation of the combine effect of sectorization and vehicular traffic on the information capacity performance of the cellular wireless system, step 4) of the algorithm described in Section IV-B is changed as follows to incorporate the modified breakpoint.

$$\gamma = \frac{1}{r^\alpha (g+r)^\rho \left( \sum_{i1=1}^{N_{i1}/S} \frac{1}{r_{i1}^\alpha (g_m + r_{i1})^\rho} + \sum_{i2=1}^{N_{i2}/S} \frac{1}{r_{i2}^\alpha (g_m + r_{i2})^\rho} \right)} \quad (19)$$

#### E. Simulations Results – Sectorized/Vehicular Traffic

The combined effect of sectorization and vehicular traffic

TABLE II  
DECREASE IN ASE BETWEEN THE TWO INTERFERENCE MODEL:  
OMNIDIRECTIONAL CELLULAR SYSTEM  
 $h_m = 1.5$  m,  $h_b = 15$  m and  $\alpha = 2$

Cell Radius (km)	Carrier Frequency	Decrease in ASE (%)
0.1	900 MHz	6
	2 GHz	8.55
	3.35 GHz	10.5
	8.45 GHz	13.73
	15.75 GHz	15.3
0.3	900 MHz	3.7
	2 GHz	4.9
	3.35 GHz	6.15
	8.45 GHz	9.18
	15.75 GHz	11.39
0.5	900 MHz	3.17
	2 GHz	4.0
	3.35 GHz	4.88
	8.45 GHz	7.42
	15.75 GHz	9.42

on the ASE of a smaller cell size radius cellular system, operating at different carrier frequencies  $f_c$  is shown in Figs. 7-10. The results show that the ASE curves conserve the same relative shape as Figs. 5 and 6. Comparing the figures, it can be seen that both secotrized cellular systems operating in traffic environment have higher area spectrum efficiency than the secotrized cellular systems when there is no traffic.

The ASE of a three sector cellular system for light and heavy vehicular traffic is shown in Figs. 7 and 8. The curves show that for light vehicular traffic, and carrier frequencies  $f_c = 0.9, 2, 3.35, 8.45$  and  $15.75$  GHz, at cell size radius  $R = 0.1$  km, the decrease in the information capacity between the two interference models was 4.29, 6.02, 7.42, 9.94 and 11.26%. For 0.3 km, the decrease in the information capacity between the two interference models was 2.82, 3.63, 4.44, 6.56 and 8.22%, and for 0.5 km, it was 2.51, 3.00, 3.59, 5.19 and 6.82%.

From the three sector and heavy vehicular traffic result, the decrease in information capacity between the two interference models for carrier frequencies  $f_c = 0.9, 2, 3.35, 8.45$  and  $15.75$  GHz at cell size radius  $R = 0.1$  km, is 2.55, 2.97, 3.45, 4.91 and 6.40%. For 0.3 km, it is 2.15, 2.30, 2.49, 3.10 and 3.81%. For 0.5 km, the decrease was 1.91, 2.17, 2.27, 2.69 and 3.16%. These results are tabulated in Table V and VI.

The ASE of a six sector cellular system in a light and heavy vehicular traffic environment is shown in Figs. 9 and 10. The curves show that for light vehicular traffic, and carrier frequencies  $f_c = 0.9, 2, 3.35, 8.45$  and  $15.75$  GHz, at cell size

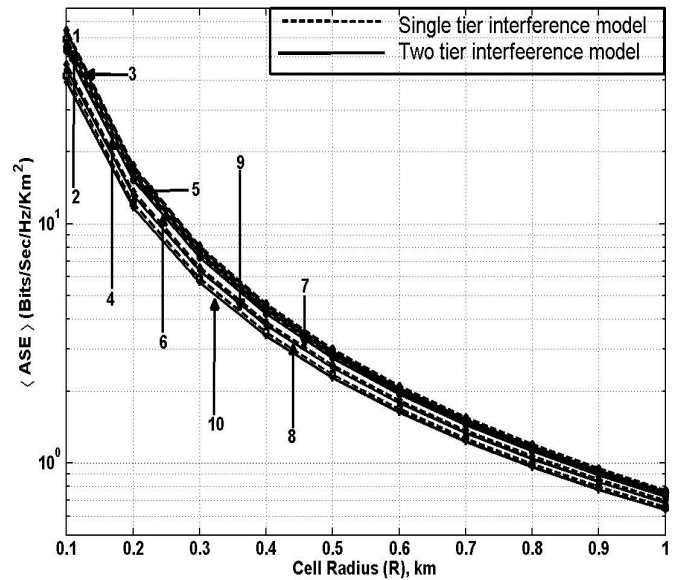


Fig. 8. Average uplink Area Spectral Efficiency (ASE) versus cell radius for three sector cellular system and heavy vehicular traffic at different carrier frequencies  $f_c$ . (Fully-loaded system with 6 and 12 co-channel interfering cells in first and second tier  $N_{I1} = 6$  and  $N_{I2} = 12$ ; basic and extra path loss exponent:  $\alpha = 2$  and  $\rho = 2$ ; MS and BS antenna heights:  $h_m = 1.5$  m and  $h_b = 15$  m; effective road height  $h = 1.3$  m).

1 - single tier interfering model ( $f_c = 900$  MHz), 2 - two tier interfering model ( $f_c = 900$  MHz), 3 - single tier interfering model ( $f_c = 2$  GHz), 4 - two tier interfering model ( $f_c = 2$  GHz), 5 - single tier interfering model ( $f_c = 3.35$  GHz), 6 - two tier interfering model ( $f_c = 3.35$  GHz), 7 - single tier interfering model ( $f_c = 8.45$  GHz), 8 - two tier interfering model ( $f_c = 8.45$  GHz), 9 - single tier interfering model ( $f_c = 15.75$  GHz), 10 - two tier interfering model ( $f_c = 15.75$  GHz).

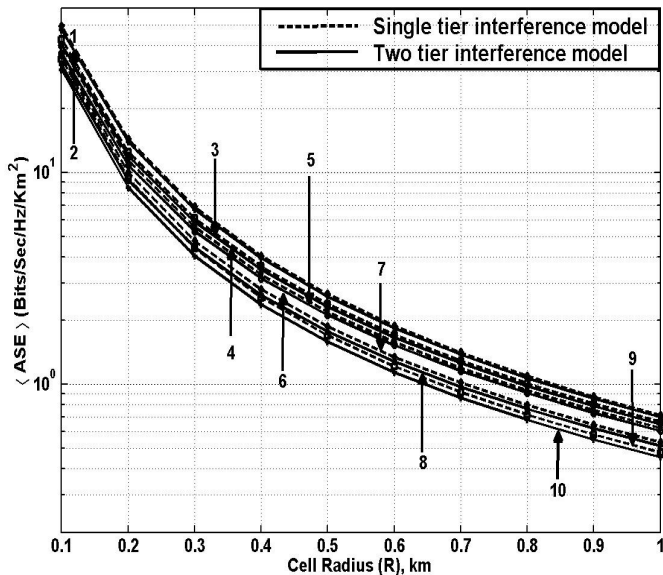


Fig. 7. Average uplink Area Spectral Efficiency (ASE) versus cell radius for three sector cellular system and light vehicular traffic at different carrier frequencies  $f_c$ . (Fully-loaded system with 6 and 12 co-channel interfering cells in first and second tier  $N_{I1} = 6$  and  $N_{I2} = 12$ ; basic and extra path loss exponent:  $\alpha = 2$  and  $\rho = 2$ ; MS and BS antenna heights:  $h_m = 1.5$  m and  $h_b = 15$  m; effective road height  $h = 0.23$  m).

1 - single tier interfering model ( $f_c = 900$  MHz), 2 - two tier interfering model ( $f_c = 900$  MHz), 3 - single tier interfering model ( $f_c = 2$  GHz), 4 - two tier interfering model ( $f_c = 2$  GHz), 5 - single tier interfering model ( $f_c = 3.35$  GHz), 6 - two tier interfering model ( $f_c = 3.35$  GHz), 7 - single tier interfering model ( $f_c = 8.45$  GHz), 8 - two tier interfering model ( $f_c = 8.45$  GHz), 9 - single tier interfering model ( $f_c = 15.75$  GHz), 10 - two tier interfering model ( $f_c = 15.75$  GHz).

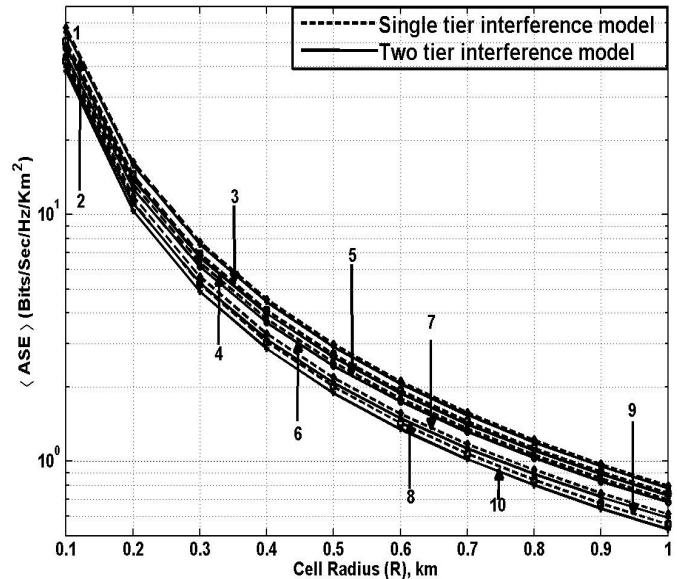


Fig. 9. Average uplink Area Spectral Efficiency (ASE) versus cell radius for six sector cellular system at different carrier frequencies  $f_c$ . (Fully-loaded system with 6 and 12 co-channel interfering cells in first and second tier  $N_{I1} = 6$  and  $N_{I2} = 12$ ; basic and extra path loss exponent:  $\alpha = 2$  and  $\rho = 2$ ; MS and BS antenna heights:  $h_m = 1.5$  m and  $h_b = 15$  m; effective road height  $h = 0.23$  m).

1 - single tier interfering model ( $f_c = 900$  MHz), 2 - two tier interfering model ( $f_c = 900$  MHz), 3 - single tier interfering model ( $f_c = 2$  GHz), 4 - two tier interfering model ( $f_c = 2$  GHz), 5 - single tier interfering model ( $f_c = 3.35$  GHz), 6 - two tier interfering model ( $f_c = 3.35$  GHz), 7 - single tier interfering model ( $f_c = 8.45$  GHz), 8 - two tier interfering model ( $f_c = 8.45$  GHz), 9 - single tier interfering model ( $f_c = 15.75$  GHz), 10 - two tier interfering model ( $f_c = 15.75$  GHz).

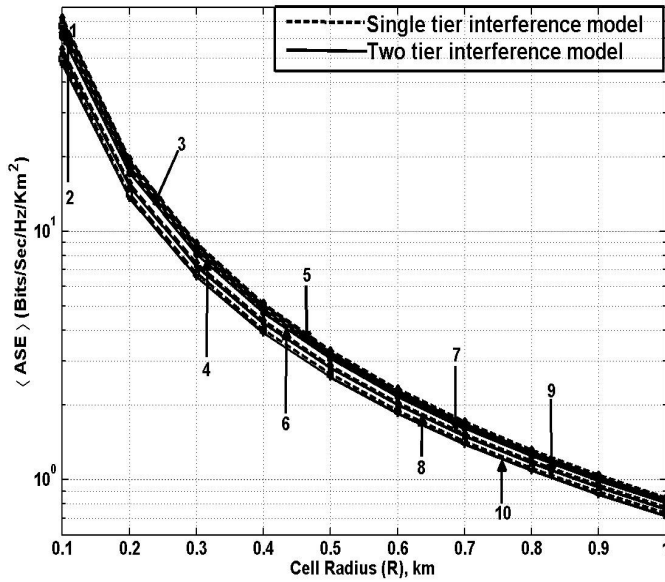


Fig. 10. Average uplink Area Spectral Efficiency (ASE) versus cell radius for six sector cellular system at different carrier frequencies  $f_c$ . (Fully-loaded system with 6 and 12 co-channel interfering cells in first and second tier  $N_{I1} = 6$  and  $N_{I2} = 12$ ; basic and extra path loss exponent:  $\alpha = 2$  and  $\rho = 2$ ; MS and BS antenna heights:  $h_m = 1.5$  m and  $h_b = 15$  m; effective road height  $h = 1.3$  m).

1 - single tier interfering model ( $f_c = 900$  MHz), 2 - two tier interfering model ( $f_c = 900$  MHz), 3 - single tier interfering model ( $f_c = 2$  GHz), 4 - two tier interfering model ( $f_c = 2$  GHz), 5 - single tier interfering model ( $f_c = 3.35$  GHz), 6 - two tier interfering model ( $f_c = 3.35$  GHz), 7 - single tier interfering model ( $f_c = 8.45$  GHz), 8 - two tier interfering model ( $f_c = 8.45$  GHz), 9 - single tier interfering model ( $f_c = 15.75$  GHz), 10 - two tier interfering model ( $f_c = 15.75$  GHz).

radius  $R = 0.1$  km, the decrease in the information capacity between the two interference models was 3.73, 5.17, 6.33, 8.45 and 9.53%. For 0.3 km, the decrease in the information capacity between the two interference model was 2.52, 3.19, 3.82, 5.66 and 7.05%, and for 0.5 km, it was 2.25, 2.69, 3.14, 4.54 and 5.87%.

For the six sector and heavy vehicular traffic the decrease in information capacity between the two interference models for carrier frequencies  $f_c = 0.9, 2, 3.35, 8.45$  and  $15.75$  GHz, at cell size radius  $R = 0.1$  km, is 2.29, 2.65, 3.03, 4.24 and 5.47%. For 0.3 km, the decrease in the information capacity

TABLE V  
DECREASE IN ASE BETWEEN THE TWO INTERFERENCE MODEL:  
THREE-SECTOR CELLULAR SYSTEM/LIGHT VEHICULAR TRAFFIC  
 $h_m = 1.5$  m,  $h_b = 15$  m,  $h = 0.23$  m and  $\alpha = 2$

Cell Radius (km)	Carrier Frequency	Decrease in ASE (%)
0.1	900 MHz	4.31
	2 GHz	6.02
	3.35 GHz	7.42
	8.45 GHz	10
	15.75 GHz	11.24
0.3	900 MHz	2.84
	2 GHz	3.64
	3.35 GHz	4.46
	8.45 GHz	6.56
	15.75 GHz	8.23
0.5	900 MHz	2.48
	2 GHz	3.00
	3.35 GHz	3.59
	8.45 GHz	5.19
	15.75 GHz	6.76

TABLE VI  
DECREASE IN ASE BETWEEN THE TWO INTERFERENCE MODEL:  
THREE-SECTOR CELLULAR SYSTEM/HEAVY VEHICULAR TRAFFIC  
 $h_m = 1.5$  m,  $h_b = 15$  m,  $h = 1.3$  m and  $\alpha = 2$

Cell Radius (km)	Carrier Frequency	Decrease in ASE (%)
0.1	900 MHz	2.55
	2 GHz	2.97
	3.35 GHz	3.45
	8.45 GHz	4.91
	15.75 GHz	6.40
0.3	900 MHz	2.15
	2 GHz	2.30
	3.35 GHz	2.49
	8.45 GHz	3.10
	15.75 GHz	3.81
0.5	900 MHz	1.91
	2 GHz	2.17
	3.35 GHz	3.55
	8.45 GHz	2.69
	15.75 GHz	3.16

TABLE VII  
DECREASE IN ASE BETWEEN THE TWO INTERFERENCE MODEL: SIX-SECTOR  
CELLULAR SYSTEM/LIGHT VEHICULAR TRAFFIC  
 $h_m = 1.5$  m,  $h_b = 15$  m,  $h = 0.23$  m and  $\alpha = 2$

Cell Radius (km)	Carrier Frequency	Decrease in ASE (%)
0.1	900 MHz	3.73
	2 GHz	5.17
	3.35 GHz	6.33
	8.45 GHz	8.45
	15.75 GHz	9.53
0.3	900 MHz	2.52
	2 GHz	3.19
	3.35 GHz	3.82
	8.45 GHz	5.66
	15.75 GHz	7.05
0.5	900 MHz	2.25
	2 GHz	2.69
	3.35 GHz	3.14
	8.45 GHz	4.54
	15.75 GHz	5.87

between the two interference model was 2.0, 2.08, 2.23, 2.78 and 3.36%, and at 0.5 km, it was 1.87, 2.0, 2.07, 2.39 and 2.78%. These results are tabulated in Table VII and VIII.

From these results, we can conclude that, for a sectorized cellular system, operating at higher carrier frequency and having smaller cell size radius in a traffic environment, the second tier co-channel interference still becomes dominant. The result confirms the need to include second tier co-channel interference in the information capacity performance analysis of future and emerging cellular wireless communication systems. We can also conclude that the presence of vehicles and pedestrians in the environment tends to mitigate the severity of the co-channel interference.

## V. CONCLUSION

In this paper, because of the importance of co-channel interference on the information capacity performance of cellular system, we have shown that even for sectorized cellular wireless system operating at carrier frequency greater than 2 GHz and smaller cell size radius, in a traffic environment second tier co-channel interference still becomes dominant. Therefore there is a need to include second tier co-channel interference in the design and system model of

TABLE VIII  
DECREASE IN ASE BETWEEN THE TWO INTERFERENCE MODEL:  
THREE-SECTOR CELLULAR SYSTEM/HEAVY VEHICULAR TRAFFIC  
 $h_m = 1.5$  m,  $h_b = 15$  m,  $h = 1.3$  m and  $\alpha = 2$

Cell Radius (km)	Carrier Frequency	Decrease in ASE (%)
0.1	900 MHz	2.29
	2 GHz	2.65
	3.35 GHz	3.03
	8.45 GHz	4.24
	15.75 GHz	5.47
0.3	900 MHz	2.0
	2 GHz	2.08
	3.35 GHz	2.23
	8.45 GHz	2.78
	15.75 GHz	3.36
0.5	900 MHz	1.87
	2 GHz	2.0
	3.35 GHz	2.07
	8.45 GHz	2.39
	15.75 GHz	2.78

emerging and future cellular wireless communication systems. Future work will focus on including multiple tiers of co-channel interfering cells, correlation coefficient, shadowing and multipath fading. In future we will also use more realistic propagation and system model's scenario in terms of user's distribution and radio environment.

#### REFERENCES

- [1] W. C. Y. Lee, "Spectrum efficiency in cellular," *IEEE Trans. Veh. Technol.*, vol. 38, pp. 69–75, May 1989.
- [2] K. Pahlavan and A. H. Levesque, "Wireless data communication," *proc. IEEE*, vol. 82, pp. 1398–1430, Sept. 1994.
- [3] Y. Yao and A. U. H. Sheikh, "Investigations into co-channel interference in microcellular mobile radio systems," *IEEE Trans. Veh. Technol.*, vol. 41, no. 2, pp. 114–121, May 1992.
- [4] T. K. Sarkar, Z. Ji, K. Kim, A. Medouri, and M. Salazar-palma, "A survey of various propagation models for mobile communication," *IEEE Trans. Antennas Propagat.*, vol. 45, pp. 51–74, Jun. 2003.
- [5] S. Zhou, M. Zhao, X. Xu, J. Wang, and Y. Yao, "Distributed wireless communication system: a new architecture for future public wireless access," *IEEE Commun. Mag.*, vol. 41, pp. 108–113, 2003.
- [6] J. Takada, J. Fu, H. Zhu, and T. Kobayashi, "Spatio-temporal channel characterization in a suburban non line-of-sight microcellular environment," *IEEE J. Select. Areas Commun.*, vol. 20, no. 3, pp. 532–538, April 2002.
- [7] H. Masui, T. Kobayashi, and M. Akaike, "Microwave path-loss modeling in urban line-of-sight environments," *IEEE J. Select. Areas Commun.*, vol. 20, no. 6, pp. 1151–1155, Aug 2002.
- [8] G. Hernández-valdez, F. A. Cruz-pérez, and D. Lara-rodríguez, "Sensitivity of the system performance to the propagation parameters in los microcellular environments," *IEEE Trans. Veh. Technol.*, vol. 57, no. 6, pp. 3488–3508, Nov. 2008.
- [9] V. H. Macdonald, "The cellular concept," *Bell Systems Technology Journal*, vol. 58, no. 1, pp. 15–41, Jan. 1979.
- [10] P. Harley, "Short distance attenuation measurements at 900 mhz and 1.8 ghz using low antenna heights for microcells," *IEEE J. Select. Areas Commun.*, vol. 7, no. 1, pp. 5–11, Jan. 1989.
- [11] Y. Liang, A. Goldsmith, G. Foschini, R. Valenzuela, and D. Chizhik, "Evolution of base station in cellular networks: denser deployment versus coordination," *IEEE international conference on communications*, pp. 4128 – 4132, May 2008.
- [12] K. A. Anang, P. B. Rapajic, T. I. Eneh, and Y. Nijssure, "Minimum cell size for information capacity increase in cellular wireless network," in *Proc. 73rd IEEE Vehicular Technology Conference (VTC'2011)*, Budapest, Hungary, May 2011, pp. 305–311.
- [13] K. A. Anang, P. B. Rapajic, T. I. Eneh, L. Bello, and G. Oletu, "Impact of vehicular traffic on information capacity of cellular wireless network at carrier frequencies greater than 3 ghz," in *Proc. 5th IEEE European Modelling Symposium on Mathematical modelling and Computer Simulation (EMS' 2011)*, Madrid, Spain, Nov. 2011, pp. 430–434.
- [14] K. A. Anang, P. B. Rapajic, and R. Wu, "Impact of sectorization on the minimum cell size for information capacity increase in cellular wireless network," in *IX International Symposium Industrial Electronics (INDEL'2012)*, Banja Luka, Bosnia and Herzegovina, Nov. 2012, pp. 220–225.
- [15] W. C. Y. Lee, *Mobile communication design fundamentals*. New York, NY: John Wiley & Sons, 1993, p. 142.
- [16] S. Singh, N. B. Mehta, A. F. Molisch, and A. Mukhopadhyay, "Moment matched lognormal modeling of uplink interference with power control and cell selection," *IEEE Trans. Wireless Commun.*, vol. 9, no. 3, pp. 932 – 938, Mar. 2010.
- [17] D. N. Hatfield, "Measures of spectral efficiency in land mobile radio," *IEEE Trans. Electromagn. Compat.*, vol. emc-19, no. 3, pp. 266–268, Aug. 1977.
- [18] M. Alouini and A. J. Goldsmith, "Area spectral efficiency of cellular mobile radio systems," *IEEE Trans. Veh. Technol.*, vol. 48, no. 4, pp. 1047–1065, Jul. 1999.
- [19] ITU, "Propagation data and prediction methods for planning of short range outdoor radio communication systems and radio local area networks in the frequency range 300 mhz to 100 ghz," Recommendation ITU-R P.1411 - 1, ITU Radio communication Assembly.
- [20] G. TR25.996, "3gpp scm channel models," 3GPP TR25.996, vol. v6.1.0, Sept. 2003.

# Development of the Algorithm for Energy Efficiency Improvement of Bulk Material Transport System

Leposava Ristić, Milan Bebić, and Borislav Jeftenić

**Abstract**—The paper presents a control strategy for the system of belt conveyors with adjustable speed drives based on the principle of optimum energy consumption. Different algorithms are developed for generating the reference speed of the system of belt conveyors in order to achieve maximum material cross section on the belts and thus reduction of required electrical drive power. Control structures presented in the paper are developed and tested on the detailed mathematical model of the drive system with the rubber belt. The performed analyses indicate that the application of the algorithm based on fuzzy logic control (FLC) which incorporates drive torque as an input variable is the proper solution. Therefore, this solution is implemented on the new variable speed belt conveyor system with remote control on an open pit mine. Results of measurements on the system prove that the applied algorithm based on fuzzy logic control provides minimum electrical energy consumption of the drive under given constraints. The paper also presents the additional analytical verification of the achieved results through a method based on the sequential quadratic programming for finding a minimum of a nonlinear function of multiple variables under given constraints.

**Index Terms**—Conveyors, fuzzy logic, optimal control, energy efficiency, mining industry.

*Original Research Paper*  
DOI: 10.7251/ELS1317030R

## I. INTRODUCTION

**E**LECTRICAL energy consumption is increasing globally in order to keep improving our quality of life. Energy efficiency is today one of the key elements in energy policy of all developed countries in the world, because it contributes to the improvement of economy globally and extends the lifetime of conventional energy sources, since the greatest part of total electrical energy is generated by fossil fuels. In many countries, most electrical energy comes from coal, for example in Serbia, 62% of all capacities for energy production is in thermal power plants which use coal, and they produce 65% of total electrical energy production. In the following decades,

the focus will be on thermal power plants to further increase electrical energy capacities, requiring the rise of coal production.

In various branches of industry where bulk materials are produced or used, various types of belt conveyors (BCs) are used for the transport of materials. Continuous mining is used in large open pit mines (OPM), most often in mines where coal is excavated for use in thermal power plants. The mechanization in these types of mines is organized into systems, such as an ECS (excavator - belt conveyor - spreader) for excavating overburden, or an ECSY (excavator - belt conveyor - stock yard) for excavating coal. The BCs which are placed next to the excavator are called bench conveyors and their task is to receive the material from the excavator. The BC which transfers the material into the spreader is called the dump-side conveyor and BCs which connect the bench and dump-side conveyors are called connecting conveyors.

In recent times, very long BCs have been built with lengths of several dozen kilometers. Due to the length of the route and the necessity to shift the route regularly as a result of the technological demands a system of several BCs, i.e. BC stations are formed. BC stations are placed along the envisaged route so that material is transferred from BC to BC several times until it reaches the final destination. The installed power of these BCs is large and each rationalization of energy consumption can provide significant savings, which is naturally of significant interest for a user [1], [2], [3], [4].

There are two possibilities for energy savings in belt conveyors: first affects efficiency of drive components [5], [6], and second applies different control strategies of multi motor drives on belt conveyors [1], [2], [3], [7]. According to this, the paper presents the new BC system in an OPM, which transports overburden from the excavator to the spreader with the system of five BCs, with all aspects for energy efficiency improvement considered and applied in its realization. The belt drive of BC station is with a belt width of 2000 mm and has installed power of 4 MW, meaning the entire system has installed power of 20 MW. Modern belt conveyor systems are highly sophisticated systems which can be realized with remote control from the control centre of the OPM. Remote control makes full use of advances in modern technologies to increase safety, reliability and productivity levels. Control of

Manuscript received 12 April 2013. Received in revised form 24 May 2013. Accepted for publication 30 May 2013.

L. Ristić, M. Bebić and B. Jeftenić are with the Faculty of Electrical Engineering, University of Belgrade, Belgrade, Serbia (Leposava Ristić is corresponding author phone: +381-11-3218-364; fax: +384-86-81; e-mail: lela@etf.rs).

the BC system as a whole in the view of improved energy efficiency is possible only if the remote control is utilized.

Bulk material transported by a BC can be distributed along the length of the belt in various ways depending on how the material is deposited onto the conveyor. The quantity of material which is transported within a unit of time, or the average capacity, can be expressed with the general formula:

$$Q = \frac{1}{T} \int_0^T A(t) \cdot v(t) dt. \quad (1)$$

The instantaneous quantity of bulk material which is being transported using a BC depends on the operational mode of the system within which the BC is used. In a large number of cases, this quantity is variable and most often the instantaneous cross section area of material on the belt is less than the rated value. Since BC often operates at a decreased capacity, the same quantity of material can be transferred in two ways: with a constant rated speed ( $v_r$ ) and smaller cross section of material on the belt ( $A(t)$ ), or with rated cross section area of material ( $A_r$ ), but at a lower than rated speed ( $v(t)$ ), as shown in Fig. 1.

It has been shown in [1], that most often in practice  $A(t) < A_r$ , meaning that if the speed is modified according to (2), the BC could operate at a lower than rated speed.

$$v(t) = \frac{A(t)}{A_r} v_r \quad (2)$$

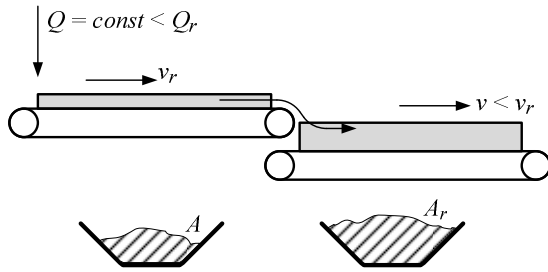


Fig. 1. Two BCs in a series connection - cross section of material on a belt.

Operation of conveyor at lower than rated speed would naturally lead to a decrease in the amount of energy needed to conduct transport [1], [2], [3], [8]. Therefore, if the speed is adjusted according to (2) for the transport of a certain quantity of material, savings of energy will be achieved based on the decreased power necessary for driving the belt.

The paper presents different algorithms which are developed for generating the reference speed of the system of belt conveyors as a function of instantaneous cross section of material on the belt, in order to achieve minimum electrical energy consumption but to avoid potential spillage of material, activation of electrical braking and unnecessary stress of belts and mechanical assemblies. Analyses performed on the detailed mathematical model of the conveyor with rubber belt indicate that the application of the algorithm based on fuzzy logic control will be the proper solution. The validation of the proposed idea is achieved through experimental results recorded on an existing system of belt conveyors in an open pit mine. The presented results are further compared with results of the other approach to optimum speed determination.

According to this approach, results for the optimum speed of BC are obtained „off - line” for the same incoming material, i.e. for the same input variable  $Q_{in}$ , applying the method of sequential quadratic programming and using the new identified function for average power of BC drive. It is proved that optimum speed is determined with both approaches, providing the minimum of electrical energy consumption under given constraints of the considered system of belt conveyors.

## II. DEVELOPMENT OF THE ALGORITHM FOR GENERATING REFERENCE SPEED OF BELT CONVEYOR DRIVE

### A. Algorithm with Constant Deceleration

Speed control of a BC requires information about the quantity of material which is deposited onto the belt, meaning the instantaneous capacity must be known.

The instantaneous capacity is:

$$Q(t) = \frac{dV(t)}{dt} = A(t) \cdot v(t) = A(t) \cdot v_{const} \sim A(t). \quad (3)$$

The speed of the belt onto which the material is deposited should be modified in accordance with (2) in order to achieve the defined criteria of speed control. However, the instantaneous capacity changes quite frequently and sporadically. This means that the speed should be increased and decreased in the same manner as the instantaneous capacity changes. These dynamic processes would be unfavorable for the mechanical assemblies of a BC, especially for the belt, and could lead to increased energy consumption.

Because of the fact that the instantaneous capacity changes and those changes cannot be predicted, the control algorithm must be such that the belt speed is adjusted to the conditions at the beginning of the conveyor, i.e. at the location where the instantaneous capacity is measured.

The algorithm for generating the reference speed of the belt drive with constant deceleration is defined as follows:

1. The theoretical belt speed is calculated on the basis of the equation (2), and can be expressed as its special case when a BC in the system of BCs is considered:

$$v_t(t) = \frac{A_{in}(t)}{A_r} v_{in}(t). \quad (4)$$

In (4)  $A_{in}(t)$  and  $v_{in}(t)$  are the instantaneous value of cross section of incoming material and the instantaneous speed of the previous belt.

The actual reference speed of the belt drive  $v_{ref}(t)$  is calculated on the basis of (4) according to (6) under the conditions defined by (5):

$$\frac{dv_t(t)}{dt} \geq 0 \quad \text{and} \quad v_t(t) - v_{ref}(t) \geq \varepsilon, \quad (5)$$

$$v_{ref}(t) = c \cdot \int (v_t(t) - v_{ref}(t)) dt + v_{ref}(t_1), \quad (6)$$

where  $t_1$  is the moment when both conditions defined by (5) are acquired,  $c$  and  $\varepsilon$  are constants with dimensions  $[s^{-1}]$  and  $[\%]v_r$  respectively, while  $dv_t/dt$  is time derivative of theoretical belt speed with the dimension of  $[s^{-1} \cdot \%]v_r$ .

2. When the conditions from (5) are not fulfilled, i.e.

$$\frac{dv_t(t)}{dt} < 0 \quad \text{and} \quad v_t(t) - v_{ref}(t) < -\varepsilon, \quad (7)$$

the actual reference speed is determined on the basis of (8),

$$v_{ref}(t) = v_{ref}(t_2) - k \cdot (t - t_2), \quad (8)$$

where  $t_2$  is the moment when at least one of the conditions from (7) ceases to be valid and  $k$  is deceleration.

If it is desired for the BC to constantly operate at the rated speed, then, using the „Operating mode” signal, the status of switch P2 is selected as „0”, and then the reference speed is determined using the expression (9).

$$v_{ref}(t) = c \cdot \int (v_r - v_{ref}(t)) dt + v_{ref}(t_3) \quad (9)$$

Block diagram of the described algorithm is shown in Fig. 2. During the period when the quantity of material coming onto the conveyor increases, the reference speed of the drive is determined according to (6), and at that time the drive accelerates. The constant  $c$  determines the dynamic of reference speed. In this manner the cross section of the material on the speed controlled belt increases, meaning it gravitates towards  $A_r$ . When the quantity of incoming material decreases, the reference speed is calculated based on (8), i.e. the speed decreases with a deceleration  $k$ . The speed adjustment range is limited, minimum speed should be 50% of the rated speed; the maximum speed is set at 100 - 125%, dependant on the capacity of excavator and working conditions.

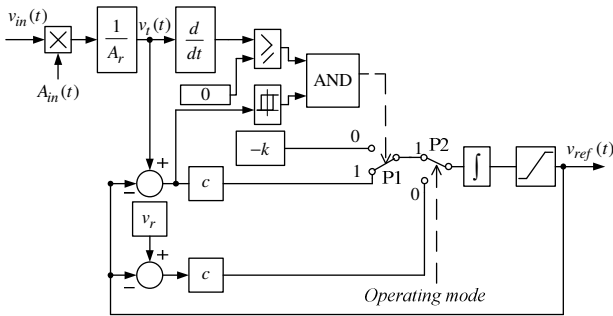


Fig. 2. Algorithm for generating the reference speed of the belt with constant deceleration.

When material is deposited to the beginning of the belt at a constant speed ( $v_{const}$ ), then the cross section area of material at the transfer point is proportional to the instantaneous capacity of the material which is being deposited. In this case, the capacity which is obtained in this manner is proportional to  $A_{in}(t)$ . If it is not the case, i.e. the material is deposited to the beginning of the belt at a speed which is not constant, but is the result of the algorithm shown in Fig. 2, then the cross section area of material at the transfer point must be calculated in accordance with the conservation of capacity, as in (10), for the transfer point between two BCs,  $(i-1)$  and  $i$ -th,

$$A_{(i)in}(t) = \frac{A_{(i-1)out}(t)}{v_{(i)}(t)} \cdot v_{(i-1)}(t). \quad (10)$$

According to (10), the cross section at the end of the  $(i-1)$  belt must be determined. Calculation is conducted by

„monitoring” the movement of material along the belt over time. This can be performed by dividing the belt into sections of constant length. The length of these sections is determined so that a constant cross section of material can be observed along its entire length. The cross section area of material on one such section is entered into the memory, i.e., registry. The number of registries  $R$  is:

$$R = \frac{L}{L_{regi}} \in \mathbb{N}. \quad (11)$$

The upper side of the belt, meaning the side where the material is located, is represented by series containing an  $R$  number of registries. Entering of data into the registry is done in accordance with the selection time which corresponds to the time necessary for the belt to travel a distance of  $L_{regi}$ . The time when the data is entered (the sampling instant) is determined using a logical block with a resettable integrator, according to (12). The registries are organized in a series so that at the sampling instant the earlier recorded values are shifted into the next registry and new value is entered into the first registry.

$$trigger = \begin{cases} 0 & \int v(t) dt < L_{regi} \\ 1 & \int v(t) dt = L_{regi} \end{cases} \quad (12)$$

The constant  $k$  determines the deceleration of the drive which must confirm with the dynamic characteristics of the drive. An abrupt deceleration unfavorably affects all mechanical assemblies, couplings, bearings, the belt, etc. BC drives with a route which does not traverse an incline use braking with a resistor and chopper in the DC circuit. An abrupt deceleration would lead to the activation of the electric braking system whereby the braking energy would unnecessarily transform into heat within the resistors.

Regarding these conditions and constraints a value for constant  $k$  is empirically determined and applied in the algorithm for generating the reference speed of the belt on the system of five belt conveyers in an open pit mine. The results of measurements performed on the system are given in [4]. These results show that the maximum value of the material cross section on the belt is not achieved due to two reasons: the minimum speed is limited to 50% of the rated speed and the speed does not exactly follow the reduction of the instantaneous material cross section on the belt due to constant value of deceleration. As the absolute value of constant  $k$  decreases, the deviation from the maximum material cross section increases, but the activation of the electric braking system is avoided in all modes of operation, except in the case of emergency stop. Therefore, the system of belt conveyors does not operate with maximum efficiency.

#### B. Algorithm with Fuzzy Logic Control of Instantaneous Material Cross Section on the Belt: FLC - Case A

To further improve the algorithm for generating reference speed, modifications concerning deceleration  $k$  should be analyzed. Based on analytical considerations and results of simulations performed on mathematical model of belt

conveyor, it can be concluded that average power and average belt speed under the given constraints, have their minimum values if the belt runs with speed proportional to material at its input, i.e. with the theoretical belt speed  $v_i(t)$ . In this case, during the period of deceleration, time derivative of speed will have its maximum absolute value, hence further increase will cause spillage of material over the belt. Also, in cases when value of incoming material cross section onto the belt has big or frequent variations, this maximum absolute value of time derivative of speed during deceleration can activate electric braking system and therefore, it could not be allowed.

When reference speed of BC is the result of the applied algorithm with constant deceleration, the BC drive starts to decelerate always when the condition  $dv_i(t)/dt < 0$  is fulfilled, consequently reducing the range of BC operation with the theoretical belt speed  $v_i(t)$ . To improve the algorithm for generating reference speed, the range of BC operation with the theoretical belt speed  $v_i(t)$  must be extended.

As nonlinear system is to be controlled, the control methodology has to be nonlinear, too. Therefore, the authors of the paper propose different methodology to develop the algorithm for generating the reference speed of the belt, which is based on fuzzy logic control of instantaneous material cross section on the belt, since the adjustment of belt speed is in accordance to the variance of instantaneous material cross section on the belt.

Fuzzy logic based control has been successfully employed in the large number of scientific and engineering applications, as well as numerous commercial applications and industrial systems. In this paper, a knowledge based control algorithm, called fuzzy logic control is proposed to solve the minimization problem, i.e. to drive the system with minimum electrical power, meaning to convey the maximum cross section of material at optimum speed.

The block diagram of the algorithm with fuzzy logic control of instantaneous material cross section on the belt is shown in Fig. 3. As explained earlier, the material which is deposited onto the beginning of each speed controlled BC in the system is not measured then calculated. In accordance with (10), fuzzy control which is found to calculate the speed reference of each BC in the system requires three values to be provided: speed of the observed BC, speed of the previous BC and cross section of incoming material from the previous BC. All of them are achieved with SCADA system.

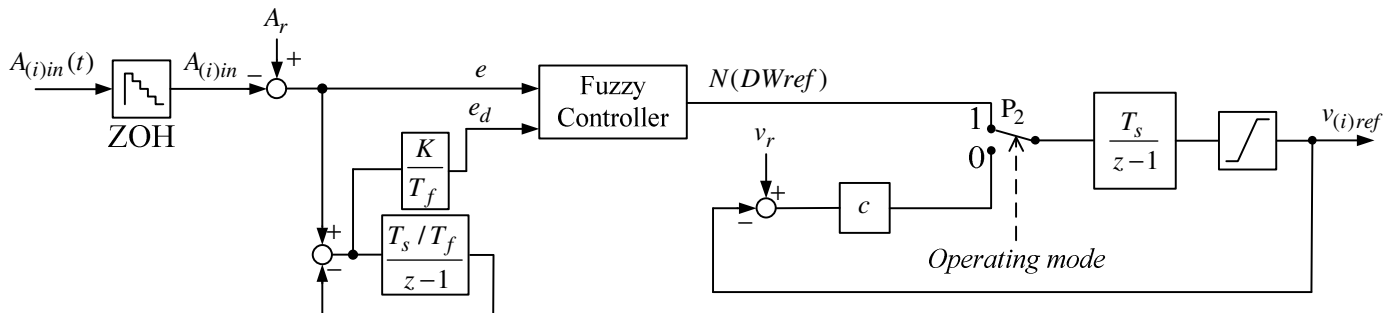


Fig. 3. Algorithm for generating the reference speed of the  $i$ -th BC in the BC system with FLC - case A.

As it can be seen from Fig. 3, the FLC - case A has two inputs: the first input  $e$ , which presents the deviation of the instantaneous material cross section from the rated value and the second  $e_d$ , which presents the derivative of the first input. The „practical differentiator” is applied for the variable  $e_d$ , to provide derivation and filtration of the variable  $e$  in the same time, instead of using these two functions separately.  $T_s$  is sample time,  $T_f$  is time constant of discrete filter and  $K$  is constant which adjusts the value of variable  $e_d$  to its universe of discourse. FLC - case A has single output variable  $N(DWref)$ , which presents an increment of the reference speed, generated from fuzzy rule base given in Table I. Membership functions for the input  $e$  are given in Fig. 4, membership functions for the input  $e_d$ , are given in Fig. 5, and membership functions for the output  $N(DWref)$  are given in Fig. 6.

Values for input and output variables are normalized with base values selected in accordance with rated parameters of motor and the belt conveyor, given in the Appendix. FLC - case A is based on Mamdani's reasoning methods, developed using Fuzzy Logic Toolbox [9] and integrated into Matlab Simulink dynamic model of BC, which is presented in [10].

TABLE I  
FUZZY RULES FLC - CASE A

$e \backslash e_d$	N	NS	ZE	P
N	P	PS	PS	PS
ZE	PS	PS	ZE	NS
P	ZE	ZE	NS	NS

In the process of fuzzification, the universe of discourse for linguistic variable  $e$  is mapped in the  $[-1, 1]$  interval and divided into 4 fuzzy sets: negative (N), negative small (NS), zero (ZE) and positive (P). The universe of discourse for the linguistic variable  $e_d$  is mapped in the  $[-0.5, 0.5]$  interval and divided into 3 fuzzy sets: negative (N), zero (ZE) and positive (P). The universe of discourse for the linguistic variable  $N(DWref)$  is mapped in the  $[-0.3, 1]$  interval and divided into 4 fuzzy sets: negative small (NS), zero (ZE), positive small (PS) and positive (P). The MIN-MAX method is used for fuzzy rules processing, while the centre of gravity method is used for defuzzification.

The desired performance of the system is accomplished with small number of fuzzy sets per variable. This reduces the size of table of fuzzy rules and simplifies the implementation. Considering rules given in the Table I, it can be concluded that the reduction of speed is applied only in three cases: when instantaneous material cross section on the belt has smaller than maximum value (variable  $e$  is P) and this value decreases or stays unchanged (variable  $e_d$  is P or ZE). In all other cases speed reference is increased or kept unchanged, in order to avoid spillage of material over the belt.

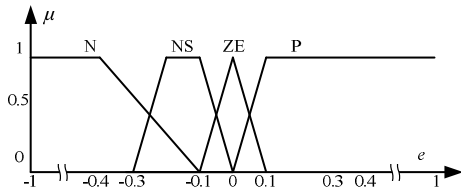


Fig. 4. Membership functions for input variable  $e$ .

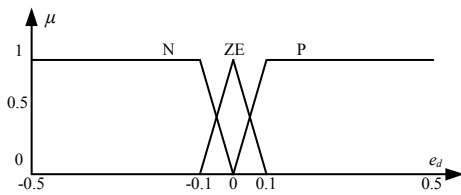


Fig. 5. Membership functions for input variable  $e_d$ .

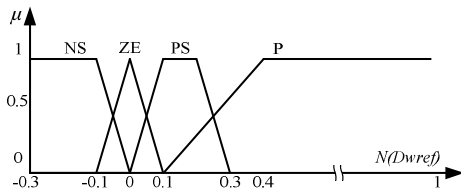


Fig. 6. Membership functions for input variable  $N(DWref)$ .

The performance of the algorithm is tested in cases which best illustrate the developed control strategy, with actual constraints of the system considered and added into the simulation conditions. Results of simulations are given in Fig. 7. In the observed system of five BCs, the first two BCs are bench conveyors and are running at constant speed, while the other three have the speed reference generated with the proposed algorithm. The third BC in the system is considered. The material cross section is measured at the end of the second belt,  $A_{2out}$ . The following simulation was conducted: the belt with incoming material of 20% was started with rated speed, then the speed control was turned on at time  $t = 40s$ ; then the incoming material was increased to 90% of rated value, and at the end, the incoming material was suddenly decreased to the starting value. The presented results show that during the instantaneous and short – term increase of the incoming value of material cross section on the third belt, the control algorithm provides maximum acceleration in order to avoid spillage of material over the belt. Also, the control algorithm provides maximum deceleration, but without braking in the case of sudden decrease of incoming flow of material on the BC.

The other test of the applied control strategy is performed on the mathematical model, too. In this case, time dependency

of the incoming material is with a sine component  $A_{in}(t) = A_{av} + A_{sin} \cdot \sin((2 \cdot \pi / T_{sin}) \cdot t)$ . This signal is selected to simulate the way in which the excavator is depositing material on the BC. Again, the presented results of simulation in Fig. 8 show that the value of the material cross section on the BC is maintaining maximum. Small variations around the maximum value are due to lagging of actual BC speed to reference speed, which follows the shape of material, with required acceleration and maximum deceleration – without braking.

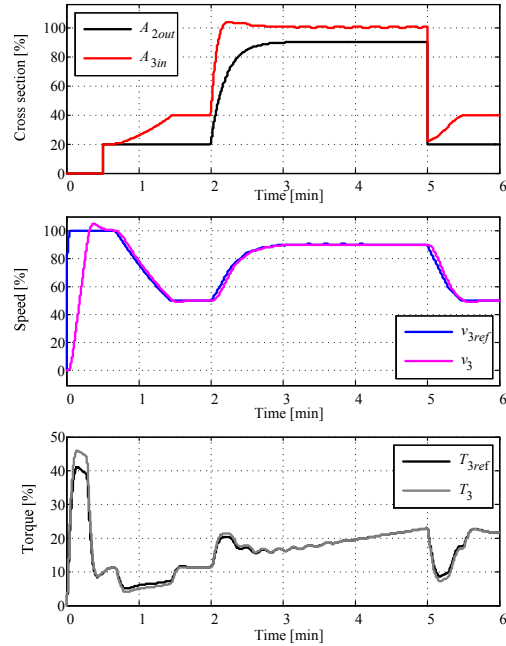


Fig. 7. Characteristic values of the third belt with FLC - case A: transition period from constant speed operation to controlled speed operation with changes of the incoming material from 20% to 90% of rated value and vice versa, in a realistic way that can be expected in practice.

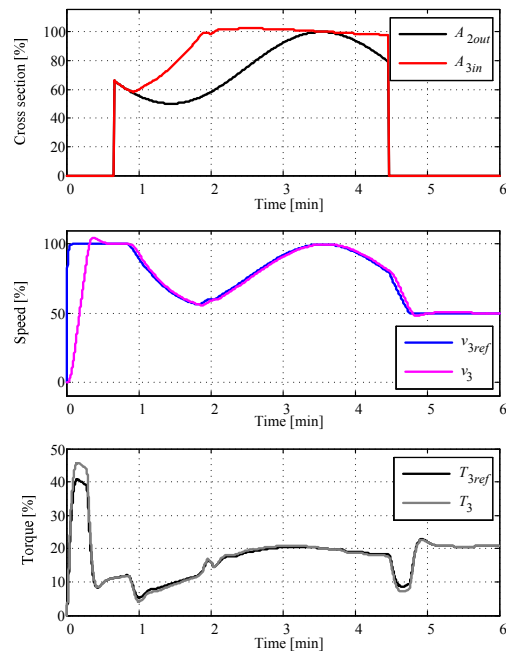


Fig. 8. Characteristic values of the third belt with FLC - case A: transition period from constant speed operation to controlled speed operation with sinusoidal changes of the incoming material.

The algorithm is generating the speed reference based on information of instantaneous value of incoming material cross section onto the belt, without the information about variable motional resistances which are the result of various quantities of material on the belt, different weather conditions and the condition of equipment. This can be a problem, which may cause the activation of electrical breaking system. The required information is included in the information about the instantaneous value of the drive torque. Hence, this value must be considered in order to provide precise control of the reference speed.

### C. Algorithm with Fuzzy Logic Control Which Incorporates Drive Torque: FLC – Case B

Due to aforementioned reasons,  $k$  should be variable to provide deceleration with drive torque nearly zero (but not negative) and therefore operation with minimum energy consumption. It can be determined using the expression (13), derived from the Newtons law,

$$k(t)_{oe} = \frac{T_l(t)}{J_\Sigma(t)} \quad (13)$$

where  $J_\Sigma(t)$  is the total inertia referred to motor shaft, including the effect of material mass. In accordance with DIN22101 standard,  $T_l$  can be expressed as

$$T_l(t) = T_{l0} + T_l(m_{bm}) \quad (14)$$

where  $T_{l0}$  is constant part of the total load torque and  $T_l(m_{bm})$  is a part which is a function of mass of the material on the belt and consequently time dependant. Similar can be derived for the total moment of inertia of the loaded belt conveyor,

$$J_\Sigma(t) = J_{\Sigma 0} + J_\Sigma(m_{bm}), \quad (15)$$

where  $J_{\Sigma 0}$  is a constant part of the total moment of inertia and  $J_\Sigma(m_{bm})$  is a part proportional to mass of the material on the belt and is also time dependant.

The constant part of the load torque, as well as the constant part of the moment of inertia, can be calculated with sufficient accuracy. The values can also be updated from time to time to account for changes in the system of BCs, due to changes of length or changes in condition of the equipment. However, components of load torque and moment of inertia remain unknown since they are functions of mass of material on the belt and external conditions. This leads to inaccurate calculation of  $k$  and inappropriate deceleration of a BC.

Due to aforementioned facts, it can be derived that the

optimum value for  $k(t)$  has to fulfill following three criteria:

1) the absolute value of  $k(t)$  must be less than absolute value of  $\Delta A_{in}/\Delta t$  in the period of deceleration, in order to avoid spillage of material over the belt,

2) technical criteria,  $|k(t)| \leq k_{max\ technical} = 3.5 [s^{-1} \cdot \%] v_r$ , in order to keep stress of belts and mechanical assemblies during the deceleration within tolerance and

3) the criteria for optimum energy consumption under given constraints of the system, defined with (13).

The value  $k_{oe}(t)$  must not be applied during periods of deceleration when  $|k_{oe}(t)| > k_{max\ technical}$ . For this reason, motors of the multi motor drive of BC have to develop torques in accordance with (16).

$$T_e \geq k_{max\ technical} \cdot J_\Sigma(t) - T_l(t) \quad (16)$$

The expression (16) leads to the conclusion that measured value of the drive torque has to be incorporated in the algorithm for generating reference speed, in order to provide operation of the system with optimum  $k(t)$ , within existing operating conditions. This value is achieved with SCADA system, meaning that it is always available.

Fuzzy control was found to calculate acceleration and deceleration, based on measuring three values: speed of previous BC, cross section of incoming material, and the drive torque. The block diagram of the algorithm for generating the reference speed of BC with FLC – case B is shown in Fig. 9. As it can be seen from Fig. 9, FLC – case B has two inputs:  $Dwref$  according to (17),

$$Dwref_{(n)} = v_{t(n)} - v_{ref(n-1)}, \quad (17)$$

and the drive torque  $Te$ . The task of maintaining the torque of the motor at a zero value during periods of deceleration is now provided by the FLC – case B. Therefore, the deceleration is achieved while avoiding all the problems caused with the parameters variation due to external conditions. The FLC – case B is with single output  $N(Dwref)$ . It is based on Mamdani's reasoning methods, developed using *Fuzzy Logic Toolbox* [9] and integrated into *Matlab Simulink* dynamic model of BC, which is presented in [10], as well as FLC – case A.

Membership functions for the input  $Dwref$  are given in Fig. 10, membership functions for the input  $Te$  are given in Fig. 11, and membership functions for the output  $N(Dwref)$  are given in Fig. 12.

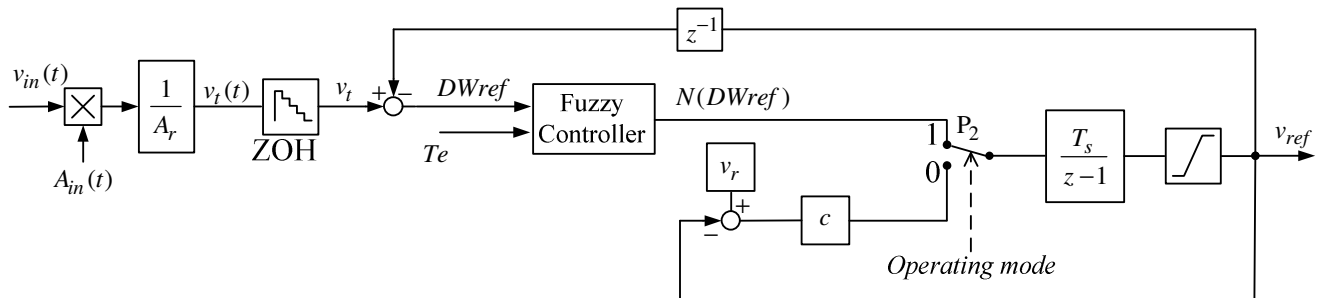


Fig. 9. Algorithm for generating the reference speed of the belt with FLC – case B.

The output variable  $N(Dwref)$  is increment of the reference speed, generated from fuzzy rule base given in Table II. Values for input and output variables are normalized with base values selected in accordance with rated parameters of motor and the belt conveyor, given in the Appendix, as well as for the FLC – case A.

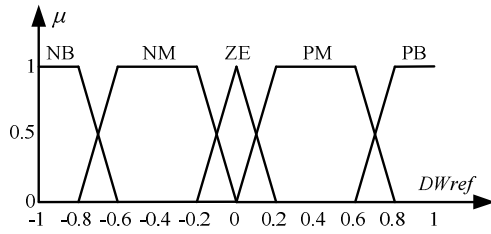


Fig. 10. Membership functions for input variable  $Dwref$ .

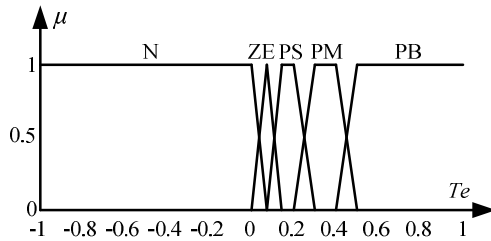


Fig. 11. Membership functions for input variable  $Te$ .

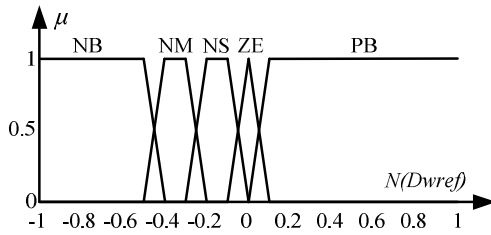


Fig. 12. Membership functions for output variable  $N(Dwref)$ .

In the process of fuzzification, the universe of discourse for linguistic variables  $Dwref$ ,  $Te$  and  $N(Dwref)$  is mapped in the  $[-1, 1]$  interval and divided into fuzzy sets: negative (N), negative big (NB), negative medium (NM), zero (ZE), positive small (PS), positive medium (PM), and positive big (PB). The MIN-MAX method is used for fuzzy rules processing, while the center of gravity method is used for defuzzification.

Considering Table II, three regions can clearly be distinguished and described with fuzzy rules as follows:

- If ( $Te$  is N) then ( $N(Dwref)$  is ZE) - meaning that if drive torque approaches zero, the reference speed increment must converge to zero in order to avoid activation of electrical braking;

- If ( $Dwref$  is ZE) then ( $N(Dwref)$  is ZE) - meaning that if the required change of reference speed is small (zero), then no change of the output value (reference speed increment) is needed, regardless of drive torque value;

- If ( $Dwref$  is PM) then ( $N(Dwref)$  is PB) or

- If ( $Dwref$  is PB) then ( $N(Dwref)$  is PB) - meaning that if incoming material on the belt is increasing, the BC drive must achieve proper acceleration in order to avoid spillage of material over the belt.

TABLE II  
FUZZY RULES FLC - CASE B

$Te \backslash Dwref$	N	ZE	PS	PM	PB
NB	ZE	NS	NM	NB	NB
NM	ZE	ZE	NS	NM	NB
ZE	ZE	ZE	ZE	ZE	ZE
PM	ZE	PB	PB	PB	PB
PB	ZE	PB	PB	PB	PB

The desired performance of the system was accomplished with only five fuzzy sets per variable. This reduces the size of table of fuzzy rules. Distribution of fuzzy sets depends on the requirements of the system. Also it provides adequate control sensitivity. For the input variable  $Te$ , a single fuzzy set „N” denotes braking which should be avoided. When torque is close to zero, high control sensitivity is required, therefore narrow fuzzy sets are defined. For any positive value of the  $Te$ , when the input variable  $Dwref$  is positive, the FLC - case B gives big value at the output in order to avoid spillage of material on the belt. For small variations of input variable  $Dwref$ , i.e. small variations of material cross section at the input of the BC ( $A_{in}$ ), the system has no sudden change of the output variable, which is provided with the adequate tuning of the „ZE” fuzzy sets. The shape of generated control function is given as a surface in Fig. 13. This form is suitable for implementation in PLC as look up table with interpolation between the calculated points.

The described algorithm with FLC - case B for generating the speed reference is developed and tested on the detailed mathematical model of the drive system with the rubber belt [5]. The rule base is fully defined and the controller generates the output within the system limits for every combination of input variables. The systems equipped with smart features which adjust the response of the system under the effect of any unseen loading conditions should be much safe and reliable. Therefore, an adaptive fuzzy controller must be developed [11], which can be the topic of authors' future work.

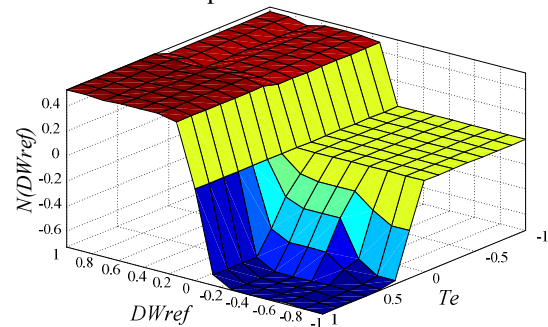


Fig. 13. The shape of generated control function.

The results of measurements of the implemented algorithm on the dump-side conveyor on the new variable speed BC system with remote control on an OPM are presented in Fig. 14. The speed is adjusted in the range from 60% to 100% of the rated speed, as the user demanded. The cross section value of incoming material to the dump-side BC ( $A_{4out}$ ) is

calculated, not measured. Discretization of the input material cross section at the transfer point between two BCs influences all other characteristic values of BC, which are archived with SCADA and presented in Fig. 14.

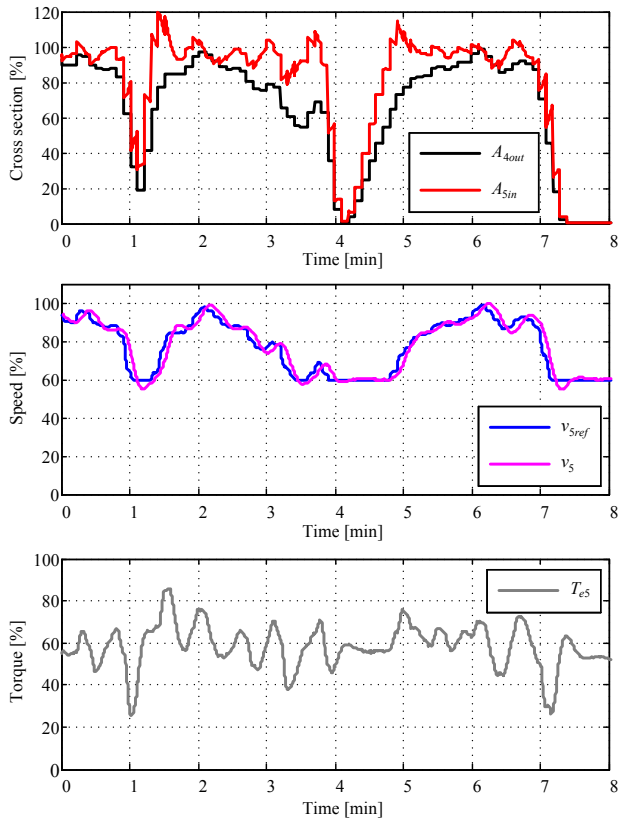


Fig. 14. Characteristic values of the dump-side BC: implementation of the algorithm for generating the reference speed of the belt with FLC - case B (speed control in the range of 60% to 100%  $v_r$ ).

It has been shown by experimental results presented in Fig. 14 that the control strategy with FLC - case B adjusts the speed of the loaded BC in accordance with the quantity of material on the belt, in order to achieve energy saving in normal operation. Variable acceleration and deceleration is performed in such a way to cause minimum stress of mechanical assemblies and the belt. It can also be noticed from presented results that the cross section of material on the belt is sometimes greater than 100% which is the maximum theoretical value. Even when the value of the cross section reaches 116% of the theoretic value, transport can still be conducted without spillage [8].

The measurements which were taken over a longer period of time on a system with an installed power of 20MW confirmed the expected savings in electrical energy consumption. The system operated while alternating between speed control and constant speed, each for several hours. Twenty series of measurements were generated in various exploitation conditions. Data was collected for a period of eight months for three BCs in the system. Fig. 15 provides the data for average power in the individual series of measurements, and Fig. 16 provides data on consumption of electrical energy per cubic meter of transferred overburden. The displayed results show

the reduction of both, average power [MW] and average value of specific energy [kWh/m<sup>3</sup>], in the range from 3% to 19%, comparing to constant speed operation. Hence, the measurements unequivocally confirm the advantage of speed control on BCs, which results in reduced energy consumption.

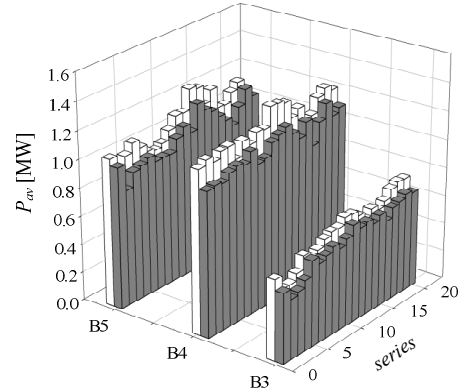


Fig. 15. Average power consumption of belt drives in [MW], on the third, fourth and fifth BC station (B3, B4 and B5): white bars - constant speed operation, grey bars - variable speed operation with FLC - case B.

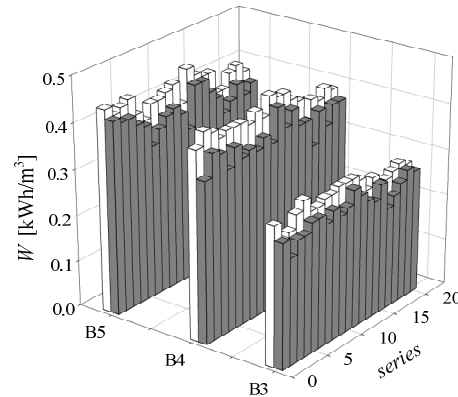


Fig. 16. Consumption of Energy per m<sup>3</sup> [kWh/m<sup>3</sup>], on the third, fourth and fifth BC station (B3, B4 and B5): white bars - constant speed operation, grey bars - variable speed operation with FLC - case B.

### III. THE OPTIMUM SPEED GAINED WITH FLC - CASE B: ANALYTICAL VERIFICATION

A function of mechanical power of belt conveyor drive is developed based on DIN 22101 methodologies for motional resistances calculation. It is presented in [2] as a new „energy model”, which lumps all the parameters into four coefficients,  $\theta_1$ ,  $\theta_2$ ,  $\theta_3$  and  $\theta_4$ . The procedure for least square (LSQ) based „off - line” parameters estimation has been applied to identify coefficients of „energy model” of the observed dump-side BC. The required speed has also been determined using the method of sequential quadratic programming, with the goal to reduce the electrical energy consumption under defined constraints of the system. The result achieved in this way, has been compared with the result of the applied algorithm with FLC - case B.

Mechanical power of the BC drive as a function of capacity and speed, for the defined operating conditions, i.e. „energy model” is given with (18),

$$P(T, v) = \theta_1 \cdot T^2 \cdot v + \theta_2 \cdot v + \theta_3 \cdot \frac{T^2}{v} + \theta_4 \cdot T + \frac{v^2 \cdot T}{3.6} \quad (18)$$

where  $P$  [W] is mechanical power,  $v$  [m/s] is speed and  $T$  [t/h] is mass flow,  $T$  [t/h] =  $\gamma$ [t/m<sup>3</sup>]· $Q$ [m<sup>3</sup>/h]. Mechanical power in steady state operation of the considered dump-side conveyor is calculated for different values of input variables, i.e. capacity and speed. Based on achieved results, the parameter estimation scheme presented in [2] has been applied providing the following values of „energy model” coefficients:  $\theta$  [p.u.] = [0.0036 1.292·10<sup>5</sup> 0.0312 63.4393]<sup>T</sup>. All variables are normalized with base values selected in accordance with rated parameters of motor and the BC, given in the Appendix. Steady state characteristics for  $P_{av} = f(v, Q = \text{const})$ , given in Fig. 16, are calculated with the estimated parameters  $\theta_1, \theta_2, \theta_3$  and  $\theta_4$ , for different values of capacity  $Q$  (from 0.5 to 1 [p.u.]), by varying speed in the range of  $v = [0.4, \dots, 1]$  [p.u.]. For speed values less than 0.4 p.u., the relation (17) is inappropriate, therefore, different functional dependency for  $P_{av} = f(v, Q)$  has to be established. Nonetheless, the performed analysis does not apply in this range. Two more characteristics,  $P_{av} = f(v, A_{max})$  and  $P_{av \min} = f(v, Q)$ , are also presented in the same figure. The presented results clearly show that the characteristic for  $P_{av \min}$  is to the left of the characteristic  $P_{av} = f(v, A_{max})$ . Consequently, the considered BC will not be able to operate at speed which provides minimum energy consumption, because it will cause the spillage of material over the belt. Due to this reason, the BC can operate only with speeds equal or higher than the speeds determined by the characteristic  $P_{av} = f(v, A_{max})$ . Hence, the true minimum of energy consumption will not correspond to the absolute minimum of average mechanical power ( $P_{av}$ ), but to the average mechanical power, which is determined in accordance with the constraint of maximum capacity.

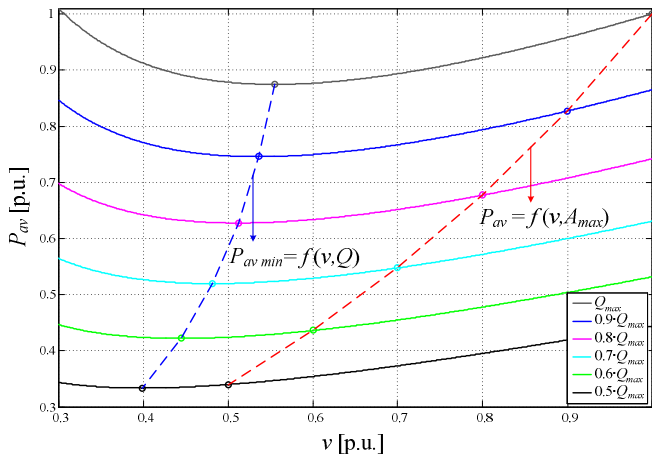


Fig. 16. Characteristics for  $P_{av} = f(v, Q = \text{const})$ .

Belt conveyors in OPMs always work in the system with excavators and spreaders for the purpose of material handling, so their energy efficiency is affected by many constrains which exist at the equipment or system level. In practice, many belt conveyors are working with reduced capacity, even with empty belts, due to problems which may occur during the system

operation. The paper deals with the optimization problem which is dedicated to optimize the belt conveyor speed under a reduced capacity and under defined system constraints, in order to minimize electrical energy consumption. Hence, the analytical expression for electrical energy consumption is employed as the objective of this problem for minimization. The belt speed is within its defined limits, as well as maximum mass per unit of belt length. They form the constraints of this problem. As additional constraint, the range for time derivative of speed is also introduced. This especially refers to deceleration coefficient which has to fulfill following three criteria, defined in the previous section. Therefore, the optimization problem is formulated as follows,

$$\begin{aligned} \min W_{el}(v_j, Q_j : 1 \leq j \leq N) &= \sum_{j=1}^{j=N} \frac{1}{\eta} P(v_j, Q_j) t_s \\ \text{subject to:} & \\ 0.5 \cdot v_{max} \leq v_j \leq v_{max} & \\ \frac{\Delta v_{min}}{t_s} \leq \frac{v_j - v_{j-1}}{t_s} \leq \frac{\Delta v_{max}}{t_s} & \left. \vphantom{\frac{\Delta v_{min}}{t_s}} \right\} \text{linear constraints} \\ 0 \leq M'_{Lj} \leq M'_{Lmax} & \text{nonlinear constraints} \end{aligned} \quad (19)$$

where  $\eta$  is the overall efficiency of the driving system,  $t_s$  is sampling time,  $Q_{in} = [Q_{in1}, \dots, Q_{inN}]$  is acquired from file which is recorded on the real system and  $M'_L$  [kg/m] =  $\gamma \cdot Q_{in} / (3,6 \cdot v)$  is mass of material per unit of belt length. The results of measurements of the implemented algorithm with FLC, which are presented in Fig. 14, are recorded for the same values of input variable  $Q_{in}$ . The solution of the optimization problem is the optimum speed  $v_{opt} = [v_{opt1}, \dots, v_{optN}]$  for the given value of the input capacity of material, which provides the operation of BC with minimum energy consumption, i.e. with maximum energy efficiency under defined linear and nonlinear constraints. The minimum and maximum speed of the belt, as well as minimum and maximum time derivative of the belt speed present linear constrains, while maximum mass of material per unit of belt length presents nonlinear constraint.

The required solution is obtained by applying the *fmincon* function of MATLAB *Optimization Toolbox* [12], which finds a minimum of a constrained nonlinear multivariable function based on SQP algorithm (sequential quadratic programming).

In the considered case, constants  $\eta$ ,  $T_{max} = \gamma \cdot Q_{max}$  and  $M'_{Lmax}$  are the actual values of the analyzed system of BCs. The lower limit of belt speed is set on 60% of  $v_r$ , while the upper limit is set to 100% of  $v_r$ . Sampling rate for the input variable  $Q_{in}$  is  $t_s = 1$  s. Maximum values for acceleration and deceleration coefficients are equal and set to  $3.3[\%] \cdot v_r / t_s$ , in accordance with recommendations given in [3]. The result for the optimum speed obtained as the solution of the described optimization problem,  $v_{opt}$ , is in excellent agreement with the result of measurement for the fuzzy speed control of BC,  $v_{ref}$ , as presented in Fig. 17.

Presented time diagrams also confirm that the variable deceleration in the case of fuzzy speed control does not exceed the maximum value and satisfies all three defined requirements. Therefore, it is proved that the proposed

algorithm with FLC - case B provides operation with minimum energy consumption, in the existing operating conditions and under defined system constraints.

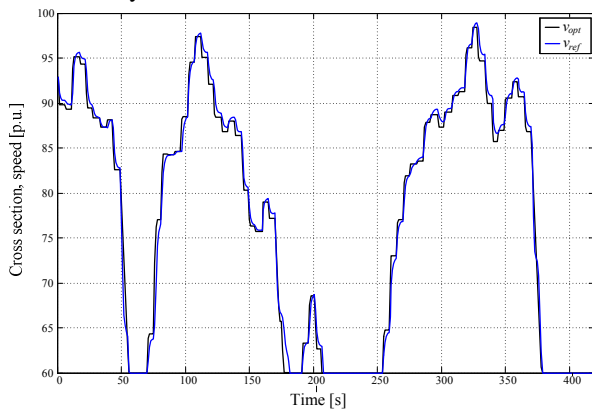


Fig. 17. Reference speed obtained with algorithm with FLC - CASE B,  $v_{ref}$ , together with optimum speed obtained with  $fmincon$  function,  $v_{opt}$ .

#### IV. CONCLUSION

The paper presents development of the algorithm for generating reference speed of the system of belt conveyors with adjustable speed induction motor drives based on a principle of optimum energy consumption. Three algorithms are presented. Two of them are generating the reference speed based on fuzzy logic control. All of them are tested on the detailed mathematical model of the belt conveyor. The algorithm based on fuzzy logic control which incorporates drive torque as the input variable is implemented on the new belt conveyor system at OPM. The displayed results of energy consumption during eight months of exploitation validate the applied control strategy. It is also confirmed analytically, through a method based on the sequential quadratic programming for finding the minimum of the nonlinear function of multiple variables under given constraints. Considering the indicated advantages of the proposed algorithm, as well as the proven opportunity of its successful implementation, the authors of the paper are expecting that their solution will be applied on similar systems in our country, as well as abroad. They certainly hope that their contribution will reduce the energy consumption and improve the efficiency of the mining process.

#### APPENDIX

##### Motor data:

Operating voltage: 690 V;  
Winding connection:  $\Delta$ ;  
Power: 1000kW / 995rpm;  
Duty: S1, ED 100%;  
Efficiency: 96.50%; Power factor: 0.837;  
Current: 1036 A; Torque: 9600Nm

##### BC data:

Belt width 2000mm; Number of drives 4;  
Type of drives: frequency converter with DTC;  
Maximum length 3.25km; Rated speed 4.65 m/s;  
Rated capacity of 6600m<sup>3</sup>/h

##### System of BCs data:

Number of belt conveyors: 5;  
Total installed power 20 MW;  
Current length: 7.5 km..

#### REFERENCES

- [1] W. Daus, *et al.*, "Raw Coal Loading and Belt Conveyer System at the Nochten Opencast Mine," *Braunkohle Surface Mining*, vol. 50, p. 12, 1998.
- [2] S. Zhang and X. Xia, "Modeling and energy efficiency optimization of belt conveyors," *Applied Energy*, vol. 88, p. 11, 2011.
- [3] Y. Pang and G. Lodewijks, "Improving energy efficiency in material transport systems by fuzzy speed control," in *Logistics and Industrial Informatics (LINDI), 2011 3rd IEEE International Symposium on*, 2011, pp. 159-164.
- [4] B. Jeftenić, *et al.*, "Energy efficiency in transportation of bulk material with frequency controlled drives," in *14th International Power Electronics and Motion Control Conference EPE-PEMC 2010*, Ohrid, Macedonia, 2010, pp. T5 105-113.
- [5] A. G. Tapp, "Energy Saving Troughing Idler Technology," *Bulk solids handling*, vol. 20, pp. 437-449, 2000.
- [6] B. T. Ralf, *et al.*, "Energy efficiency in opencast mine production systems," *Surface Mining - Braunkohle and other Minerals*, vol. 61, p. 8, 2009.
- [7] L. B. Ristić and B. I. Jeftenić, "Implementation of Fuzzy Control to Improve Energy Efficiency of Variable Speed Bulk Material Transportation," *IEEE Transactions on Industrial Electronics*, vol. 59, pp. 2959-2969, 2012.
- [8] B. Jeftenić, *et al.*, "Design and Selection of Belt Conveying Equipment & Systems," in *Design and Selection of Bulk Material Handling Equipment and Systems : Mining, Mineral Processing, Port, Plant and Excavation Engineering*. vol. I, J. Bhattacharya, Ed., I ed Kolkata: Wide Publishing, 2012, p. 254.
- [9] S. S.N., *et al.*, *Introduction to Fuzzy Logic using MATLAB*: Springer, 2007.
- [10] B. Jeftenić, *et al.*, "Optimal Utilization of the Bulk Material Transportation System based on Speed Controlled Drives," in *The XIX International Conference on Electrical Machines ICEM 2010*, Rome, Italy, 2010, pp. 1-6.
- [11] *Fuzzy Controllers- Recent Advances in Theory and Applications*, Sohail Iqbal, Nora Boumella and Juan Carlos Figueroa Garcia ed.: InTech, 2012.
- [12] *Optimization Toolbox User's Guide For Use with MATLAB, Version 2*. Available: www.mathworks.com

# An Efficient Method for Approximation of Non-Rational Transfer Functions

Tomislav B. Šekara, Milan R. Rapaić, and Mihailo P. Lazarević

**Abstract**—A method for rational approximation of linear fractional order systems (LFOS) is presented in the present paper. The method is computationally efficient, flexible and effective, as is illustrated by numerous examples. The proposed approach can also be used as an intermediate stage in designing indirect discrete rational approximations.

**Index Terms**—Discretization, fractional order systems, rational approximations.

*Original Research Paper*  
DOI: 10.7251/ELS1317040S

## I. INTRODUCTION

DESIGNING classical and/or fractional order control laws involving integral and differential actions [1, 2] often requires formulation of a discrete model of the process by using methods of invariable response to a pulse or Heaviside excitation and a series of other approximate methods [3-20]. Since a process can, in general, be represented by a transfer function  $G_p(s)$  which is not a rational function [21, 22], the problem of rational approximation and discretization in general becomes complex. In addition, the fundamental system properties, such as steady-state gain and settling time, as well as basic properties in the frequency domain, must be preserved. In the process of discretization of LFOS, where, in general, fractional order integral and differential actions belong, one can make use of the well-known mapping of  $s$ -domain to  $z$ -domain in the complex plane

$$z = e^{sT}, \quad (1)$$

where  $T$  is the sampling time. Transform (1) maps left half-plane of the  $s$ -plane to interior of the unity circle in the  $z$ -plane. This means that stability of the discrete system has been preserved if all poles of the discrete system are located within the unity circle. One of the basic goals of discretization

is acquiring the ability for practical realization of the corresponding control laws or of some other requirements in order that the digital model is fully equivalent to the continuous system over a wide frequency range.

The method proposed within the present paper relies on the interpolation of the frequency characteristic of the system on a predefined set of target frequencies. The approach has originally been proposed in [25]. The present manuscript extends the development of [25] by suggesting the possibility of using least-squares approximation on a wider frequency range.

For the purpose of illustration of practical importance of LFOS, consider a process described by classical diffusion equation (also referred to as the heat equation), which is ubiquitous in science and engineering since it simultaneously describes a number of transfer phenomena, including heat-transfer and a number of other diffusion-like processes. These diffusion-like processes include diffusion of mass (mechanical diffusion), diffusion of momentum (viscosity), diffusion of electrical potential (in long lines, when inductivity is negligible), and many others. One-dimensional diffusion equation is a partial differential equation of the form

$$\tau \frac{\partial^2 \rho}{\partial z^2} = \frac{\partial \rho}{\partial t}, \quad \tau > 0 \quad (2)$$

describing the process of transport (diffusion) of a quantity  $\rho$  along the  $z$  axis in time  $t$ . For simplicity, let us address only the diffusion within a semi-infinite medium, where both space and time variable take arbitrary positive values. Let us assume also that the process can be controlled by acting on the cross-section  $z = 0$ , and that the process output is taken (measured) at the cross-section  $z = L$ . The dynamics of the process is influenced by the diffusion time constant  $\tau = \tau(z, t)$ , which is, in general, a function of both space and time. However, in a variety of practically interesting cases this coefficient can be approximated by a constant factor.

Without loss of generality, assume that (2) describes a heat conduction process schematically shown in Fig. 1. Let us obtain its transfer function. In this particular case,  $\rho = \rho(z, t)$ , is the temperature of the cross section defined by space coordinate  $z$  evaluated at time instant  $t$ . Let  $\tilde{\rho} = \tilde{\rho}(z, s)$  denote the Laplace transform of  $\rho$ , where the Laplace transform is taken with respect to the time variable  $t$  and the space variable  $z$  is considered as a parameter,

Manuscript received 19 April 2013. Accepted for publication 8 May 2013.

The authors would like to gratefully acknowledge the financial support of Serbian Ministry of Science and Education, under grants TR33020 (T.B.Š), TR32018 and TR33013 (M.R.R) and III41006 (M.P.L.).

T. B. Šekara is with the Faculty of Electrical Engineering, University of Belgrade, Belgrade, Serbia (e-mail: tomi@etf.rs).

M. R. Rapaić is with Faculty of Technical Sciences, University of Novi Sad, Novi Sad, Serbia. (tel: +381621711982, e-mail: rapaja@uns.ac.rs).

M. P. Lazarević is with the Faculty of Mechanical Engineering, University of Belgrade, Belgrade, Serbia (e-mail: mlazarevic@mas.bg.ac.rs).

$$\tilde{\rho}(z, s) = \int_0^{\infty} \rho(z, t) e^{-st} dt. \quad (3)$$

By applying the Laplace transform to equation (2), one obtains general solution

$$\tilde{\rho}(s, z) = C_1(s) e^{-z\sqrt{s/\tau}} + C_2(s) e^{z\sqrt{s/\tau}}. \quad (4)$$

Since any heat conduction process is stable, the Laplace transform of the temperature in any cross-section must be bounded, i.e.

$$\lim_{z \rightarrow \infty} \tilde{\rho}(s, z) = \text{const.} \quad (5)$$

has to be satisfied, thus  $C_2=0$  and equation (4) takes the form

$$\tilde{\rho}(s, z) = C_1(s) e^{-z\sqrt{s/\tau}}. \quad (6)$$

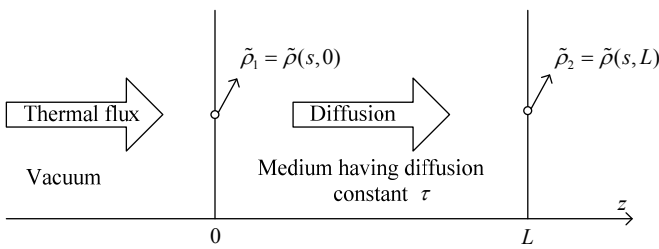


Fig. 1. A sketch of the process of heat conduction by diffusion.

Integration “constant”  $C_1$  as well as the conduction function is determined from the known (or given) boundary conditions. In view of this, the most frequent cases in practice are:

**Case 1.** Heat conduction without any convective exchange of heat with the environment and fixed temperature at the “left” boundary. In this particular case, the temperature of the cross-section  $z=0$  could be controlled directly, and considered as the input of the process, while the dependent temperature of the cross-section  $z=L$  could be considered as the output. The left boundary condition for this case is  $\tilde{\rho}(s, 0) = C_1(s)$ , and the transfer function takes the form

$$G_a(s) = \frac{\tilde{\rho}_2(s, L)}{\tilde{\rho}_1(s, 0)} = e^{-L\sqrt{s/\tau}} = e^{-\sqrt{T}s}, \quad T = L^2 / \tau. \quad (7)$$

**Case 2.** Heat conduction without any convective exchange of heat with the environment and fixed thermal flux at the “left” boundary. The process is influenced by gradient of quantity  $\rho$  at  $z=0$  (this is the boundary surface of the medium of Fig. 1), the input quantity of the process being thermal flux through the boundary surface (again without any convective exchange with the environment)

$$\psi = -\lambda \left. \frac{d\tilde{\rho}(s, z)}{dz} \right|_{z=0} \quad (8)$$

and the process (output) quantity is  $\rho_2 = \rho(s, L)$ , and the transfer function is

$$G_b(s) = \frac{\tilde{\rho}_2}{\psi} = \frac{K}{\sqrt{s}} e^{-\sqrt{T}s}, \quad T = L^2 / \tau, \quad K = \sqrt{\tau} / \lambda. \quad (9)$$

**Case 3.** Heat conduction without any convective exchange of heat with the environment. The last characteristic case is when the convection is no longer neglected. Now, the process is influenced by a linear combination of the thermal flux and temperature at the “left” boundary

$$u = -\lambda \left. \frac{d\tilde{\rho}(s, z)}{dz} \right|_{z=0} + \eta \tilde{\rho}(s, z), \quad (10)$$

with output  $\rho_2 = \rho(s, L)$ , and the transfer function is

$$G_c(s) = \frac{\tilde{\rho}_2}{u} = \frac{K}{1 + \sqrt{T_1 s}} e^{-\sqrt{T}s}, \quad K = \frac{1}{\eta}, \quad T_1 = \frac{\lambda^2}{\eta^2 \tau}, \quad T = \frac{L^2}{\tau}. \quad (11)$$

In the examples above, the semi-derivative operator has appeared in a number of contexts. It should be mentioned that other forms of fractional order transfer functions emerge during investigations of different transfer phenomena. In the analysis of axial diffusion, i.e. diffusion from the axis of the cylinder towards its lateral surface or vice versa, one meets transfer functions originating from the Laplace transforms of Bessel functions, which have the form

$$G(s) = \frac{K}{\sqrt{1 + sT}} \quad (12)$$

From this example, transfer functions given by equations (7), (9), (11), and (12) belong to the fractional order systems having transfer functions which belong to the class of irrational functions [23,24].

Since these transfer functions describe adequately physical processes, a logical question arises whether it is possible to formulate fractional order control laws and what would be their contribution to process control. Among many modern control strategies utilizing fractional order calculus, Podlubny’s Fractional order PID [1,2] regulator is emphasized here. Classical PID is arguably the most utilized control strategy in use today. By replacing classical integral and differential actions by their respective fractional order analogues, the flexibility and applicability of the PID regulator can be greatly increased. Transfer function of the fractional order PID is of the form

$$\text{PI}^\lambda \text{D}^\mu(s) = k + k_i s^{-\lambda} + k_d s^\mu, \quad \lambda, \mu \in [0, 1]. \quad (13)$$

The reader should notice that the implementation of Fractional order PID requires direct implementation of fractional order integrator and differentiator. Similar is also true for other

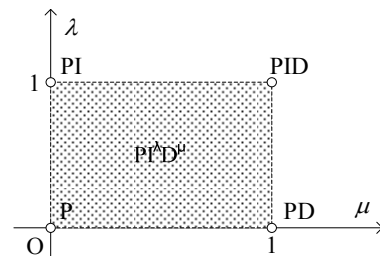


Fig. 2. A sketch of the process of heat conduction by diffusion.

types of fractional order regulators, as it can be seen from [25-27]. Such regulators are typically implemented as high order FIR or IIR filters [28], Realization of fractional order control laws involving an adequate discretization is possible thanks to the fast modern computers. It is known that in the regulator design two approaches are possible, direct design in the discrete domain and the other approach is design in the continuous domain first and then transition to the discrete domain. Obviously, discretization is required by both approaches. However, the discretization procedure is not straightforward when fractional order systems are in question, a problem which has been causing a considerable interest over the past years.

The paper is organized as follows. In the following Section II the proposed method for rational approximation of FOS has been outlined. Numerical examples are presented in Section III. Concluding remarks are presented in Section IV.

## II. RATIONAL APPROXIMATIONS OF TRANSFER FUNCTIONS OF LFOS

Let us consider rational transfer function

$$\frac{B(s)}{A(s)} = \frac{b_{n-1}s^{n-1} + \dots + b_1s + b_0}{a_n s^n + a_{n-1}s^{n-1} + \dots + a_1s + a_0} \quad (14)$$

which should be used to approximate transfer function  $G(s)$  of a linear fractional order system. For  $(G(0) \neq 0, b_0=1)$  or  $(G(0)=0, a_0=1)$  there are  $2n$  real coefficients which should be determined from  $2n$  equations obtained from the condition of overlapping the frequency characteristics in the corresponding discrete frequency points  $\omega \in [\omega_0, \omega_2, \dots, \omega_{n-1}]$ , i.e.

$$G(i\omega_k) - B(i\omega_k)/A(i\omega_k) = 0, \quad k = \overline{0, n-1}, \quad i = \sqrt{-1}, \quad (15)$$

or for  $G(0) \neq 0, b_0=1$  one obtains

$$\operatorname{Re}(G(i\omega_k)A(i\omega_k) - B(i\omega_k)) = 0, \quad k = \overline{0, n-1}, \quad (16)$$

$$\operatorname{Im}(G(i\omega_k)A(i\omega_k) - B(i\omega_k)) = 0, \quad k = \overline{0, n-1}. \quad (17)$$

Note that  $G(i\omega_k)$  is a constant complex number for any fixed  $\omega_k$ . For fixed  $\omega_k$  both numerator and denominator polynomials are linear combinations of the unknown process parameters. Thus, the set of equations (16), (17) represents a linear system of equations having  $2n$  unknown coefficients. By solving this system of  $2n$  linear equations, one obtains  $2n$  coefficients of rational approximation (14).

It is convenient to represent this system of equations in the matrix form. This form is particularly suitable for the numerical evaluation of the unknown coefficients. Consider equations (16) and (17). Assuming the case  $G(0)=0, a_0=1$  (other cases can be dealt in the similar fashion), for any  $k = \overline{0, n-1}$  one obtains

$$G(i\omega_k)(a_n(i\omega_k)^n + \dots + a_1i\omega_k + 1) - b_{n-1}(i\omega_k)^{n-1} - \dots - b_0 = 0,$$

or, introducing

$$R_{n,k} = \operatorname{Re}\{(i\omega_k)^n\}, \quad I_{n,k} = \operatorname{Im}\{(i\omega_k)^n\}, \\ GR_{n,k} = \operatorname{Re}\{G(i\omega_k)(i\omega_k)^n\}, \quad GI_{n,k} = \operatorname{Im}\{G(i\omega_k)(i\omega_k)^n\},$$

one obtains

$$a_n GR_{n,k} + \dots + a_1 GR_{1,k} - b_{n-1} R_{n-1,k} - \dots - b_0 R_{0,k} = -GR_{0,k} \quad (18)$$

$$a_n GI_{n,k} + \dots + a_1 GI_{1,k} - b_{n-1} I_{n-1,k} - \dots - b_0 I_{0,k} = -GI_{0,k} \quad (19)$$

The obtained equations are conveniently rewritten in the following matrix form, which is easily solved using some of the modern computer algebra packages, in particular, introducing

$$\mathbf{M} = \begin{bmatrix} GR_{n,0} & \dots & GR_{1,0} & -R_{n-1,0} & \dots & -R_{0,0} \\ \vdots & \ddots & \vdots & \vdots & \ddots & \vdots \\ GR_{n,n-1} & \dots & GR_{1,n-1} & -R_{n-1,n-1} & \dots & -R_{0,n-1} \\ GI_{n,0} & \dots & GI_{1,0} & -I_{n-1,0} & \dots & -I_{0,0} \\ \vdots & \ddots & \vdots & \vdots & \ddots & \vdots \\ GI_{n,n-1} & \dots & GI_{1,n-1} & -I_{n-1,n-1} & \dots & -I_{0,n-1} \end{bmatrix},$$

$$\mathbf{b} = \begin{bmatrix} GR_{0,0} \\ \vdots \\ GR_{0,n-1} \\ GI_{0,0} \\ \vdots \\ GI_{0,n-1} \end{bmatrix},$$

one easily obtains the desired system of linear equations in matrix form

$$\mathbf{M}\mathbf{x} = \mathbf{b}, \quad (20)$$

where  $\mathbf{x}$  is the vector of unknown parameters,

$$\mathbf{x} = \begin{bmatrix} a_{n-1} \\ \vdots \\ a_1 \\ b_{n-1} \\ \vdots \\ b_0 \end{bmatrix}.$$

It is important to mention that the selected set of points  $\omega \in [\omega_0, \omega_2, \dots, \omega_{n-1}]$  can produce a singular matrix of the set of equations (16), (17). In such a case, another, more appropriate set of points should be used. It is also significant to note that it is also possible to use more than  $n$  incident points in the selected set. The exact solution cannot be found in such a case. However, the best approximation, in the least-squares sense, can be found by means of pseudo-inversion.

## III. NUMERICAL EXAMPLES

Let us select several LFOS transfer functions and compare their Bode characteristics and responses to Heaviside excitation with those of the corresponding rational approximations determined on the basis of the set of linear equations (16) and (17). The exact characteristics are shown in blue line, while the approximations are plotted in red. For

each of the examples considered below, a set of target frequency values used in (16) and (17) has been specified also.

*Example 1.* Consider fractional order system described by transfer function  $G_1(s) = 1/(s^{3/2} + 1)$ , and consider its rational approximation obtained by interpolating frequency response in target points  $\omega \in [0.01, 0.1, 0.5, 1, 5, 10, 100]$ .

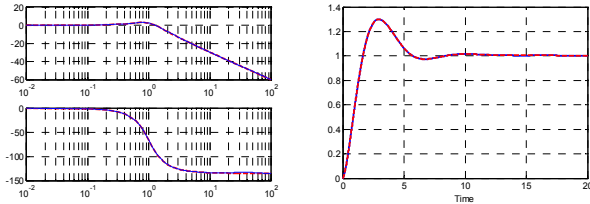


Fig 3. Frequency and time responses  $G_1(s)$  (red) and  $B_1(s)/A_1(s)$  (blue).

*Example 2.* Consider the fractional oscillator characterized by a strong resonant peak at unit angular frequency,  $G_2(s) = 1/(s - \sqrt{2}s + 1)$ , with  $\omega \in [0.01, 0.1, 0.5, 1, 5, 10, 100]$ .

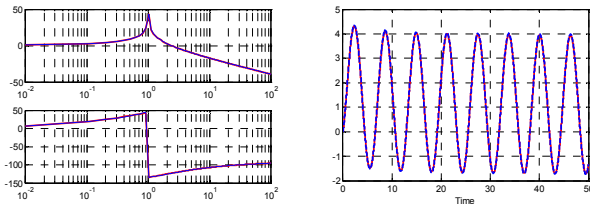


Fig 4. Frequency and time responses  $G_2(s)$  (red) and  $B_2(s)/A_2(s)$  (blue).

*Example 3.* Consider a process with  $G_3(s) = \exp(-\sqrt{s})$ .

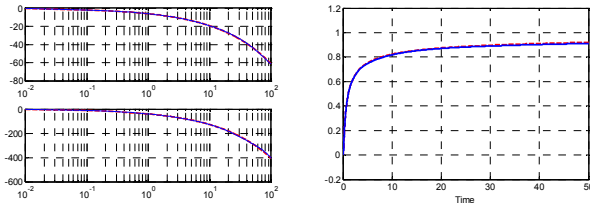


Fig 5. Frequency and time responses  $G_3(s)$  (red) I  $B_3(s)/A_3(s)$  (blue).

Processes with such a transfer function are common in analysis of distributed parameter systems, particularly those involving heat and mass transfer; see for example [22, 23]. Similar phenomena are, in a generalized form, also studied in [21].

*Example 4.* Fractional logarithmic filter with transfer function  $G_4(s) = \ln(s)/s$  appears in the study of adaptive fractional systems, as can be seen from [24]. The incident frequencies in this particular case where  $\omega \in [0.001, 0.01, 0.1, 0.5, 1, 5, 50]$ .

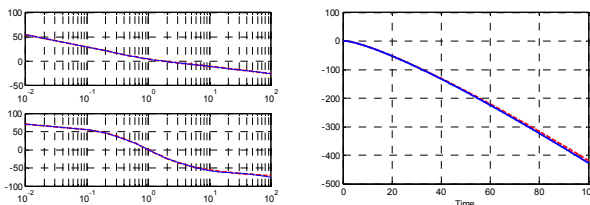


Fig 6. Frequency and time responses  $G_3(s)$  (red) i  $B_3(s)/A_3(s)$  (blue).

*Example 5.* The following example demonstrates a case when the process output is equal to the fractional semi-integral of a IIR filtered input. The actual IIR filter is, in fact, a differential compensator.  $G_5(s) = \left(\frac{s+1}{0.1s+1}\right)^{0.5}$ ,  $\omega \in [0.01, 0.1, 1, 3, 5, 10, 100]$ .

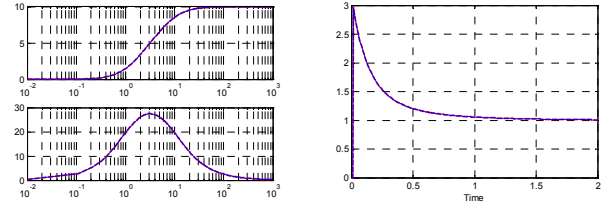


Fig 7. Frequency and time responses  $G_5(s)$  (red) i  $B_5(s)/A_5(s)$  (blue).

*Example 6.*  $G_6(s) = (1 + 1/s + s^{1.2}) / (0.1s + 1)^{1.2}$ ,  $\omega \in [0.5, 0.8, 1, 2, 5, 30, 100]$ .

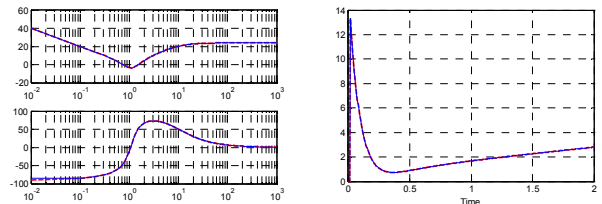


Fig 8. Frequency and time responses  $G_6(s)$  (red) i  $B_6(s)/A_6(s)$  (blue).

As the previous figures show, the rational approximations give adequate approximations for a wide range of LFOS. It should especially be mentioned that the corresponding frequency points are selected on the basis of the knowledge of Bode characteristics of LFOS transfer functions. In all previous examples the selected order  $n = 7$  obviously can be lower, but under condition that the frequency characteristics in the selected frequency range are not violated. Also, for the selected set of frequencies in all these examples, the matrices of the sets of equations (16), (17) have been regular.

Obviously, since a rational transfer function is in question, applications of all techniques of discretization are possible, consequently adequate discrete models of LSF transfer functions within certain frequency range are available.

All of the time-domain responses presented above are obtained by means of direct integration in the complex domain. The interested reader is referred to [14].

#### IV. CONCLUSIONS

Owing to simplicity of application of the method of rational approximation of transfer functions of linear fractional order systems, this paper is dedicated to an analysis of the application of this approach for the purpose of discretization of linear fractional order systems. It should be emphasized that, since a rational transfer function of a continuous system is in question, application of all techniques of its discretization are possible, i.e. for discretization of linear fractional systems.

The most outstanding feature of the proposed method is its computational efficiency. The method is, in fact, very simple both conceptually and computationally. The obtained results are, as it can be seen from the previous examples quite satisfactory. The main drawback of the proposed method is that it is not possible to guarantee stability *a priori*, in other words no constraints on the coefficients are enforced. Indeed, the form of these constraints would be so complex, that their introduction would impair the established efficiency of the solution presented in the current paper.

A possible solution to this problem is to use the obtained coefficients as the initial guess for the more elaborate, non-convex optimization procedure. Such an approach would lose the desired computational efficiency, but would be able to give stronger stability guarantees.

#### REFERENCES

- [1] I. Podlubny, Fractional Differential Equations, Academic Press, London, 1999.
- [2] I. Podlubny, Fractional-Order Systems and  $P^I D^\mu$  Controllers, IEEE Transaction on Automatic Control, vol. 44, 1999, pp. 208–214.
- [3] R. Boxer, A Simplified Method of Solving Linear and Nonlinear Systems, Proceedings of the IRE, vol. 44, 1956, pp. 89-101.
- [4] R. Boxer, A Note on Numerical Transform Calculus, Proceedings of the IRE, vol. 43, 1957, pp. 228-229.
- [5] K. J. Åström, P. Hagander, J. Sternby, Zeros of sampled systems, IEEE Automatica vol. 20, 1984, pp. 31-38.
- [6] K. J. Åström, B. Wittenmark, Computer Controlled Systems: Theory and Design, 3. ed., Prentice-Hall, 1997.
- [7] M. R. Rapačić, T. B. Šekara, Novel direct optimal and indirect method for discretization of linear fractional systems, Electrical Engineering, vol 93, 2011, pp. 91-102.
- [8] J. M. Smith, Mathematical Modeling and Digital Simulation for Engineers and Scientists, 2. ed., Wiley, New York, 1987.
- [9] T. Šekara, New Transformation Polynomials for Discretization of Analogue Systems, Electrical Engineering, vol. 89, 2005, pp. 137-147.  
T. B. Šekara, M. R. Stojić, Application of the  $\alpha$ -approximation for discretization of analogue systems, Facta Universitatis, Ser: Elec. Energ vol. 3, pp. 571-586, 2005. <http://factaee.elfak.ni.ac.yu/fu2k53/Šekara.pdf>
- [10] T. B. Šekara, L. S. Draganović, M. S. Stanković, Novel Approximations for Discretization of Continuous Systems, In: Proceedings of the XLVI ETRAN Conference, vol. 1, Bosnia and Herzegovina, 2002, pp 220-223 (in Serbian).
- [11] T. B. Šekara, M. S. Stanković, Novel Transformation Polynomials for Discretization of Continuous Systems. In: Proc. of XLVII ETRAN Conference, vol. 1, 2003, pp. 247-250, Montenegro (in Serbian).
- [12] T. B. Šekara, Indirect application of transformation polynomials for discretization of fractional integrators (differentiators). In: Proc. of XLIII ETRAN Conference, vol.1, 2005, pp.234-237. Montenegro, (in. Serb.)
- [13] T. B. Šekara, Fractional Transformations with Applications to Control Systems and Electrical Circuits. PhD Thesis, Faculty of Electrical Engineering, University of Belgrade (in Serbian), 2006.
- [14] T. Dostál, J. Pospíšil, Switched circuits I, Rersearch Report No. FE-58, Department of Radioelectronics, TU Brno, 1985.
- [15] G. Zhang, X. Chen, T. Chen, Digital Redesign via Generalized Bilinear Transform, International Journal of Control, vol. 82, 2009, pp. 741-754.
- [16] K. Zaplatilek, M. Lares Efficient Algorithms of Direct and Inverse First-Order s-z Transformations. Radioengineering, vol. 10, 2001, pp. 6-10.
- [17] Y. Choo, Computing Transformation Matrix for Bilinear s-z Transformation. IEICE Trans. Fundam., vol. E90-A, 2007, pp. 872-874.
- [18] E. W. Bai, Z. Ding, Zeros of sampled data systems represented by FIR models, Automatica, vol. 36, 2000, pp. 121-123.
- [19] J. Le Bihan, Novel Class of Digital Integrators and Differentiators, Electronic Letters, vol. 29, 1993, pp. 971–973.
- [20] Milan R. Rapačić, Optimalno i suboptimalno upravljanje klasom sistema sa raspodeljenim parametrima, doktorska disertacija, Fakultet tehničkih nauka, Novi Sad, 2011
- [21] Joel L. Schif, The Laplace transform – Theory and applications, Springer 1999
- [22] Tomislav B. Šekara, Frakcioni sistemi upravljanja, Akademska misao, 2011
- [23] Milan R. Rapačić, Alessandro Pisano, Adaptive on-line estimation of the commensurate order in fractional systems, The 5th IFAC, Nanjing, China, May 2012
- [24] Tomislav B. Šekara, Milan R. Rapačić, Mihailo P. Lazarević, Indirect application of a method for discretization of linear fractional order systems, INDEL 2012.

# Influence of Signal Stationarity on Digital Stochastic Measurement Implementation

Platon Sovilj, Vladimir Vujičić, Nebojša Pjevalica, Dragan Pejić, Marjan Urekar, and Ivan Župunski

**Abstract**—The paper presents the influence of signal stationarity on digital stochastic measurement method implementation. The implementation method is based on stochastic voltage generators, analog adders, low resolution A/D converter, and multipliers and accumulators implemented by Field-Programmable Gate Array (FPGA). The characteristic of first implementations of digital stochastic measurement was the measurement of stationary signal harmonics over the constant measurement period. Later, digital stochastic measurement was extended and used also when it was necessary to measure time-series of non-stationary signal over the variable measurement time. The result of measurement is the set of harmonics, which is, in the case of non-stationary signals, the input for calculating digital values of signal in time domain. A theoretical approach to determine measurement uncertainty is presented and the accuracy trends with varying signal-to-noise ratio (SNR) are analyzed. Noisy brain potentials (spontaneous and non-spontaneous) are selected as an example of real non-stationary signal and its digital stochastic measurement is tested by simulations and experiments. Tests were performed without noise and with adding noise with SNR values of 10dB, 0dB and -10dB. The results of simulations and experiments are compared versus theory calculations, and comparison confirms the theory.

**Index Terms**—Digital measurements, stochastic measurements, measurement uncertainty, brain potentials.

Original Research Paper  
DOI: 10.7251/ELS1317045S

## NOMENCLATURE

$s$  – noisy signal measured after conditioning  
 $s_e$  – amplified input signal  
 $n$  – noise in signal at the input of digital block  
 $s_a$  – auxiliary signal (dithered base function)  
 $S_a$  – the root mean square (RMS) value of the auxiliary signal  
 $d_i$  – dithering signal  
 $p(d_i)$  – probability density function of  $d_i$  dithering signal  
 $\Delta_i$  – quantum of the uniform quantizer

$p(n)$  – probability density function of noise  $n$   
 $T$  – measurement subinterval  
 $f_0$  – fundamental frequency  
 $f_{adc}$  – sampling frequency of analog-to-digital (A/D) converter in digital stochastic measurement block  
 $R$  – input range  
 $N$  – number of samples within measurement subinterval  
 $N_h$  – number of harmonics measured by digital stochastic measurement block  
 $\Psi_e$  – result of A/D conversion of dithered signal  $s$   
 $\Psi_a$  – result of A/D conversion of dithered base function  
 $\Psi_{acosk}$  – result of A/D conversion of dithered cosine function with period  $\omega = 2\pi kf_0$   
 $\Psi_{asink}$  – result of A/D conversion of dithered sine function with period  $\omega = 2\pi kf_0$   
 $\Psi$  – digital multiplier output  
 $\Psi_{cosk}$  – digital multiplier output for measuring cosine component of  $k$ th harmonic  
 $\Psi_{sink}$  – digital multiplier output for measuring sine component of  $k$ th harmonic  
 $a_k$  – cosine Fourier coefficient of  $k$ th harmonic i.e. trigonometric polynomial cosine coefficient of order  $k$   
 $b_k$  – sine Fourier coefficient of  $k$ th harmonic i.e. trigonometric polynomial sine coefficient of order  $k$   
 $u(\Psi)$  – standard measurement uncertainty  
 $u$  – relative measurement uncertainty  
 $\sigma_\Psi^2$  – variance of digital multiplier output  
 $\sigma_d^2$  – deterministic variance  
 $\sigma_n^2$  – noise variance  
 $\sigma_r^2$  – random variance (noise induced)  
 $\sigma_e^2$  – variance due to quantization error and dither

## I. INTRODUCTION

ALL signals can be divided into either stationary or non-stationary categories. Non-stationary signals are not constant in their statistical parameters over time (i.e. its amplitude distribution and standard deviation are not the same over time). Stationary signals are constant in their statistical parameters over time. Stationary signals further can be divided into deterministic and random signals. Random signals are unpredictable in their frequency content and their amplitude level, but they still have relatively uniform statistical characteristics over time [1-2].

Advanced measurement instrumentation is based on digitizing hardware components. Measured signals are usually

Manuscript received 15 April 2013. Received in revised form 12 June 2013. Accepted for publication 13 June 2013.

This work was supported in part by the Ministry of Science and Technological Development of Republic of Serbia under research grant No. TR32019, and supported in part by the Provincial secretariat for science and technological development of Autonomous Province of Vojvodina (Republic of Serbia) under research grant No. 114-451-2723.

The authors are with the Faculty of Technical Sciences, University of Novi Sad, Novi Sad, Serbia (Corresponding author e-mail: platon@uns.ac.rs).

conditioned and time-continuous conditioned signals are sampled and converted into discrete digital variables. In the A/D conversion process, accuracy and speed are opposing requirements, and accurate measurements of low-level, noisy and distorted signals have been a challenging problem in the theory and practice of measurement science and technology.

A possibility for reliable operation of instruments with inherent random error has been researched since 1956 [3]. An inherent property of such an approach is a very simple hardware, which can operate very fast. It has been shown that adding a random uniform dither to an A/D converter input decouples measurement error from the input signal [4]. This dither also suppresses the measurement error due to both coarse A/D conversion and the external additive noise in the input signal.

Following this generic approach, several specific methods has been developed for measuring average DC inputs, AC inputs and/or distorted AC inputs. Several prototype and small-series commercial instruments has been realized and their measurement uncertainty can be extremely low [5-6]. These methods were named digital stochastic measurement methods and these instruments were named digital stochastic instruments.

The latest prototype instrument is a digital stochastic instrument for measurement of harmonics of mains voltage and current signals, reported in [7]. This instrument performs harmonic analyses for the DC component and up to 49 harmonics (both cosine and sine components) in each of seven different input channels. Its operation is based on stochastic A/D conversion and accumulation, with a hardware structure designed for harmonic measurements. The method and the predicted uncertainty for fifty harmonics are validated in [7] by simulation and experiments using sampling frequency of 250 kHz per channel.

In paper [8] digital stochastic measurement method is investigated for various types of stationary signal. The results demonstrated the ability of this method to be applied for measurements of harmonics of any stationary signal. After that, the question was if it was possible to extend the method for being used in measuring non-stationary signals? The research described in [9], lead to positive answer, so the method can be applied in measurement of biomedical signals, audio signals, video signals etc.

This paper describes the influence of signal stationarity on digital stochastic measurement implementation, and it is based on researching theoretical models of digital stochastic measurement of stationary and non-stationary signals and their consequences in the form of mathematical formulas, and on researching simulated measurement and real measurement of

brain potential as a non-stationary signal example.

## II. ANALYSYS OF METHOD

### A. Digital Stochastic Measurement and Signal Stationarity

Measurement system based on digital stochastic measurement can be divided into three blocks: conditioning block, digital stochastic measurement block and block for data processing, recording and presenting (Fig. 1).

The signal at the input of digital stochastic measurement block is the conditioned signal. The role of this conditioning can be amplification, linearization, level transition, filtering, galvanic isolation, various techniques for rejecting noise etc. In this paper the focus of analysis is the implementation of digital stochastic measurement, neglecting the non-linearity issues of the components consisting conditioning block. Hence, it is proposed that conditioned signal  $s$  is the sum of linearly amplified input signal  $s_e$  (which will be called just “amplified input signal” in further text) and the white noise  $n$  with uniform or Gaussian amplitude distribution:

$$s = s_e + n \quad (1)$$

Noise  $n$  is assumed to be the sum of all the noises which were not rejected before the digital stochastic measurement system. The sources of the noise can be the phenomenons inside the conditioning block, but also inside the conditioning block input interface, and inside the interface between conditioning block and digital stochastic measurement block. In this paper, we do not consider the nature of various noise sources and the phenomenons behind them, but focus on the general model of noise.

If short-time Fourier transform would be applied to signal  $s_e$  by window function of width equal to measurement subinterval  $T$ , resulting in Fourier coefficients  $a_i$  and  $b_i$ , then  $s_e$  can be presented as a trigonometric polynomial of the form:

$$s_e(t) = \frac{a_0}{2} + \sum_{n=1}^M a_n \cos n\omega_0 t + \sum_{n=1}^M b_n \sin n\omega_0 t, \quad 0 < t < T \quad (2)$$

In (2)  $\omega_0 = 2\pi/T$  and  $M$  is the order of trigonometric polynomial [7].

Concept of digital stochastic measurement compared with typical digital measurement is shown at Fig. 2. The outputs of digital measurement are digital values in time domain. Each digital value is actually digitized value of appropriate analog sample from the input and that is well known classical approach of digital measurement – sample by sample.

Instead of such approach, the outputs of digital stochastic measurement are Fourier coefficients  $a_i$  and  $b_i$ . Each Fourier coefficients is the function of all analog samples from the input over the measurement subinterval. Hence, this method is not based on “sample by sample” approach, but it is an

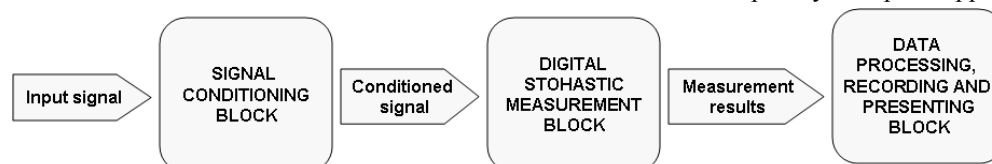


Fig. 1. Measurement system based on digital stochastic measurement.

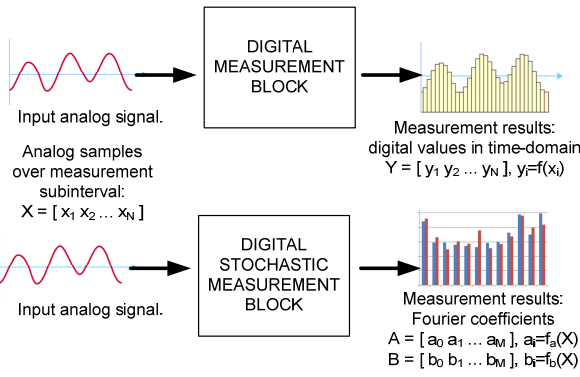


Fig. 2. Typical digital measurement versus digital stochastic measurement.

interval-based method.

At first sight it can be concluded that digital stochastic measurement is convenient only for measuring harmonics of stationary signals. But, it can be also used for measuring non-stationary signals. The result of measurement is the set of harmonics, which can be the input for calculating digital values of signal in time domain. This calculation can be simple the calculation of trigonometrial polynomial (2) at each time instant over the measurement subinterval  $T$ , or it can be Inverse Fast Fourier Transform (IFFT) over the measurement subinterval  $T$  which is faster method. Hence, the final results are a) the set of harmonics of the signal over the measurement subinterval  $T$  and b) time-series of the signal over the measurement subinterval  $T$  (Fig. 3).

This method has not to be limited to measurement subinterval  $T$ . If we want to measure the signal over the longer measurement interval  $[0, T_m]$ , where  $T_m = m \cdot T$ , than it is possible to divide original measurement interval to measurement subintervals  $[0, T]$ ,  $[T, 2T]$ , ...,  $[(m-1)T, mT]$ . Measurement and calculation can be executed for the first subinterval, and subsequently, subinterval by subinterval, signal values in time-domain can be reconstructed over the whole measurement interval  $[0, T_m]$ .

### B. Measurement of One Fourier Coefficient

The instrument presented in [7, 8] is designed to measure harmonics of mains voltages and currents, but its concept can be applied to measurement of harmonics of any signal that can be presented as (2). Therefore its concept is the base for conceptual block diagram of digital stochastic measurement of one Fourier coefficient of the amplified input signal. (Fig. 4)

Auxiliary signal  $s_a$  is a dithered base (cosine or sine) function. That is,  $s_a = R \cos k\omega_0 t$  for measuring  $k$ th cosine Fourier coefficient, or  $s_a = R \sin k\omega_0 t$  for measuring  $k$ th sine

Fourier coefficient.

Similarly to [7] the conceptual block diagram can be implemented as in Fig. 5 so  $s_a$  is not to be a measured signal, but a dithered sine or cosine function generated in advance and stored in the memory.

$d_1$  and  $d_2$  are generated dithering signals and they satisfy the following conditions that limit their amplitude and define their probability density function:

$$0 \leq |d_i| \leq \frac{\Delta_i}{2} \quad (3)$$

$$p(d_i) = \frac{1}{\Delta_i}, \text{ for } i = 1, 2 \quad (4)$$

Sampled values of conditioned signal  $s$  and auxiliary signal  $s_a$  at every time instant within the measurement subinterval ( $T$ ) are  $\psi_e$  and  $\psi_a$ , respectively. The measured value  $\psi$  (multiplier output) differs from the input signals' product by the measurement error  $e$ , which includes effect of quantization within A/D converter and the introduced dither:

$$\Psi = \Psi_e \cdot \Psi_a = s \cdot s_a + e \quad (5)$$

As the measured conditioned signal consists of the amplified input signal and the noise, then:

$$\Psi = s_e \cdot s_a + n \cdot s_a + e \quad (6)$$

The first term of the multiplier output is the signal that is to be measured and the second term is caused by noise. The three terms in (6) are statistically independent, and average  $\bar{\Psi}$  is the sum of their average values.

The average value of the third term in (6) is zero, as shown in [10] and does not affect the average value of the expected output  $\bar{\Psi}$  over the measurement subinterval. A finite input range of  $\pm R$  of digital stochastic measurement block defines the boundary of the average noise integration. Therefore the remaining two terms in the average value are [5]:

$$\bar{\Psi} = \frac{1}{T} \int_0^T s_e \cdot s_a dt + \left( \int_{-R}^R n \cdot p(n) dn \right) \frac{1}{T} \int_0^T s_a dt \quad (7)$$

If we assume that the noise has a Gaussian unbiased nature, its average value is zero so that the second term in (7) becomes zero, and then:

$$\bar{\Psi} = \frac{1}{T} \int_0^T s_e \cdot s_a dt. \quad (8)$$

In digital measurements, for  $N$  samples of the conditioned signal over the subinterval  $[0, T]$ , the average value is [7]:

$$\bar{\Psi} = \frac{1}{N} \sum_{k=1}^N \Psi_k \quad (9)$$

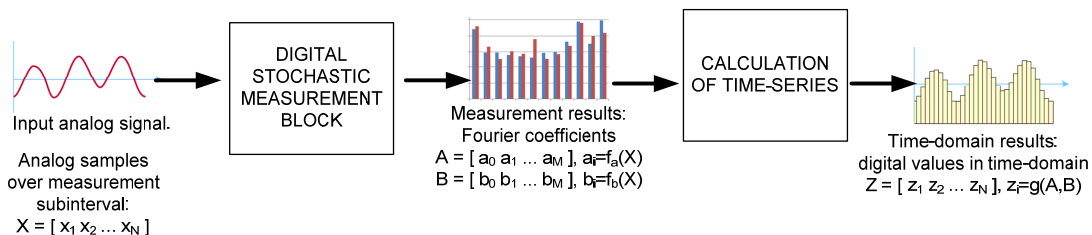


Fig. 3. Concept of measuring signal in time-domain by digital stochastic measurement over one measurement subinterval.

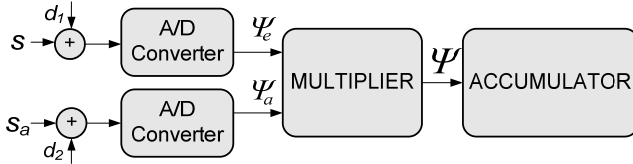


Fig. 4. Conceptual block diagram of digital stochastic measurement of one Fourier coefficient of amplified input signal. The accumulator output is used for calculation of the coefficient.

Summing of samples during the measurement subinterval is done by the accumulator and this sum is the output of the accumulator (Fig. 5). This output can be processed by microprocessor which divide the accumulator output by the number of samples  $N$ , and also calculates each sine (or cosine) component of the  $k$ th harmonic of the output as in [7] (subscripts  $sin k$  and  $cos k$  indicates that  $k$ th sine and  $k$ th cosine Fourier coefficient is measured) :

$$a_k = \frac{2\bar{\Psi}_{\cos k}}{R}, \quad b_k = \frac{2\bar{\Psi}_{\sin k}}{R} \quad (10)$$

### C. Measurement of Predefined Set of Harmonics

The concept of measuring one Fourier coefficient of the amplified input signal can be extended as in Fig. 6, which presents more complex conceptual block-diagram for measuring predefined set of harmonics of conditioned signal at the input of digital stochastic measurement block (DSMB). Beside DC component, predefined set can include all the harmonics which are interested for the signal analysis. Memory gives dithered base functions for each sine and

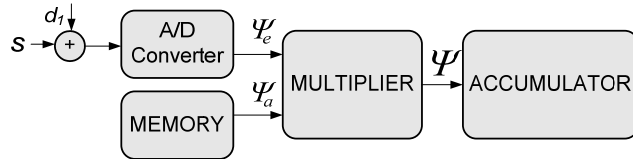


Fig. 5. Improved conceptual block diagram of digital stochastic measurement of one Fourier coefficient of amplified EEG signal. Instead of using two A/D converters, digital samples of the dithered base function are stored in memory.

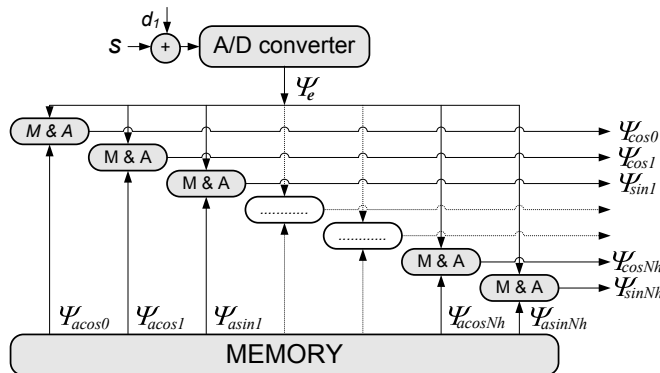


Fig. 6. Conceptual block diagram of digital stochastic measurement of predefined set of signal harmonics. Each element marked with M&A is consisted of one multiplier and one accumulator. Each output should be divided by  $N$  for calculating appropriate, which is necessary for further calculation of Fourier coefficients.

cosine component, and each sine and cosine component requires one digital multiplier and digital accumulator. Therefore, if the system should measure DC component and  $N_h$  harmonics this structure requires  $2N_h+1$  multipliers and  $2N_h+1$  accumulators.

At first sight, block diagram from Fig. 6 seems to require complex hardware structure but its hardware implementation can be relatively simple by using FPGA (it is described in more details in section dedicated to experiments).

### D. Measurement Uncertainty

In [7] output and relative measurement uncertainty were analyzed, and calculations of variance of multiplier output lead to determining variance of the average accumulator output and the relative measurement uncertainty. In digital stochastic measurement block the variance of the multiplier output is also consisted of deterministic variance, random variance and error (stochastic-related) variance. These parts are uncorrelated, hence the total variance of  $\Psi$  is [7]:

$$\sigma_{\Psi}^2 = \sigma_d^2 + \sigma_r^2 + \sigma_e^2 \quad (11)$$

Deterministic variance  $\sigma_d^2$ , according to [7], is defined as:

$$\sigma_d^2 = \frac{1}{T} \int_0^T (s_e s_a)^2 dt - \left( \frac{1}{T} \int_0^T s_e s_a dt \right)^2 \quad (12)$$

However the deterministic variance  $\sigma_d^2$  is the property of the signal and is not to be included to the measurement uncertainty [7]. Random variance and error (stochastic-related) variance,  $\sigma_r^2$  and  $\sigma_e^2$ , satisfy the central limit theorem [11] and variances of their average values depend on the number of samples  $N$  within the measurement subinterval  $T$ :

$$\sigma_r^2 = \frac{\sigma_r^2}{N}, \quad \sigma_e^2 = \frac{\sigma_e^2}{N} \quad (13)$$

Standard measurement uncertainty of average value  $\bar{\Psi}$  is defined by standard deviation:

$$u(\bar{\Psi}) = \sqrt{\sigma_r^2 + \sigma_e^2} \quad (14)$$

The relative measurement uncertainty  $u$  is defined by the standard deviation and the average value of the accumulator output:

$$u = \frac{\sqrt{\sigma_r^2 + \sigma_e^2}}{\bar{\Psi}} \quad (15)$$

Similarly to [7] the standard measurement uncertainty and the relative measurement uncertainty are limited by:

$$u(\bar{\Psi}) \leq \frac{S_a \cdot (\sigma_n + \frac{\Delta_1}{2})}{\sqrt{N}}, \quad u \leq \frac{S_a \cdot (\sigma_n + \frac{\Delta_1}{2})}{\bar{\Psi} \cdot \sqrt{N}} \quad (16)$$

Limit of the standard measurement uncertainty (16) is determined by the root mean square (RMS) value of the auxiliary signal ( $S_a$ ), noise ( $\sigma_n$ ), the resolution in A/D converter ( $\Delta_1$ ), and by the number of samples within the measurement subinterval ( $N$ ). If  $R$  is the amplitude of the auxiliary signal, then:

$$S_a = R / \sqrt{2} \quad (17)$$

According to (10), (16) and (17) standard measurement uncertainty of any Fourier coefficient measured by this method is limited by:

$$u(a_k) = u(b_k) \leq \frac{\sqrt{2} \cdot (\sigma_n + \frac{\Delta_1}{2})}{\sqrt{N}} \quad (18)$$

$$u(\sqrt{a_k^2 + b_k^2}) \leq \frac{2 \cdot (\sigma_n + \frac{\Delta_1}{2})}{\sqrt{N}} \quad (19)$$

The quantum  $\Delta_1$  is defined by the A/D converter resolution, and the number of samples  $N$  can be a compromise between the necessary measurement speed and the required accuracy [7]. Therefore the system can have a very good accuracy even when the measurement noise is significant, due to the increased number of samples  $N$ .

If the A/D converter would be an ideal one, then  $\Delta_1=0$  and right side of (18) is transformed into  $\sqrt{2} \cdot \sigma_n / \sqrt{N}$ , which is square root of Cramér–Rao lower bound (CRLB) [12].

### III. MEASUREMENT EXAMPLE

As an example of non-stationary signal for testing the developed method, noisy brain potential is selected. These potentials are recordings of the small electrical potentials (generally less than 300  $\mu\text{V}$ ) produced by the brain [13-14]. They can be divided into two categories: spontaneous brain potentials, commonly named as EEG (electroencephalography) signals, and non-spontaneous brain potentials ERP (Event Related Potential) signals. The frequencies of spontaneous brain produced potentials range from 0.5 to 100 Hz, and their characteristics are highly dependent on the degree of activity of the cerebral cortex [15]. From a hardware standpoint brain potentials are the most difficult electrogram measurement to acquire [14].

The typical measurement system uses Ag/AgCl electrodes contained within a net or hat placed on the scalp of the patient; net or hat then connects to the hardware block using a cable several feet in length, subjecting the microvolt level brain potential to ambient noise that is many times greater than the signal itself. To amplify such low level voltage, this hardware block incorporates amplifying circuits but also Driven Right Leg (DRL) technique [16] and high-order analog filters with high gain (5000-20000 times) and sharp roll-off, to ensure that the only the desired signal is detected [17-18]. There are also some other techniques used for rejecting the noise, but they will be not be described here because it is out of the scope of this paper.

If implemented correctly, this conditioning of brain potential is generally satisfying. However, if the measurement system is exposed to high-level ambient noise (e.g. when brain potential measurements are combined with magnetic resonance imaging (MRI) where imaging artifacts appear and signal-to-noise ratio (SNR) can be extremely low), then this conditioning techniques are not satisfying (Fig. 7). In these cases it is necessary to apply some digital data processing for

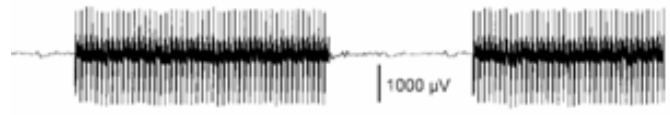


Fig. 7. The illustration from [22], showing the imaging artifact/noise in brain potential records during EEG/fMRI simultaneous recording (graph A). In this case, standard noise rejection techniques are not satisfying.

extracting brain potential [19-22].

### IV. SIMULATION

The aim of the simulation is to faithfully simulate previously described measurement system, in the case of measuring EEG signal. Hence, the simulation was implemented according to model from Fig. 3, and digital stochastic measurement block was implemented according to conceptual block-diagram from Fig. 6.

#### A. Input Signal and Conditioned Signal

Brain potential is chosen as an example of real non-stationary signal. Input signal is extracted from 2 seconds of real measurement session of the potential (Fig. 8). These values are amplified and superimposed with selected reference voltage (level transition and amplifying are usual tasks of conditioning brain potential), so the conditioned signal is actually the input of digital stochastic measurement block.

Real measurement was performed by the measurement system presented at Fig. 8. The amplifier is a three-stage amplifying and filtering circuit, implemented on one PCB (Printed Circuit Board). At the input, there is a electrostatic discharge protection circuit and passive low-pass filter for rejecting high frequencies (>1kHz).

First amplifying stage is a preamplifier based on instrumentation amplifier INA114P for obtaining high input impedance and high CMRR (Common Mode Rejection Ratio). Its amplification gain is 12. From this stage, inverted common mode voltage is driven to the DRL output of the amplifier and further to DRL cable and location of subject. This technique is often used when it is necessary to increase CMRR, and in this amplifier CMRR is 102dB.

Second amplifying stage has a central role for increasing the amplification gain (its gain is 40). Also, before input and

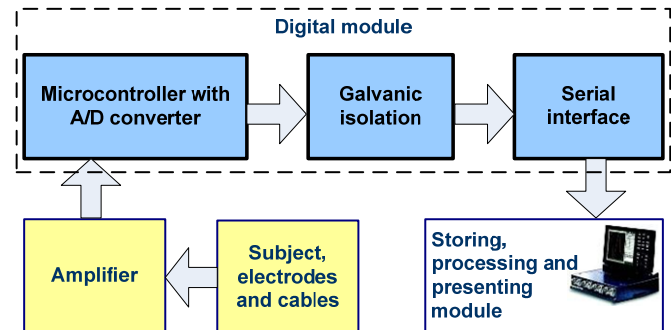


Fig. 8. System applied for real measurements. Amplifier is a three stage conditioning circuit. Digital module is consisted of microcontroller, digital optocouplers providing galvanic isolation and MAX232 providing serial interface to PC.

after output of this stage, there are high-pass filters with corner frequency of 0.15 Hz, thus providing rejection of offset voltage from amplifier input.

Third stage has role of final amplification (amplification is 16) and also of antialiasing filtering. The supply of the amplifier is unipolar (5 V), and there is also virtual ground buffered from 2 V voltage source. This voltage source is implemented on another PCB (the one with microcontroller) and leaded to the amplifier PCB.

Microcontroller module's main role is digitalization of the amplified voltage. This module is based on 8-bit microcontroller PIC18F4550 which has built-in A/D (analog-to-digital) converter with 10-bit resolution. Considering this resolution, the amplifier's amplification gain and A/D conversion reference voltage, the effective input resolution of the system is 0.5  $\mu$ V. Chosen sampling frequency of A/D conversion is 256 Hz. Digital outputs of microcontroller (RC6/TX and RC7/RX) are used for digital communication with PC based on UART (Universal asynchronous receiver/transmitter) protocol. Before connecting these outputs to MAX232 (digital chip for serial communication with PC), there are digital optocouplers implemented for achieving necessary galvanic isolation of the system.

Microcontroller is also connected with the input button, which is intended to be pressed by subject during specific cognitive tasks regarding recognition of stimuli.

In real measurement (which was a typical digital measurement), measurement records were stored 256 samples per second (S/s). For obtaining smooth simulation input and for adjusting simulation with experiment needs (described in the section dedicated to experiments) these 256 S/s records were transformed into 3,840 S/s data. This was achieved by 1) calculating Fourier coefficients by Discrete Fourier Transform (DFT) for original (256 S/s) records and 2) calculating

3,840 S/s data by using IDFT with previously calculated Fourier coefficients. Each sample of conditioned signal is stored as 64-bit floating point value in simulation lookup-table.

### B. Simulation Properties and Results

The DSMB was configured according to data presented in Table I. 4 sets of simulations was run – one without adding noise to the input signal, and other with adding white noise to the input signal. Noise has uniform Probability Density Function (PDF) and signal-to-noise ratio (SNR) was 10dB, 0dB and -10dB (Fig. 10). It is assumed there is no anti-aliasing filter before DSMB, which would limit the noise bandwidth. Therefore, comparing to classical design of conditioning block, it is worse situation (at first sight) regarding level of noise entering the digital block, but it is better situation regarding the size and optimization issues of conditioning block, because the number of conditioning block components are less.

For each SNR value, amplitude of harmonics determined by measured Fourier coefficients was compared versus amplitude determined by DFT of input signal, and absolute values of error was calculated (Table II and Fig. 11). The average error is compared versus theory maximum (19) in order to simplify comparison.

Also, the measured Fourier coefficients were used for calculating time-series (Fig. 12 shows the comparison when no noise is added). Peak-to-peak (pp) value of the resulting time-series is compared against the pp value of the input signal (Table III).

## V. EXPERIMENT

The aim of experiments was to test the theory maximum for measurement uncertainty and to compare experimental results against the simulation results.

TABLE I  
UNITS FOR MAGNETIC PROPERTIES

	<i>Simulations set 0</i>	<i>Simulations set 1</i>	<i>Simulations set 2</i>	<i>Simulations set 3</i>
<i>Number of simulations</i>	250	250	250	250
<i>SNR level</i>	No noise added	10dB	0dB	-10dB
<i>A/D converter (Fig. 6)</i>	Resolution: $m_1=6$ bits Input range: $\pm R$ and $R=2.5V$ Sampling frequency: $f_{adc} = 15625$ Hz			
<i>Measurement subinterval</i>	$[0, T]$ and $T = 20ms$			
<i>Fundamental frequency</i>	$f_0 = 1/T = 50Hz$			
<i>Number of samples per measurement subinterval</i>	$N = 312$			
<i>Digital dithered base functions</i>	Stored in memory in 64-bit floating point resolution but passed to the multiplier in 8-bit resolution, thus faithfully simulating an A/D converter with properties: Resolution: $m_2 = 8$ bits Range: $\pm R$ and $R=2.5V$ Sampling frequency: $f_{adc} = 15625$ Hz			
<i>Number of measured Fourier coefficients</i>	DC component + 15 sine coefficients + 15 cosine coefficients			

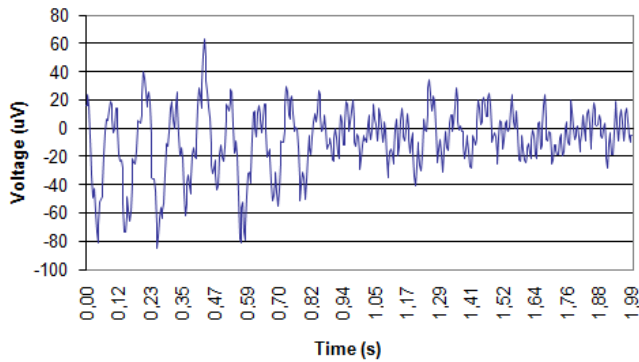


Fig. 9. 2 seconds of recording brain potential. This signal was used for both simulation and experiment input.

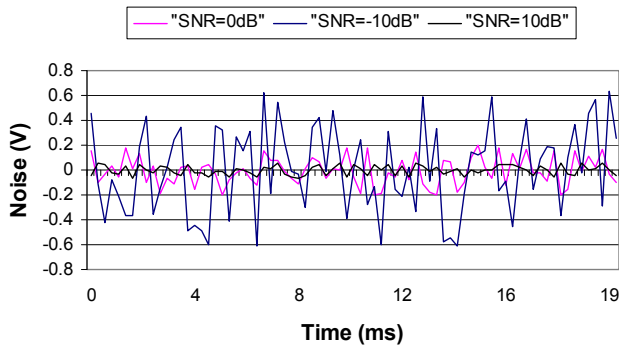


Fig. 10. The examples of the noise added to the input signal of simulations, for various SNR levels. The noise is generated (in both simulation and experiment) at rate of 3840 samples per second.

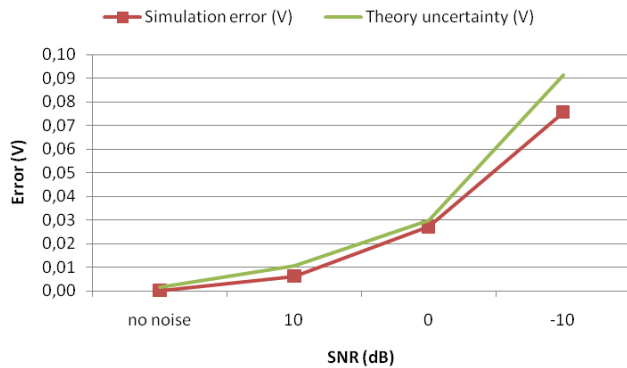


Fig. 11. Average error per harmonic compared against theory maximum for measurement uncertainty.

### A. Input Signal

The plan of experiments required 4 sets of experiments (actually  $4 \cdot 250 = 1000$  experiments) as the simulations were consisted of 4 sets of simulations. For obtaining correct results, comparable with theory and simulation, each experiment had to measure the same signal. Of course, this repeatability of brain potential could not be achieved with humane subject and “live” measurement for each experiment.

Therefore, the source of signal in experimental measurements was not the humane subject, but an artificial source of conditioned signal was made. The same data for conditioned brain potential at the input of DSMB, used in

TABLE II

SIMULATION AVERAGE ERROR PER HARMONIC COMPARED AGAINST THEORY MAXIMUM FOR MEASUREMENT UNCERTAINTY (19)				
SNR (dB)	no noise	10	0	-10
Simulation error (V)	2,08E-04	6,29E-03	2,72E-02	7,57E-02
Theory uncertainty (V)	1,41E-03	1,05E-02	3,00E-02	9,16E-02

TABLE III

RELATIVE ERRORS FOR PEAK-TO-PEAK VALUE AT VARIOUS SNR LEVELS				
SNR (dB)	no noise	10	0	-10
Peak-to-peak relative error (%)	0.26	2.67	46.19	268.69

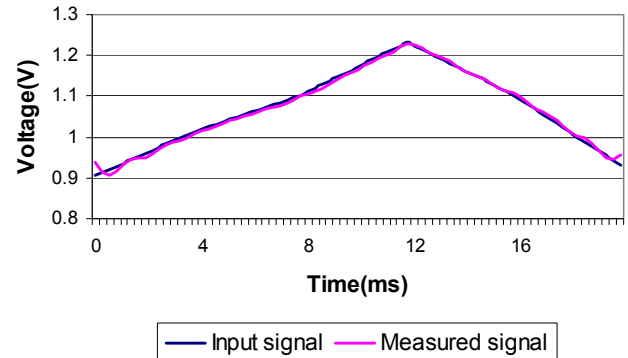


Fig. 12. Comparison of input signal and measured signal in simulations set 0. Measured signal is reconstructed by measured Fourier coefficients. Measurement subinterval is [0, 20ms] and noise is not added to the input signal.

simulations, were also used for the artificial source to generate the signal.

This source was made by development board with a programmable system-on-chip (PSoC) CY8C27843 (Fig. 13), using an embedded 8-bit digital-to-analog (D/A) converter, 16-bit counter and lookup table. Digital values, calculated from brain potential measurement results before experiment, were stored in lookup table (actually 4 sets of digital values depending on SNR level), and sample rate was configured to be 3,840 Hz which provides relatively smooth analog signal at the output. The configured range of D/A converter is from 0 V to 2.6 V.

### B. Implementation of DSMB

At first sight, block diagram from Fig. 6 seems to require complex hardware structure but its hardware implementation can be relatively simple. Block diagram of the hardware implementation is given at Fig. 14, and the photos of hardware at Fig. 15. This hardware implementation was originally developed for measuring line voltage and current harmonics.

The multipliers and accumulators are implemented by FPGA structure (chip Cypress CY39100) which finally calculates Fourier coefficients. The microprocessor (Atmel AT89s8252) interfaces the block with PC, i.e. interfaces FPGA chip with PC. Pseudostochastic dither signal is generated by FPGA chip and analog adder is required for performing addition of dither. The memory is flash EEPROM

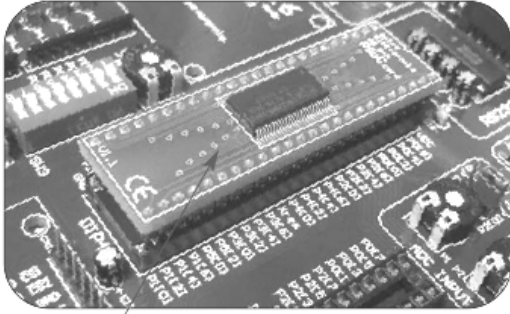


Fig. 13. PSoC CY8C27843 (its mounting on the development board is pointed by arrow) is used as the generator of conditioned signal.

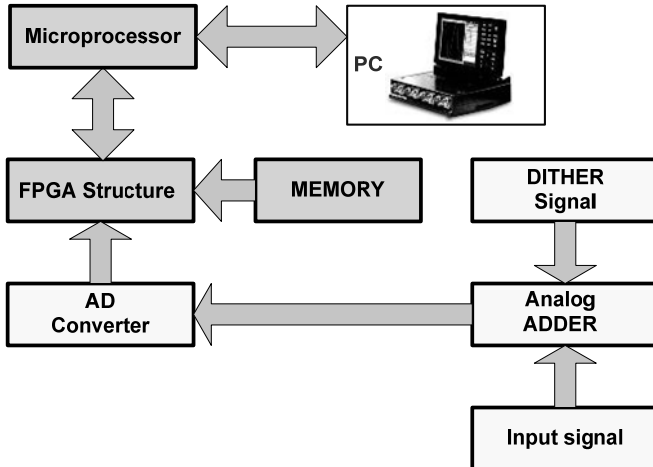


Fig 14. Hardware block diagram of digital stochastic measurement block interfaced to PC.

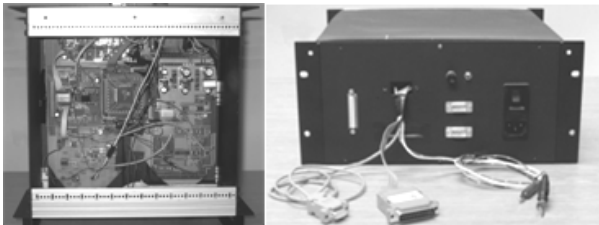


Fig 15. Prototype hardware implementation of block diagram from Fig 13.

memory M29F040 with capacity of 512 Kb.

A/D converter's properties are the same as in simulations (resolution:  $m_1=6$  bits, input range:  $\pm 2.5$  V, sampling rate:  $f_{adc}=15,625$  Hz). Regarding A/D converter, an important thing is that this A/D converter can generally have lower resolution and faster conversion time than the one in typical digital measurement, which can be useful for parallelization of measurements necessary for multichannel recordings.

FPGA chip is programmed with a very-high-speed integrated circuits hardware description language (VHDL) program. The VHDL program is consisted of 4 processes (P1, P2, P3 and P4) which execute simultaneously. Process P1 receives 6-bit digital values from A/D converter. Process P2 is the main process, and all the mathematical calculations are implemented by this process. Process P3 has the task to send the results of process P2 to the microprocessor. Process P4 waits for request from the microprocessor, and when the request comes in P4 activates the process P3.

TABLE IV  
AVERAGE ERROR PER HARMONIC COMPARED VERSUS THEORY MAXIMUM FOR MEASUREMENT UNCERTAINTY (19)

SNR (dB)	no noise	10	0	-10
Experiment error (V)	2,51E-04	7,73E-03	2,77E-02	7,95E-02
Simulation error (V)	2,08E-04	6,29E-03	2,72E-02	7,57E-02
Theory uncertainty (V)	1,41E-03	1,05E-02	3,00E-02	9,16E-02

PC software application receives the data from microprocessor, records and presents the measurement results.

### C. Results

4 sets of experiments were done in the same way as simulations – one without adding noise to the input signal, and other with adding white noise (Fig. 10) to the input signal. Noise has uniform PDF and signal-to-noise ratio (SNR) was 10 dB, 0 dB and -10 dB.

For each SNR value, amplitude of harmonics determined by measured Fourier coefficients was compared versus amplitude determined by DFT of input signal data, and absolute values of error was calculated (Table IV and Fig. 16).

Experiment results showed well adjustment with the limits calculated by formula (19) for three SNR values (10 dB, 0 dB and -10 dB). Resolution of the D/A converter used for generating input signal, and the ambient noise interfered with the interface between input signal generator and DSMB are recognized as factors responsible for the fact that experimental errors are higher than simulation errors.

## VI. DISCUSSION

Hardware resources used in implementation of the digital stochastic measurement block (Fig. 14 and Fig. 15) are pretty modest comparing to the technology state of the art. In future research, it would be interesting to investigate, what would be the results of measurement if the sampling frequency of the A/D converter is drastically increased (e.g. 1 MHz) and if the number of measured harmonics is increased, because actual A/D and FPGA chips allow such implementation and theoretically developed formula for measurement uncertainty limit indicates the possibility of significant improvement of the measuring system accuracy and noise rejection.

It would also be interesting to extend measurement subinterval (e.g. to 2, 4 or 8 seconds, because FFT of brain potential is usually calculated for a short section of time series - from 1 to 8 seconds [13]). This extension would increase the number of samples involved in measurement subinterval (i.e. increase the accuracy), but it would also increase delay time for presenting reconstructed time-series. This delay time would be disadvantage if the application of measurement would include necessity for real-time control/reaction, but otherwise this would not be problematic (like in measurements of ERP brain potential, when processing of measurement data is performed after the appropriate measurement interval [23]).

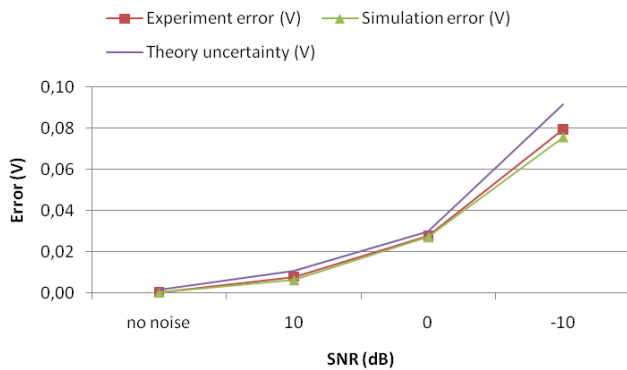


Fig 16. Average error per harmonic by experiment compared against simulation results and theory maximum for measurement uncertainty.

## VII. CONCLUSION

Accurate measurement of weak and noisy signals presents a challenge in digital measurements. The previous research on digital stochastic measurement shown to be relatively robust to noise as it gives accurate results even when the noise is greater than the measured stationary signal.

The research described in this paper evaluated digital stochastic measurement method implementation for non-stationary signals and compared it to the method implementation for stationary signals. Developed theory resulted in formula for theory limit of measurement uncertainty, and this theory is tested with applied simulations and experiments.

Brain potential is chosen as an example of real non-stationary signal which is to be measured. The noise is added in three sets of simulations and experiments for inspecting the noise rejection of the method.

The experimental test signal generator and prototype instrument has been used in experiments. The implemented digital stochastic measurement block includes a flash A/D converter, a memory for dithered base functions, and one signal multiplier and a digital accumulator for each sine and cosine components of the measured harmonics realized by FPGA structure.

The simulations and experiments have shown well agreement with the developed formula for measurement uncertainty limit. This formula shows the possibility of controlling measurement uncertainty even if it is necessary to work with the constant measurement subinterval. This limit is dependent on number of samples over the measurement interval, which is determined by sampling rate of A/D converter inside digital stochastic measurement block, allowing designer to choose A/D converter with lower resolutions and faster sampling rate for achieving more accurate measurement and measurement more robust to noise.

## REFERENCES

- [1] M.B. Priestley, *Non-linear and Non-stationary Time Series Analysis*, Academic Press, 1988.
- [2] W. J. Fitzgerald, R. L. Smith, A. T. Walde, P. C. Young, *Nonlinear and Nonstationary Signal Processing*, Cambridge University Press; 1st ed, 2001.
- [3] J. von Neumann, "Probabilistic logic and the synthesis of reliable organisms from unreliable components," in *Automata studies*, CE Shannon, Ed. Princeton, NJ: Princeton University Press, 1956.
- [4] M.F.Wagdy, W.Ng, "Validity of uniform quantization error model for sinusoidal signals without and with dither," *IEEE Trans. Instrum. Meas.*, vol. 38, pp. 718-722, June 1989.
- [5] V. Vujičić, S. Milovančev, M. Pešaljević, D. Pejić and I. Župunski, "Low frequency stochastic true RMS instrument," *IEEE Trans. Instrum. Meas.*, vol. 48, pp.467-470, Apr. 1999.
- [6] D. Pejić, V. Vujicic, "Accuracy limit of high-precision stochastic Watt-hour meter," *IEEE Trans. Instrum. Meas.*, vol. 49, pp. 617-620, June 2000.
- [7] B. Santrač, M. A. Sokola, Z. Mitrović, Ivan Župunski and V. Vujičić, "A Novel Method for Stochastic Measurement of Harmonics at Low Signal-to-Noise Ratio", *IEEE Trans. Instrum. Meas.*, vol. 58, pp. 3434-3441, Oct. 2009.
- [8] V. Pjevalica, and V. Vujičić, "Further Generalization of the Low-Frequency True-RMS instrument (Periodical style—Accepted for publication)", *IEEE Trans. Instrum. Meas.*, to be published.
- [9] Sovilj P. M., Milovančev S. S., Vujičić V.: Digital Stochastic Measurement of a Nonstationary Signal With an Example of EEG Signal Measurement, *Instrumentation and Measurement IEEE Transactions on*, Vol. 60 - issue 9, pp. 3230-3232, 2011.
- [10] V. Vujičić, "Generalized low frequency stochastic true RMS instrument", *IEEE Trans. Instrum. Meas.*, vol. 50, pp. 1089-1092, Oct. 2001.
- [11] A. Papoulis, "Probability, random variables and stochastic processes", McGraw-Hill series in Systems Science, USA, 1965.
- [12] S.M. Kay, "Fundamentals of Statistical Signal Processing, Volume I: Estimation Theory", Vol. I, 1st ed., pp. 27-82, New Jersey: Prentice Hall PTR, 1993.
- [13] J.D. Bronzino, "Principles of Electroencephalography", in *Biomedical Engineering Handbook*, Vol. I, J.D. Bronzino, 2nd ed., New York: CRC Press LLC, 2000.
- [14] J. G. Webster, "Medical Instrumentation Application and Design", New York: Wiley, 1998.
- [15] M. Abeles and M. Goldstein, "Multispikes Train Analysis", *Proc. IEEE*, No. 65, pp (762-773), 1977.
- [16] B. B. Winter and J. G. Webster, "Driven-right-leg circuit design", *IEEE Trans. Biomed. Eng.*, vol. 30, pp. 62-66, 1983.
- [17] M. Kutz, "Standard Handbook of Biomedical Engineering and Design", McGraw-Hill, 2003.
- [18] B. A. Schmitz, "Improving signal quality and test reliability in EEG measurements using integrated high-density surface-mount electronics", *SMAT Medical Electronics Symposium*, Minneapolis Airport Marriott, Bloomington, May 2004
- [19] L. M. Angeloneb, P. L. Purdona, J. Ahveninena, J. W. Belliveaua and G. Bonmassara, "EEG/(f)MRI measurements at 7 Tesla using a new EEG cap ("InkCap")", *NeuroImage*, vol. 33, pp. 1082-1092, 2006
- [20] M. Negishi, B.I. Pinus, A.B. Pinus and R.T. Constable, "Origin of the Radio Frequency Pulse Artifact in Simultaneous EEG-fMRI Recording: Rectification at the Carbon-Metal Interface", *IEEE Trans. Biomed. Eng.*, Sept. 2007, vol. 54, pp. 1725 - 1727
- [21] S. M. Mirsattari, J. R. Ives, S. Leung and R. S. Menon, "EEG Monitoring during Functional MRI in Animal Models", *Epilepsia*, vol. 48(suppl. 4), pp. 37-46, Blackwell Publishing, Inc., 2007
- [22] Philip J. Allen, Oliver Josephs, and Robert Turner, "A Method for Removing Imaging Artifact from Continuous EEG Recorded during Functional MRI", *NeuroImage*, vol. 12, pp. 230-239, 2000
- [23] E. Donchin, K. M. Spencer, and R. Wijesinghe, "The mental prosthesis: Assessing the speed of a P300-based brain-computer interface," *IEEE Trans. Rehab. Eng.*, vol. 8, pp. 174-179, June 2000.



# Instructions for Authors

First A. Author, Second B. Author, and Third C. Author

**Abstract**—These instructions give you guidelines for preparing papers for ELECTRONICS journal. Use this document as a template if you are using Microsoft *Word* 6.0 or later. Otherwise, use this document as an instruction set. The electronic file of your paper will be formatted further. Define all symbols used in the abstract. Do not cite references in the abstract. Do not delete the blank line immediately above the abstract; it sets the footnote at the bottom of this column.

**Index Terms**—About four key words or phrases in alphabetical order, separated by commas.

## I. INTRODUCTION

THIS document is a template for Microsoft *Word* versions 6.0 or later.

When you open the file, select “Page Layout” from the “View” menu in the menu bar (View | Page Layout), which allows you to see the footnotes. Then, type over sections of file or cut and paste from another document and use markup styles. The pull-down style menu is at the left of the Formatting Toolbar at the top of your *Word* window (for example, the style at this point in the document is “Text”). Highlight a section that you want to designate with a certain style, then select the appropriate name on the style menu. The style will adjust your fonts and line spacing. **Do not change the font sizes or line spacing to squeeze more text into a limited number of pages.** Use italics for emphasis; do not underline. The length of the manuscript is limited to the maximum of 15 pages.

To insert images in *Word*, position the cursor at the insertion point and either use Insert | Picture | From File or

copy the image to the Windows clipboard and then Edit | Paste Special | Picture (with “float over text” unchecked).

We will do the final formatting of your paper.

## II. PROCEDURE FOR PAPER SUBMISSION

### A. Review Stage

The manuscripts are to be delivered to the editor by e-mail: electronics@etfbl.net. Prepare it in two-column format as shown in this template. Place all figures and tables at the end of the paper (after the references) on separate page(s). Figures and tables must have the same caption names as referenced in the text. Only PDF format of the manuscript is allowed at the review stage. Please, check if all fonts are embedded and subset and that the quality of diagrams, illustrations, and graphics is satisfactory. Failing to provide above listed requirements is a valid reason for rejection.

### B. Final Stage

When you submit your final version (after your paper has been accepted), prepare it in two-column format, including figures and tables in accordance with this template. Pack all of your files (manuscript source file in *Word*, figures, and manuscript PDF form) within one archive file (you may use any of the available file compression tools: *WinZip*, *WinRAR*, *7-Zip*, etc.). Do not forget to provide the manuscript converted in PDF format that will be used as a reference for final formatting of your paper. Figures should be named as referenced in the manuscript (e.g. *fig1.eps*, *fig2.tif*, etc.)

### C. Figures and Tables

Format and save your graphic images using a suitable graphics processing program and adjusts the resolution settings. We accept images in the following formats: PS, EPS, TIFF, GIF, and PNG. Additionally, it is allowed to use images generated by using one of the following software tools: Microsoft Word, Microsoft PowerPoint, or Microsoft Excel. The resolution of a RGB color file should be 400 dpi. Please note that JPG and other lossy-compressed image formats are not allowed. Use available software tools to convert these images to appropriate format.

Image quality is very important to how yours graphics will reproduce. Even though we can accept graphics in many formats, we cannot improve your graphics if they are poor quality when we receive them. If your graphic looks low in quality on your printer or monitor, please keep in mind that cannot improve the quality after submission.

Manuscript received 15 September 2011 (write the date when you have first sent the manuscript for review). Received in revised form 20 October 2011 (write the date when you have sent the manuscript in its revised form if revisions required for your paper after review).

(Place here any sponsor and financial support acknowledgments).

F. A. Author is with the Faculty of Electrical Engineering, University of Banja Luka, Banja Luka, Bosnia and Herzegovina (corresponding author to provide phone: +387-51-222-333; fax: +387-51-111-222; e-mail: author@etfbl.net).

S. B. Author was with Faculty of Technical Sciences, University of Novi Sad, Novi Sad, Serbia. He is now with the Institute “Mihailo Pupin”, Belgrade, Serbia (e-mail: author@pupin.rs).

T. C. Author is with the School of Electrical Engineering, University of Belgrade, Belgrade, Serbia, on leave from the Faculty of Electronic Engineering, University of Niš, Niš, Serbia (e-mail: author@elfak.ni.ac.rs).

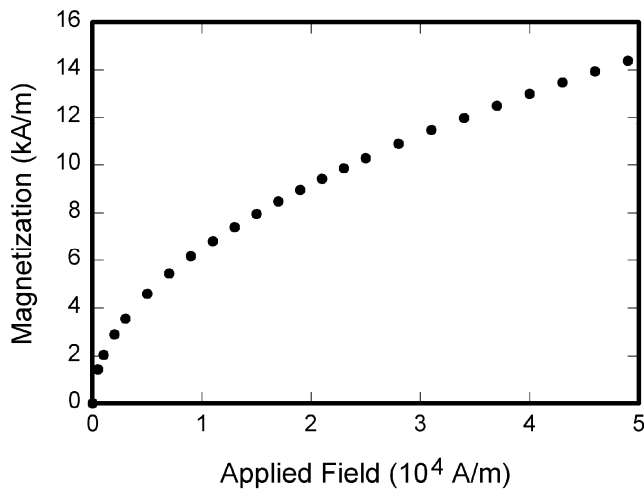


Fig. 1. Magnetization as a function of applied field. Note that “Fig.” is abbreviated. There is a period after the figure number, followed by two spaces. It is good practice to explain the significance of the figure in the caption.

If you are importing your graphics into this Word template, please use the following steps:

Under the option EDIT select PASTE SPECIAL. A dialog box will open, select paste picture, then click OK. Your figure should now be in the Word Document.

If you are preparing images in TIFF, EPS, or PS format, note the following. High-contrast line figures and tables should be prepared with 600 dpi resolution and saved with no compression, 1 bit per pixel (monochrome).

Photographs and grayscale figures should be prepared with 300 dpi resolution and saved with no compression, 8 bits per pixel (grayscale).

Most charts graphs and tables are one column wide (3 1/2 inches or 21 picas) or two-column width (7 1/16 inches, 43 picas wide). We recommend that you avoid sizing figures less than one column wide, as extreme enlargements may distort your images and result in poor reproduction. Therefore, it is better if the image is slightly larger, as a minor reduction in size should not have an adverse affect the quality of the image.

### III. MATH

If you are using *Word*, use either the Microsoft Equation Editor or the *MathType* add-on (<http://www.mathtype.com>) for equations in your paper (Insert | Object | Create New | Microsoft Equation *or* MathType Equation). “Float over text” should *not* be selected.

### IV. UNITS

Use either SI (MKS) or CGS as primary units. (SI units are strongly encouraged.) English units may be used as secondary units (in parentheses). **This applies to papers in data storage.** For example, write “15 Gb/cm<sup>2</sup> (100 Gb/in<sup>2</sup>).” An exception is when English units are used as identifiers in trade, such as “3½-in disk drive.” Avoid combining SI and CGS units, such as current in amperes and magnetic field in

TABLE I  
UNITS FOR MAGNETIC PROPERTIES

Symbol	Quantity	Conversion from Gaussian and CGS EMU to SI <sup>a</sup>
$\Phi$	magnetic flux	1 Mx $\rightarrow$ $10^{-8}$ Wb = $10^{-8}$ V·s
$B$	magnetic flux density, magnetic induction	1 G $\rightarrow$ $10^{-4}$ T = $10^{-4}$ Wb/m <sup>2</sup>
$H$	magnetic field strength	1 Oe $\rightarrow$ $10^3/(4\pi)$ A/m
$m$	magnetic moment	1 erg/G = 1 emu $\rightarrow$ $10^{-3}$ A·m <sup>2</sup> = $10^{-3}$ J/T
$M$	magnetization	1 erg/(G·cm <sup>3</sup> ) = 1 emu/cm <sup>3</sup> $\rightarrow$ $10^3$ A/m
$4\pi M$	magnetization	1 G $\rightarrow$ $10^3/(4\pi)$ A/m
$\sigma$	specific magnetization	1 erg/(G·g) = 1 emu/g $\rightarrow$ 1 A·m <sup>2</sup> /kg
$j$	magnetic dipole moment	1 erg/G = 1 emu $\rightarrow$ $4\pi \times 10^{-10}$ Wb·m
$J$	magnetic polarization	1 erg/(G·cm <sup>3</sup> ) = 1 emu/cm <sup>3</sup> $\rightarrow$ $4\pi \times 10^{-4}$ T
$\chi, \kappa$	susceptibility	1 $\rightarrow$ $4\pi$
$\chi_p$	mass susceptibility	1 cm <sup>3</sup> /g $\rightarrow$ $4\pi \times 10^{-3}$ m <sup>3</sup> /kg
$\mu$	permeability	1 $\rightarrow$ $4\pi \times 10^{-7}$ H/m = $4\pi \times 10^{-7}$ Wb/(A·m)
$\mu_r$	relative permeability	$\mu \rightarrow \mu_r$
$w, W$	energy density	1 erg/cm <sup>3</sup> $\rightarrow$ $10^{-1}$ J/m <sup>3</sup>
$N, D$	demagnetizing factor	1 $\rightarrow$ $1/(4\pi)$

Vertical lines are optional in tables. Statements that serve as captions for the entire table do not need footnote letters.

<sup>a</sup>Gaussian units are the same as cgs emu for magnetostatics; Mx = maxwell, G = gauss, Oe = oersted; Wb = weber, V = volt, s = second, T = tesla, m = meter, A = ampere, J = joule, kg = kilogram, H = henry.

oersteds. This often leads to confusion because equations do not balance dimensionally. If you must use mixed units, clearly state the units for each quantity in an equation.

The SI unit for magnetic field strength  $H$  is A/m. However, if you wish to use units of T, either refer to magnetic flux density  $B$  or magnetic field strength symbolized as  $\mu_0 H$ . Use the center dot to separate compound units, e.g., “A·m<sup>2</sup>.”

## V. HELPFUL HINTS

### A. Figures and Tables

Because we will do the final formatting of your paper, you do not need to position figures and tables at the top and bottom of each column. In fact, all figures, figure captions, and tables can be at the end of the paper. Large figures and tables may span both columns. Place figure captions below the figures; place table titles above the tables. If your figure has two parts, include the labels “(a)” and “(b)” as part of the artwork. Please verify that the figures and tables you mention in the text actually exist. **Please do not include captions as part of the figures. Do not put captions in “text boxes” linked to the figures. Do not put borders around the outside of your figures.** Use the abbreviation “Fig.” even at the beginning of a sentence. Do not abbreviate “Table.” Tables are numbered with Roman numerals.

Color printing of figures is not available Do not use color unless it is necessary for the proper interpretation of your figures.

Figure axis labels are often a source of confusion. Use words rather than symbols. As an example, write the quantity

“Magnetization,” or “Magnetization  $M$ ,” not just “ $M$ .” Put units in parentheses. Do not label axes only with units. As in Fig. 1, for example, write “Magnetization (A/m)” or “Magnetization ( $A \cdot m^{-1}$ ),” not just “A/m.” Do not label axes with a ratio of quantities and units. For example, write “Temperature (K),” not “Temperature/K.”

Multipliers can be especially confusing. Write “Magnetization (kA/m)” or “Magnetization ( $10^3$  A/m).” Do not write “Magnetization (A/m)  $\times$  1000” because the reader would not know whether the top axis label in Fig. 1 meant 16000 A/m or 0.016 A/m. Figure labels should be legible, approximately 8 to 12 point type.

### B. References

Number citations consecutively in square brackets [1]. The sentence punctuation follows the brackets [2]. Multiple references [2], [3] are each numbered with separate brackets [1]–[3]. When citing a section in a book, please give the relevant page numbers [2]. In sentences, refer simply to the reference number, as in [3]. Do not use “Ref. [3]” or “reference [3]” except at the beginning of a sentence: “Reference [3] shows ... .” Please do not use automatic endnotes in *Word*, rather, type the reference list at the end of the paper using the “References” style.

Number footnotes separately in superscripts (Insert | Footnote).<sup>1</sup> Place the actual footnote at the bottom of the column in which it is cited; do not put footnotes in the reference list (endnotes). Use letters for table footnotes (see Table I).

Please note that the references at the end of this document are in the preferred referencing style. Give all authors’ names; do not use “*et al.*” unless there are six authors or more. Use a space after authors’ initials. Papers that have not been published should be cited as “unpublished” [4]. Papers that have been accepted for publication, but not yet specified for an issue should be cited as “to be published” [5]. Papers that have been submitted for publication should be cited as “submitted for publication” [6]. Please give affiliations and addresses for private communications [7].

Capitalize only the first word in a paper title, except for proper nouns and element symbols. For papers published in translation journals, please give the English citation first, followed by the original foreign-language citation [8]. All references **must be** written in Roman alphabet.

### C. Abbreviations and Acronyms

Define abbreviations and acronyms the first time they are used in the text, even after they have already been defined in the abstract. Abbreviations such as IEEE, SI, ac, and dc do not have to be defined. Abbreviations that incorporate periods should not have spaces: write “C.N.R.S.,” not “C. N. R. S.” Do not use abbreviations in the title unless they are unavoidable (for example, “IEEE” in the title of this article).

<sup>1</sup>It is recommended that footnotes be avoided (except for the unnumbered footnote with the receipt date and authors’ affiliations on the first page). Instead, try to integrate the footnote information into the text.

### D. Equations

Number equations consecutively with equation numbers in parentheses flush with the right margin, as in (1). First use the equation editor to create the equation. Then select the “Equation” markup style. Press the tab key and write the equation number in parentheses. To make your equations more compact, you may use the solidus (/), the exp function, or appropriate exponents. Use parentheses to avoid ambiguities in denominators. Punctuate equations when they are part of a sentence, as in

$$\int_0^{r_2} F(r, \varphi) dr d\varphi = [\sigma r_2 / (2\mu_0)] \cdot \int_0^\infty \exp(-\lambda |z_j - z_i|) \lambda^{-1} J_1(\lambda r_2) J_0(\lambda r_i) d\lambda. \quad (1)$$

Be sure that the symbols in your equation have been defined before the equation appears or immediately following. Italicize symbols ( $T$  might refer to temperature, but  $T$  is the unit tesla). Refer to “(1),” not “Eq. (1)” or “equation (1),” except at the beginning of a sentence: “Equation (1) is ... .”

### E. Other Recommendations

Use one space after periods and colons. Hyphenate complex modifiers: “zero-field-cooled magnetization.” Avoid dangling participles, such as, “Using (1), the potential was calculated.” [It is not clear who or what used (1).] Write instead, “The potential was calculated by using (1),” or “Using (1), we calculated the potential.”

Use a zero before decimal points: “0.25,” not “.25.” Use “ $cm^3$ ,” not “cc.” Indicate sample dimensions as “0.1 cm  $\times$  0.2 cm,” not “0.1  $\times$  0.2  $cm^2$ .” The abbreviation for “seconds” is “s,” not “sec.” Do not mix complete spellings and abbreviations of units: use “Wb/m<sup>2</sup>” or “webers per square meter,” not “webers/m<sup>2</sup>.” When expressing a range of values, write “7 to 9” or “7-9,” not “7~9.”

A parenthetical statement at the end of a sentence is punctuated outside of the closing parenthesis (like this). (A parenthetical sentence is punctuated within the parentheses.) In American English, periods and commas are within quotation marks, like “this period.” Other punctuation is “outside”! Avoid contractions; for example, write “do not” instead of “don’t.” The serial comma is preferred: “A, B, and C” instead of “A, B and C.”

If you wish, you may write in the first person singular or plural and use the active voice (“I observed that ...” or “We observed that ...” instead of “It was observed that ...”). Remember to check spelling. If your native language is not English, please get a native English-speaking colleague to carefully proofread your paper.

## VI. SOME COMMON MISTAKES

The word “data” is plural, not singular. The subscript for the permeability of vacuum  $\mu_0$  is zero, not a lowercase letter “o.” The term for residual magnetization is “remanence”; the adjective is “remanent”; do not write “remnance” or “remnant.” Use the word “micrometer” instead of “micron.” A

graph within a graph is an “inset,” not an “insert.” The word “alternatively” is preferred to the word “alternately” (unless you really mean something that alternates). Use the word “whereas” instead of “while” (unless you are referring to simultaneous events). Do not use the word “essentially” to mean “approximately” or “effectively.” Do not use the word “issue” as a euphemism for “problem.” When compositions are not specified, separate chemical symbols by en-dashes; for example, “NiMn” indicates the intermetallic compound  $\text{Ni}_{0.5}\text{Mn}_{0.5}$  whereas “Ni–Mn” indicates an alloy of some composition  $\text{Ni}_x\text{Mn}_{1-x}$ .

Be aware of the different meanings of the homophones “affect” (usually a verb) and “effect” (usually a noun), “complement” and “compliment,” “discreet” and “discrete,” “principal” (e.g., “principal investigator”) and “principle” (e.g., “principle of measurement”). Do not confuse “imply” and “infer.”

Prefixes such as “non,” “sub,” “micro,” “multi,” and “ultra” are not independent words; they should be joined to the words they modify, usually without a hyphen. There is no period after the “et” in the Latin abbreviation “*et al.*” (it is also italicized). The abbreviation “i.e.,” means “that is,” and the abbreviation “e.g.,” means “for example” (these abbreviations are not italicized).

An excellent style manual and source of information for science writers is [9].

## VII. EDITORIAL POLICY

Each manuscript submitted is subjected to the following review procedure:

- It is reviewed by the editor for general suitability for this publication
- If it is judged suitable, two reviewers are selected and a single-blinded review process takes place
- Based on the recommendations of the reviewers, the editor then decides whether the particular paper should be accepted as is, revised or rejected.

Do not submit a paper you have submitted or published elsewhere. Do not publish “preliminary” data or results. The submitting author is responsible for obtaining agreement of all coauthors and any consent required from sponsors before submitting a paper. It is the obligation of the authors to cite relevant prior work.

Every paper submitted to “Electronics” journal are single-blind reviewed. For conference-related papers, the decision to accept or reject a paper is made by the conference editors and publications committee; the recommendations of the referees are advisory only. Undecipherable English is a valid reason for rejection.

## VIII. PUBLICATION PRINCIPLES

The contents of “Electronics” are peer-reviewed and archival. The “Electronics” publishes scholarly articles of archival value as well as tutorial expositions and critical reviews of classical subjects and topics of current interest.

Authors should consider the following points:

- 1) Technical papers submitted for publication must advance the state of knowledge and must cite relevant prior work.
- 2) The length of a submitted paper should be commensurate with the importance, or appropriate to the complexity, of the work. For example, an obvious extension of previously published work might not be appropriate for publication or might be adequately treated in just a few pages.
- 3) Authors must convince both peer reviewers and the editors of the scientific and technical merit of a paper; the standards of proof are higher when extraordinary or unexpected results are reported.
- 4) Because replication is required for scientific progress, papers submitted for publication must provide sufficient information to allow readers to perform similar experiments or calculations and use the reported results. Although not everything need be disclosed, a paper must contain new, useable, and fully described information. For example, a specimen’s chemical composition need not be reported if the main purpose of a paper is to introduce a new measurement technique. Authors should expect to be challenged by reviewers if the results are not supported by adequate data and critical details.
- 5) Papers that describe ongoing work or announce the latest technical achievement, which are suitable for presentation at a professional conference, may not be appropriate for publication in “Electronics”.

## IX. CONCLUSION

A conclusion section is not required. Although a conclusion may review the main points of the paper, do not replicate the abstract as the conclusion. A conclusion might elaborate on the importance of the work or suggest applications and extensions.

## APPENDIX

Appendixes, if needed, appear before the acknowledgment.

## ACKNOWLEDGMENT

The preferred spelling of the word “acknowledgment” in American English is without an “e” after the “g.” Use the singular heading even if you have many acknowledgments. Avoid expressions such as “One of us (S.B.A.) would like to thank ... .” Instead, write “F. A. Author thanks ... .” **Sponsor and financial support acknowledgments are placed in the unnumbered footnote on the first page, not here.**

## REFERENCES

- [1] G. O. Young, “Synthetic structure of industrial plastics (Book style with paper title and editor),” in *Plastics*, 2nd ed. vol. 3, J. Peters, Ed. New York: McGraw-Hill, 1964, pp. 15–64.
- [2] W.-K. Chen, *Linear Networks and Systems* (Book style). Belmont, CA: Wadsworth, 1993, pp. 123–135.
- [3] H. Poor, *An Introduction to Signal Detection and Estimation*. New York: Springer-Verlag, 1985, ch. 4.

- [4] B. Smith, "An approach to graphs of linear forms (Unpublished work style)," unpublished.
- [5] E. H. Miller, "A note on reflector arrays (Periodical style—Accepted for publication)," *IEEE Trans. Antennas Propagat.*, to be published.
- [6] J. Wang, "Fundamentals of erbium-doped fiber amplifiers arrays (Periodical style—Submitted for publication)," *IEEE J. Quantum Electron.*, submitted for publication.
- [7] C. J. Kaufman, Rocky Mountain Research Lab., Boulder, CO, private communication, May 1995.
- [8] Y. Yorozu, M. Hirano, K. Oka, and Y. Tagawa, "Electron spectroscopy studies on magneto-optical media and plastic substrate interfaces (Translation Journals style)," *IEEE Transl. J. Magn.Jpn.*, vol. 2, Aug. 1987, pp. 740–741 [Dig. 9<sup>th</sup> Annu. Conf. Magnetics Japan, 1982, p. 301].
- [9] M. Young, *The Technical Writers Handbook*. Mill Valley, CA: University Science, 1989.
- [10] J. U. Duncombe, "Infrared navigation—Part I: An assessment of feasibility (Periodical style)," *IEEE Trans. Electron Devices*, vol. ED-11, pp. 34–39, Jan. 1959.
- [11] S. Chen, B. Mulgrew, and P. M. Grant, "A clustering technique for digital communications channel equalization using radial basis function networks," *IEEE Trans. Neural Networks*, vol. 4, pp. 570–578, Jul. 1993.
- [12] R. W. Lucky, "Automatic equalization for digital communication," *Bell Syst. Tech. J.*, vol. 44, no. 4, pp. 547–588, Apr. 1965.
- [13] S. P. Bingulac, "On the compatibility of adaptive controllers (Published Conference Proceedings style)," in *Proc. 4th Annu. Allerton Conf. Circuits and Systems Theory*, New York, 1994, pp. 8–16.
- [14] G. R. Faulhaber, "Design of service systems with priority reservation," in *Conf. Rec. 1995 IEEE Int. Conf. Communications*, pp. 3–8.
- [15] W. D. Doyle, "Magnetization reversal in films with biaxial anisotropy," in *1987 Proc. INTERMAG Conf.*, pp. 2.2-1–2.2-6.
- [16] G. W. Juette and L. E. Zeffanella, "Radio noise currents in short sections on bundle conductors (Presented Conference Paper style)," presented at the IEEE Summer power Meeting, Dallas, TX, Jun. 22–27, 1990, Paper 90 SM 690-0 PWRS.
- [17] J. G. Kreifeldt, "An analysis of surface-detected EMG as an amplitude-modulated noise," presented at the 1989 Int. Conf. Medicine and Biological Engineering, Chicago, IL.
- [18] J. Williams, "Narrow-band analyzer (Thesis or Dissertation style)," Ph.D. dissertation, Dept. Elect. Eng., Harvard Univ., Cambridge, MA, 1993.
- [19] N. Kawasaki, "Parametric study of thermal and chemical nonequilibrium nozzle flow," M.S. thesis, Dept. Electron. Eng., Osaka Univ., Osaka, Japan, 1993.
- [20] J. P. Wilkinson, "Nonlinear resonant circuit devices (Patent style)," U.S. Patent 3 624 12, July 16, 1990.
- [21] *IEEE Criteria for Class IE Electric Systems* (Standards style), IEEE Standard 308, 1969.
- [22] *Letter Symbols for Quantities*, ANSI Standard Y10.5-1968.
- [23] R. E. Haskell and C. T. Case, "Transient signal propagation in lossless isotropic plasmas (Report style)," USAF Cambridge Res. Lab., Cambridge, MA Rep. ARCRL-66-234 (II), 1994, vol. 2.
- [24] E. E. Reber, R. L. Michell, and C. J. Carter, "Oxygen absorption in the Earth's atmosphere," Aerospace Corp., Los Angeles, CA, Tech. Rep. TR-0200 (420-46)-3, Nov. 1988.
- [25] (Handbook style) *Transmission Systems for Communications*, 3rd ed., Western Electric Co., Winston-Salem, NC, 1985, pp. 44–60.
- [26] *Motorola Semiconductor Data Manual*, Motorola Semiconductor Products Inc., Phoenix, AZ, 1989.
- [27] (Basic Book/Monograph Online Sources) J. K. Author. (year, month, day). Title (edition) [Type of medium]. Volume (issue). Available: [http://www.\(URL\)](http://www.(URL))
- [28] J. Jones. (1991, May 10). Networks (2nd ed.) [Online]. Available: <http://www.atm.com>
- [29] (Journal Online Sources style) K. Author. (year, month). Title. *Journal* [Type of medium]. Volume(issue), paging if given. Available: [http://www.\(URL\)](http://www.(URL))
- [30] R. J. Vidmar. (1992, August). On the use of atmospheric plasmas as electromagnetic reflectors. *IEEE Trans. Plasma Sci.* [Online]. 21(3), pp. 876–880. Available: <http://www.halcyon.com/pub/journals/21ps03-vidmar>



# Instruction for Authors

## *Editorial objectives*

In the journal "Electronics", the scientific papers from different fields of electronics and electrical engineering in the broadest sense are published. Main topics are electronics, automatics, telecommunications, computer techniques, power engineering, nuclear and medical electronics, analysis and synthesis of electronic circuits and systems, new technologies and materials in electronics etc. The main emphasis of papers should be on methods and new techniques, or the application of existing techniques in a novel way.

## *The reviewing process*

Each manuscript submitted is subjected to the following review procedures:

- It is reviewed by the editor for general suitability for this publication;
- If it is judged suitable, two reviewers are selected and a double-blind review process takes place;
- Based on the recommendations of the reviewers, the editor then decides whether the particular paper should be accepted as it is, revised or rejected.

## *Submissions Process*

The manuscripts are to be delivered to the editor by e-mail: [electronics@etfbl.net](mailto:electronics@etfbl.net).

Manuscripts have to be prepared in accordance with the instructions given in the template for paper preparation that can be found on the journal's web page ([www.electronics.etfbl.net](http://www.electronics.etfbl.net)).

**Authors should note that proofs are not supplied prior to publication and ensure that the paper submitted is complete and in its final form.**

## *Copyright*

Articles submitted to the journal should be original contributions and should not be under consideration for any other publication at the same time. Authors submitting articles for publication warrant that the work is not an infringement of any existing copyright and will indemnify the publisher against any breach of such warranty. For ease of dissemination and to ensure proper policing of use, papers and contributions become the legal copyright of the publisher unless otherwise agreed.

# ELECTRONICS, VOL. 17, NO. 1, JUNE 2013

---

## PAPERS

MORLET WAVELET UDWT DENOISING AND EMD BASED BEARING FAULT DIAGNOSIS.....	1
A. Santhana Raj and N. Murali	
COMBINED DISCRETE SPACE VOLTAGE VECTOR WITH DIRECT TORQUE CONTROL FOR BEARINGLESS BRUSHLESS DC MOTOR AND CLOSED-LOOP SUSPENDED FORCE CONTROL.....	9
Zhanshi Sheng, Xiaolian Wang, Fei Tan, and Weiran Wang	
A REALIZATION OF TEMPERATURE MONITORING SYSTEM BASED ON REAL-TIME KERNEL MC/OS AND 1-WIRE BUS .....	16
Haibo Pu, Lijia Xu, and Yanmei Qi	
IMPACT OF SECTORIZATION/VEHICULAR TRAFFIC ON MINIMUM CELL SIZE FOR INFORMATION CAPACITY INCREASE IN CELLULAR SYSTEMS.....	21
Kwashie A. Anang, Predrag B. Rapajic, and Ruiheng Wu	
DEVELOPMENT OF THE ALGORITHM FOR ENERGY EFFICIENCY IMPROVEMENT OF BULK MATERIAL TRANSPORT SYSTEM.....	30
Leposava Ristić, Milan Bebić, and Borislav Jeftenić	
AN EFFICIENT METHOD FOR APPROXIMATION OF NON-RATIONAL TRANSFER FUNCTIONS .....	40
Tomislav B. Šekara, Milan R. Rapaić, and Mihailo P. Lazarević	
INFLUENCE OF SIGNAL STATIONARITY ON DIGITAL STOCHASTIC MEASUREMENT IMPLEMENTATION .....	45
Platon Sovilj, Vladimir Vujičić, Nebojša Pjevalica, Dragan Pejić, Marjan Urekar, and Ivan Župunski	
<hr/>	
INSTRUCTIONS FOR AUTHORS.....	55

---

ISSN 1450 -5843

UDK 621.38